

RWTH Aachen
Fakulty of Mathematics, Computer Science and Natural Sciences

Stabilization of the orientation map in a computational model of L4 in V1 of macaque monkey

Author
Silas André Theinen

Master Thesis in Physics
performed at

Institute for Advanced Simulation
(IAS-6) and JARA-Institute Brain
Structure-Function Relationships (INM-10)
Jülich Research Centre, Jülich, Germany

Supervisors:
Prof. Dr. Markus Diesmann
Prof. Dr. Andreas Offenhäusser

Advisor:
Anno Kurth M. Sc.

Contents

1 Abstract	3
2 Introduction	4
3 Neuroscientific background	4
3.1 Cortical areas and layers	4
3.2 Single neurons	4
3.3 Neural networks	5
3.3.1 Previous work	5
4 Underlying model	6
4.1 Medium range isotropic connectivity	6
4.2 Long range patchy connectivity	7
4.3 Orientation map creation	7
4.4 Short range push-pull connectivity	10
4.4.1 Thalamo-cortical connections	11
4.4.2 Push-pull connections	13
4.5 External input	15
5 Research questions	15
6 Methods	17
6.1 Extensions and modifications	17
6.1.1 Correction for V1 inputs	17
6.1.2 Retina Model	17
6.2 Hebbian inspired weight modulation	18
6.3 Elliptical connectivity	20
6.3.1 Super-localized inhibition	22
6.3.2 Network description	24
6.4 Network analysis	24
6.4.1 Retina input	24
6.4.2 Orientation map retrieve and tuning curves	24
6.4.3 Calculation of the g factor and PSP for conductance based neurons	26
6.4.4 Raster plots of spiking activity	26
6.4.5 Firing rate histogram's	27
6.4.6 Coefficient of variation	27
6.4.7 Power spectra	27
6.4.8 Spatial activity	27
6.4.9 Contrast in-variance	27
6.4.10 Signal to noise ratio	27
7 Results	33
7.1 Isotropic connectivity orientation map retrieve	33
7.2 Hebbian inspired weight modulation enables orientation map retrieve	33
7.3 Super-localized inhibition increases number of correct retrieved orientations and tuning steepness	33
7.3.1 Reciprocal motifs do not enhance excitation-inhibition balancing	38
7.4 Elliptical inhibition steepens tuning curves and rises correct predicted orientations in L4AB	38
7.5 Push-pull connectivity increases tuning prominence	40
7.6 Patchy connectivity further increases correctly predicted orientations and tuning prominence in L4ABE	41
7.7 Intermediate parameters	41
7.8 Additional network measures	44
7.8.1 Super-localized inhibition performs best when being circular	44
7.8.2 Patchy connectivity allows for dashed line retrieve	44
7.8.3 The network's response is contrast in-variant	46

7.8.4	Spatial and temporal grating frequency shift	46
7.8.5	Cortical waves	47
7.8.6	A noise resistant network	50
7.9	Conductance based neurons balance the network at g equal to one	54
7.10	Coefficient of variation	54
8	Conclusion	58
8.1	Summary	58
8.2	Discussion	58
8.2.1	Choice of inputs	58
8.2.2	Isotropic network	58
8.2.3	Weight modulation	58
8.2.4	Inhibitory effect	59
8.2.5	Function and implementation of the push-pull connectivity	59
8.2.6	Function and implementation of the patchy connectivity	60
8.3	Predictive coding	60
8.3.1	Frequency shift	61
8.3.2	Balancing the network at low g factors	61
8.3.3	Network capabilities	61
8.3.4	Network statistics	62
8.3.5	Cortical waves	62
9	Outlook	63
9.1	Neuron model	63
9.2	Connectivity, weight and plasticity	63
9.3	Expanding the model	64

1 Abstract

The visual cortex is one of the best studied areas of the brain. Even though an abundance of data on neurons and their connections have been collected, the functional side of this data is still not fully understood. There are neuron assemblies in early visual areas especially showing a strong reaction, when moving bars of a certain orientation are presented to the eye. Assigning each neuron its bar angle of preferred response results in an orientation map. This thesis is concerned with how the intra-areal connectivity can support the orientation tuning when shown moving gratings. In order to investigate this relationship we employ computer simulations of simplified network models of L4 of the visual cortex 1 in macaque. We then show that the network is robust to noise, grating movement speed, grating spatial frequency and grating contrast. Furthermore it is demonstrated that the network can discernible angles of straight and dashed lines.

2 Introduction

In 1959 D. Hubel and T. Wiesel [HW59] investigated the primary visual cortex, the entry point of visual information into the brain. They show a cat various shapes on a screen and record single neuron activities. First the cat was anesthetized and fixated, then an electrode was inserted in its visual cortex. Responses of single cells were recorded under the presentation of different geometrical shapes. The strongest eliciting shape was a moving bar, upon which some neurons started firing rigorously, while other neurons remained silent. But when rotating the bar by 90° , the silent neurons became active, while previously active neurons showed no response anymore. They concluded that a neurons response strength is dependent on the angle of the moving bar. The functional dependency of a single neurons firing rate on the angle of a moving grating is captured by the so called tuning curve. The neurons preferred orientation can be found by determining the angle of highest elicited firing rate (Heggelund and Albus [HA78]). This allows to calculate the tuning curve for every neuron in the cortical layer also delivering the preferred moving-bar angle of each neuron. Color coding each neuron by their preferred grating angle results in an orientation map such as depicted by Bonhoeffer and Grinvald [BG93]. The orientation map is present in all layers of V1 in various animals such as the cat, monkeys and humans but for example not in mouse (Kaschube et. al. [KSL⁺10]). However, how the orientation map and the tuning curves are supported by the spatial connectivity of a neural network is still not fully understood.

3 Neuroscientific background

This section introduces basic neuroscientific concepts required to understand the problems and solutions presented in this work. We start with simple but crucial features of single neurons and work our way up to the connectivity and structure of large scale neuronal networks.

3.1 Cortical areas and layers

The brain is divided in several areas responsible for different computational abilities. These different cortical areas are composed of various layers that differ in cell densities and morphology (Brodmann [Bro09]). In the primary visual cortex the usual classification proposes six cortical layers: L1, L2, L3, L4, L5 and L6. Furthermore L4 may be split into L4C receiving a large amount of structured thalamic inputs and L4AB where only sparse and unstructured thalamic input is provided.

3.2 Single neurons

The brain is composed of independent but interconnected cells called neurons. They consist of three computationally relevant parts: the dendrites receive inputs from other neurons at the synapses altering the membrane potential (i.e. the electric potential between the cell and its surrounding) by the influx of ions. The received inputs are transmitted to the soma. If a certain threshold potential is crossed at the soma, a large, self-sustained deviation in the membrane potential is generated that travels along the axons where synapses to other neurons are located. This deviation is called action potential. Since its width is small with respect to other fluctuations in the membrane potential, it is abstracted to an event with a time stamp and referred to as spike. Only if the action potential reaches the synapses in the axons, a release of neuro-transmitters is triggered at the synapses. This results in the aforementioned influx of ions in the dendrites of receiving neurons. (Dyan and Abbott [DA01])

In computational neuroscience there exist many neuron models differing in their computational complexity and biological realism. One simple but computationally efficient and therefore widely used neuron model is the leaky integrate and fire neuron (LIF neuron). A LIF neuron has two key electrical potentials, the equilibrium or resting and the threshold potential. An unperturbed neuron sits at the equilibrium potential. Whenever the neuron receives a spike the membrane potential is kicked out of its resting potential and strives to get back to its equilibrium. We call this relaxation to the resting potential leak due to the loss of information about the spike over time. Crossing the threshold potential on the other hand emits a spike. Upon emitting a spike the membrane potential is reset to the resting state. Subsequently it is clamped there for about 2 ms

mimicking the refractory period. During the refractory period the neuron does not consider any inputs at all. LIF neurons are point like, meaning their dendrites and soma lie at the same point in space. (Dyan and Abbott [DA01])

Most studies use current based LIF neurons. A current based neuron changes its membrane potential by the same amount whenever receiving a spike. However, real neurons receive their charge via ion channels and hence there is no constant current flowing into the neuron. The current is dependent on the potential difference between extracellular potential and the membrane potential. Furthermore the chemical force depending on the ion concentrations plays a role. The conductance based leaky integrate and fire neuron (Bernander et. al. [BDMK91]) models two ion channels, one for positive charges and one for negative charges. We require two additional parameters compared to the current based model being the excitatory and inhibitory reversal potentials. These potentials are the equilibrium of the electro-chemical force located at around 0 mV and -70 mV sandwiching the resting potential. The name reversal potential stems from the experiment, no negative charge influx is observed at -70 mV when an inhibitory spike arrives. When going even below -70 mV the ion influx sign of an inhibitory synapse reverses and instead rises the potential. Excitatory neurons would show an analogous effect in an experiment. However, before reaching the excitatory reversal potential the threshold potential is reached and the neuron emits a spike. Across this thesis we use conductance based neurons. They provide two advantages above current based neurons. First, not arbitrarily small membrane potentials are allowed. And second, the sub-threshold dynamics are more realistic than in current base models.

$$C \frac{d}{dt} U(t) + [U(t) - U_r]G_l + [U(t) - U_e]G_e + [U(t) - U_i]G_i = 0 \quad (1)$$

$$G_s = \sum_k B_s \frac{t - t_k}{\tau_s} \exp(1 - \frac{t - t_k}{\tau_s}) H(t - t_k) | s \in e, i \quad (2)$$

Equation:1,2 shows the differential equation of a conductance based neuron. C is the capacity of the neuron, $U(t)$ resembles the membrane potential, $U_j | j \in e, i, r$ are the reversal potentials for excitation, inhibition and equilibrium. Furthermore $G_j | j \in e, i, r$ account for the excitatory, inhibitory and leak conductance's. t_k represent the time points of an incoming spike. The conductance is time dependently modeled with an alpha kernel showing a linear rise at $t = t_k$ and exponentially decaying at higher time values (Kuhn et. al. [KAR04]).

3.3 Neural networks

Integrating the knowledge about biological networks and determining the functional connection is one side of the modeling approach. The other side is the requirement of a powerful simulator precisely and efficiently simulating these biological models. For this reason the NEST Simulator (Gewaltig and Diesmann [GD07]) is used to simulate our networks. NEST is able to simulate large scale and densely connected neuronal networks with high adaptability of neuron and synapse models. Furthermore rather complex connection patterns may be achieved. Another advantage of using a simulator is the huge amounts of tests ensuring the correctness of the simulation and allowing comparability with previous networks written in NEST. We use a special version of the NEST simulator including Gabor filters (https://github.com/ackurth/nest-simulator/tree/V1V2V4_nest). In the following we briefly cover preceding networks relevant for this thesis.

3.3.1 Previous work

Based on anatomical and physiological data, Potjans and Diesmann constructed a multi-layered random network model of the somatosensory cortex (Potjans and Diesmann [PD12]). Simulations of this network model with LIF neurons show a ground state with realistic, layer-resolved firing rates.

Schmidt et. al. [SBH⁺18] adapted the model and changed it to V1 of macaque monkey by integrating data into a connectivity map. They build a spatial computational model of V1 accounting for realistic neuron and synapse densities of a 1 mm × 1 mm patch of each layer. This model is simulated without retinal input and reproduces the ground state activity of macaque monkey(Schmidt et. al. [SBS⁺18]).

Senk et. al. [SKD⁺22] further improved the model by extending it to 4 mm × 4 mm. In their analysis they focus on calculating the LFP's and MUA recordings comparing it with experimental data to show a comparable network state.

Antolik et. al. [ACR⁺18] describe a model similar to Senk et. al. [SKD⁺22] of 4 mm × 4 mm in L4 and L2/3. However, they worked with data from cat and reduced the synapses to 10% of realistic numbers. Additionally the network is coated with an orientation map. From the orientation map they determined the thalamo-cortical functional connections, which subsequently induce short range push-pull connections. Furthermore the orientation map mediates the long range patchy intra-areal connectivity. They then let a sinusoidal grating signal impinge from the thalamus to L4 and show that the network is orientation selective as well as contrast invariant.

4 Underlying model

This thesis is based on a network construction personally communicated by A. Kurth and J. Albers. For reasons of completeness and better understanding of the changes introduced in the course of this thesis, we give a detailed overview on the model construction. Kurth and Albers started with integrating a large amount of data using various studies to derive a realistic computational model of V1 of macaque monkey. First the number of neurons and synapses per area was extracted from Vanni et. al [VHWA20], which includes Beaulieu et. al. [BKS⁺92], Fitz-Patrick et. al. [FLB85], Giannaris and Rosene [GR12], Hendry et. al. [HSJY87] and O'Kusky and Colonnier [OC82]. Out of this information they calculated the number of synapses per neuron using a modified version of Peters rule from Binzegger et. al. [BDM04]. Synapses fall into three categories: thalamic synapses, cortico-cortical synapses and intra-areal synapses. Furthermore the intra-areal synapses were separated in the number of synapses connecting from each source layer to each target layer residing in V1. The data is used to construct a model of macaque V1 resolved by the layers L23, L3B, L4C, L4AB, L5 and L6.

They then endow the network with three different connection schemes for recurrent intra-areal synapses, the medium range isotropic connectivity, the long range patchy connectivity and the short range push-pull connectivity. Additionally the network possesses a structured thalamic input. The patchy connectivity, the push-pull connectivity and the thalamic inputs depend on the orientation map calculated by an artificial model.

4.1 Medium range isotropic connectivity

In order to derive a spatial connection profile from the synapses per neuron Kurth and Albers utilize the functional behaviour shown in equation:3. It determines the connections per distance proposed by Markov et. al. [MMF⁺10] covering connections on a medium range. Integrating the connection probability describing equation:3 and multiplying it with the target neuron density results in the number of synapses characterized by equation:4. S_{ij} is already known from previous calculations of Kurth and Albers. Therefore only equation:5 and λ_{ij} are required to calculate p_{0ij} . λ_{ij} may be determined by fitting equation:3 to connections per distance data from Packer and Yuste et. al. [PY11]. In the end they insert λ_{ij} into equation:5 to determine p_{0ij} .

$$p_{ij} = p_{0ij} \exp\left(-\frac{r}{\lambda_{ij}}\right) \quad (3)$$

$$S_{ij} = 2\pi\rho \cdot p_{0ij} \cdot \lambda_{ij}^2 \quad (4)$$

$$p_{0ij} = \frac{S_{ij}}{2\pi\rho \cdot p_{0ij} \cdot \lambda_{ij}^2} \quad (5)$$

Plotting the target neurons of one source neuron applying the medium range connectivity results in Figure:1. The source neuron (not shown) lies in the center of the blue shaded area and every blue dot represents one connection. For computational reasons they do not calculate the

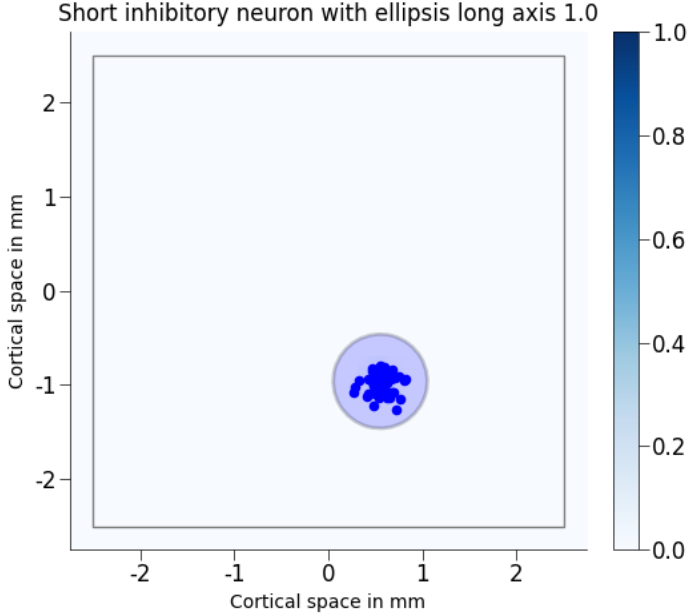


Figure 1: Connections of a cortical neuron with exponentially decaying connection probability. It is used to describe the medium range isotropic connection probability. The source neuron is not shown. Only connections in the blue shaded area of radius $4\lambda_{ij}$ are considered in order to higher the computational efficiency.

connection probability of two neurons being further apart then 4λ (light blue shaded are). This cut off omits less than 1% of the connections.

4.2 Long range patchy connectivity

Moreover Kurth and Albers covered the long range patchy connectivity, which is apparent in all layers except L4C. In contrast to the medium range isotropic connectivity, the patchy connectivity links neurons of similar preferred orientation organized in an orientation map (Stettler et. al. [SDBG02]). Patchy connections arise from axons of excitatory neurons and target neurons in an ellipse around the source neuron. The ellipses angle and the preferred orientation angle are the same (Bosking et. al. [BZSF97]). Angleucci et. al. [ALW⁺02] determined the ellipses long and short axis to be 3.3 mm and 2.2 mm in L4AB. In each ellipse Kurth and Albers assumed that the source neuron has a pairwise Bernoulli (Senk et. al. [SKD⁺22]) connection probability to connect to each possible target neuron. Since the total number of synapses is constrained, the parameter ψ is introduced determining which percentage of the synapses are patchy. Correspondingly the parameter p_{0ij} of the medium range connections is decreased. The in biology continuous orientation preference parameter is binned into 6 pieces. Since a bar is a 2-fold symmetrical object, the relevant angle space is 180° large. The bin difference therefore amounts to 30°. Furthermore patchy connections between different orientation preferences are omitted.

Figure:2 shows an orientation map depicting one source neuron in L4ABE (black dot) of 0° orientation preference asserting patchy connections to 5% of the other neurons of 0° preference in the patchy ellipse. Note that 5% is not the value for ψ . for example a ψ value of 40% would result in a connection probability of 3.7% to excitatory neurons. Patchy connections may only have an excitatory source, but excitatory and inhibitory targets.

4.3 Orientation map creation

As indicated in section:4.2 the patchy connectivity requires an orientation map assigning each cortical neuron a preferred orientation. Kurth and Albers therefore implemented an approach described by Sadeh and Rotter [SR14] to create an artificial orientation map.

Circular symmetric labeled object in Figure:3 shows the weight projection of a thalamic neuron or equivalently the receptive field of a potential cortical neuron, sitting in the center right below

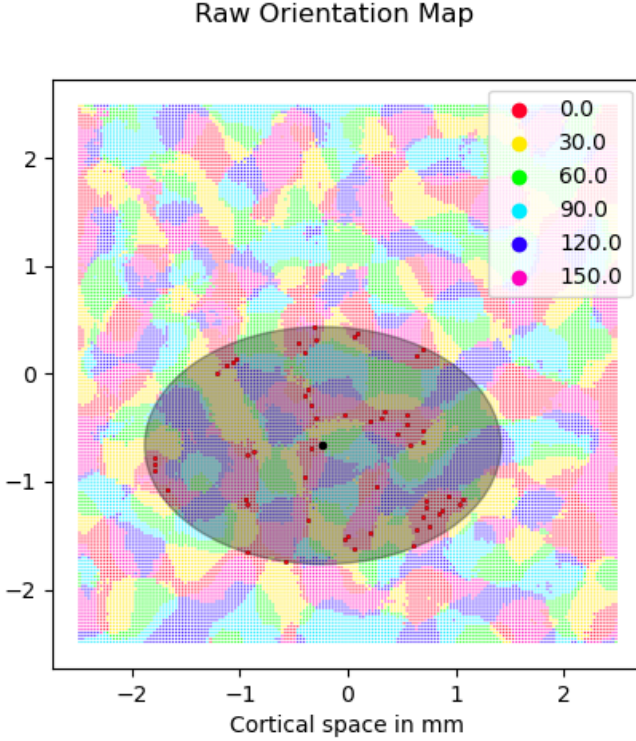


Figure 2: Visualization of a 0° neuron (Black dot) in L4ABE asserting patchy connections onto other 0° neurons (Highlighted red dots) lying in an ellipse (Dark shaded area) of 0° orientation. The connection probability in this example is uniform and amounts to 5%

the thalamic neuron. When a cortical neuron sits next to the single thalamic neuron (top left of fig:3) it receives circular symmetric input. Therefore it is independent on the thalamic input as a whole. In consequence it cannot be orientation selective. The other three configurations in Figure:3 show the superimposed projection of two thalamic neurons. A neuron in the yellow area receives input from both thalamic neurons. Taking for example the top right configuration, we notice that a bar of 0° would elicit both thalamic neurons at once. Hence each cortical neuron in the yellow area would receive their maximal input in this case and in consequence these neurons would prefer an orientation of 0° .

In order to build the dummy model, 2000 neurons per 1mm^2 (1000 per ON/OFF population) are distributed on the thalamic layer in a regular square grid. Then random positions for $3 \cdot 10^4$ neurons in the cortical layer are drawn. After superimposing both layers, each thalamic neuron connects to each cortical neuron with a weight spatially modulated by a 2D Gaussian. Since around 3 cortical neurons per thalamic neuron exist, a high correlation between nearby cortical neurons is induced. Therefore we expect a smooth spatial transition in the resulting orientation tuning (fig:5a).

In order to provide input to the system, Kurth and Albers modulated the thalamic current injected to the cortical layer. They use drifting sinusoidal gratings (fig:4) of the six orientations 0° , 30° , 60° , 90° , 120° and 150° . Meanwhile the spikes of every neuron in response to each grating are recorded.

Neurons fire in response to the thalamic currents. Their elicited rates depend on the overlap of the thalamic 2D shape projections. Each neuron's preferred orientation may be determined by counting the total number of spikes it emits during each of the two second long grating sweeps. Every neurons gets assigned the grating orientation it showed the maximal response to. The 2D map summarizing all these preferences together with their spatial position is called the orientation map. However, comparing the simulated and experimental measured orientation map by Bonhoeffer and Grinvald [BG93] shows a huge discrepancy. The simulated orientation map consists of tile like symmetrical elements. Meanwhile the experimental orientation map is largely heterogeneous.

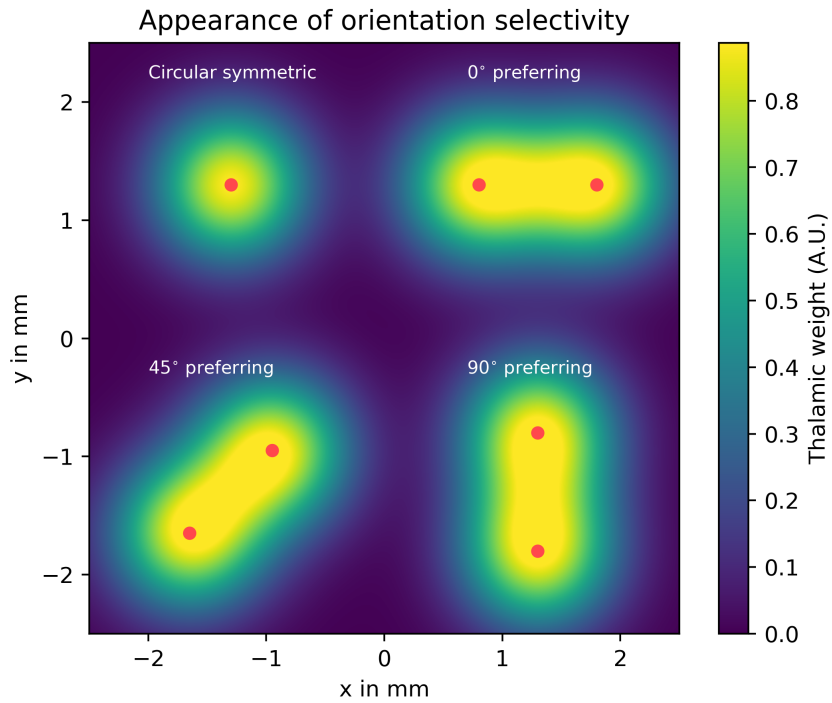


Figure 3: Projection of several thalamic neurons (red dots). The projection of a single neuron (top left corner) is of Gaussian shape. When two thalamic neurons come close to each other their projection overlaps and creates elongated patterns (top right, bottom left and bottom right corner). Neurons located in for example the yellow area of the top right thalamic overlap receive their strongest input when both thalamic neurons are activated at the same time. This happens when a bar of 0° moves over this vicinity. This plot is inspired by Figure 5C of Sadeh and Rotter [SR14]

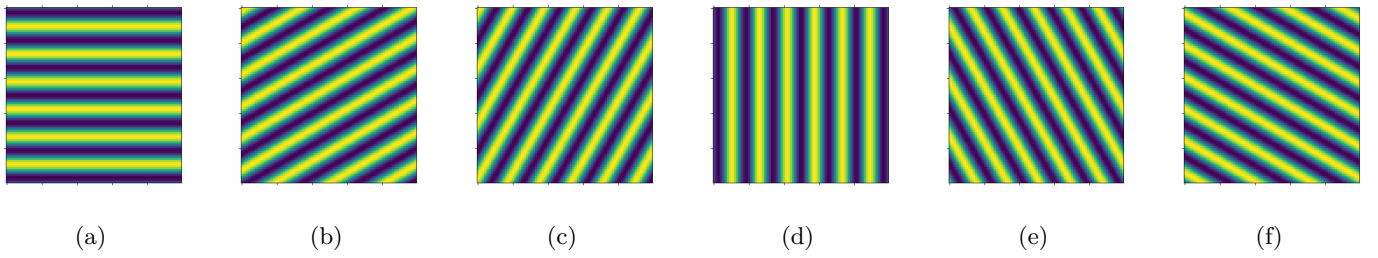


Figure 4: Grating input of a) 0° , b) 30° , c) 60° , d) 90° , e) 120° , f) 150° .

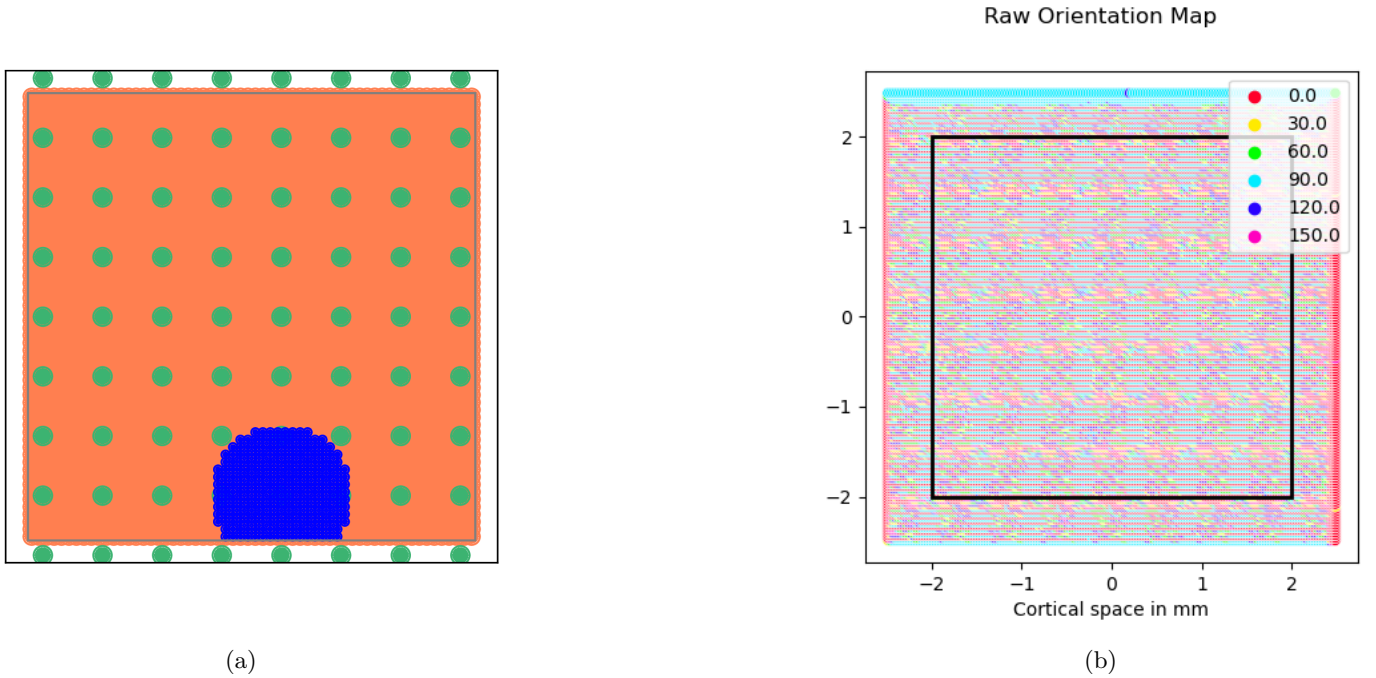


Figure 5: a) Dummy system implemented in the nest simulator. Jittered thalamic neurons (green) projecting to the cortical layer (orange). The projection of one thalamic neuron (Blue) is shown at the bottom. For better visibility the thalamic density is reduced. b) Resulting orientation map of an artificial system implementing thalamic neurons on a regular grid projecting onto a cortical layer.

Causing this problem is the highly symmetrical gridified thalamic layer. The symmetric thalamic neurons postpone their regularity to the cortical layer resulting in grid-like receptive fields. The problem may be solved by drawing random shifts (jitters) to the thalamic neurons in the x-y plane. This breaks the regularity as shown in figure:6a.

Figure:6 shows the orientation map created when the thalamic neurons are jittered instead of sitting on a regular grid. Another orientation map retrieve reveals a similar result as the experimentally measured one (Bonhoeffer and Grinvald [BG93]).

As indicated above, there exist two thalamic layers, the ON and the OFF layer. They are separated for easier handling when connecting to the retina in a later stage. ON cells prefer a bright dot with a dark surrounding. OFF cells work vice versa and prefer dark dots with bright surroundings. Section:6.1.2, Section:4.4 and Section:4.4.1 provide a more intricate view on the retina model, the push-pull connectivity and the thalamo-cortical connections.

The orientation map assigns, after smoothing, every point in cortical space a preferred grating orientation. Conceptually this is completely detached from any specific set of cortical neurons. Therefore it might be understood as a rule determining the preferred orientation of an arbitrarily located neuron in an arbitrary generated cortical layer.

4.4 Short range push-pull connectivity

Additionally to the medium range isotropic connectivity and the long range patchy connectivity Kurth and Albers endowed the network with the short range push-pull connectivity. It is mediated by the correlative input of thalamic afferents onto L4C. The push-pull implementation follows the description of Troyer et. al. [TKPM98], which provided both a simple thalamo-cortical model and the resulting push-pull connection formula.

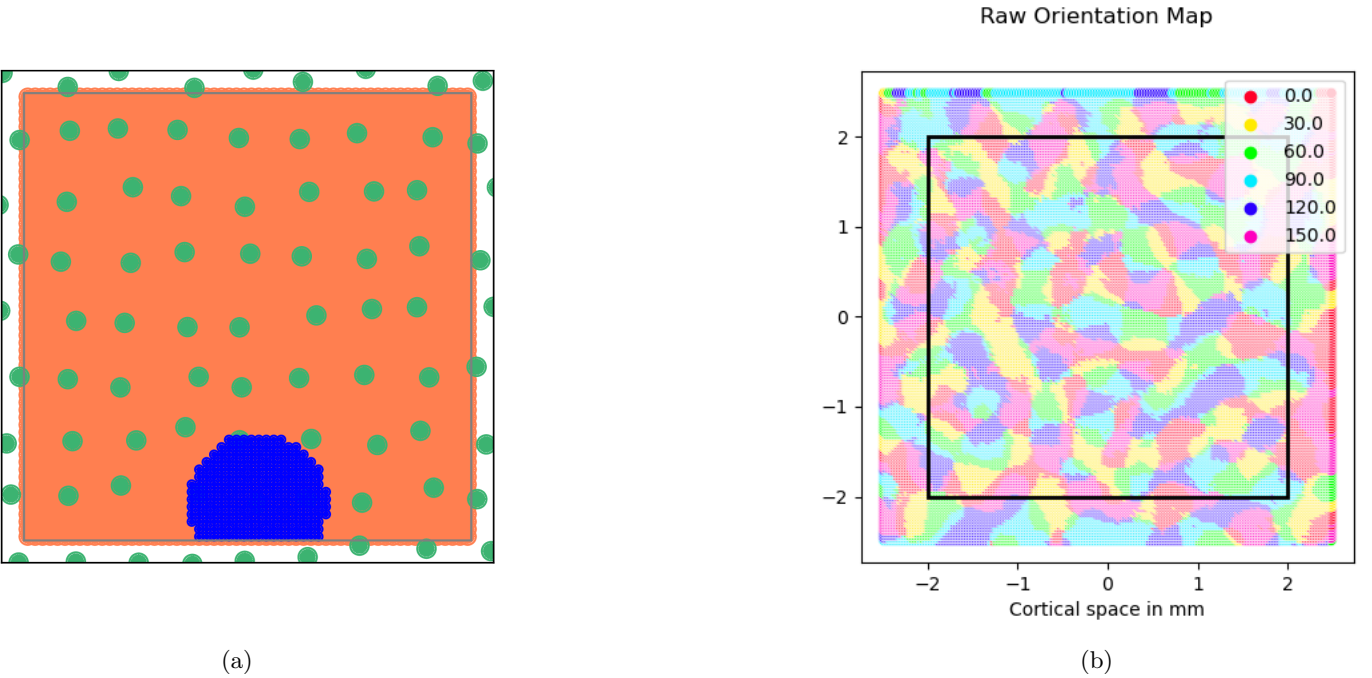


Figure 6: a) Dummy system implemented in the nest simulator. Jittered thalamic neurons (green) projecting to the cortical layer (orange). The projection of one thalamic neuron (Blue) is shown at the bottom. For better visibility the thalamic density is reduced. b) Resulting orientation map of an artificial system implementing jittered thalamic neurons projecting onto a cortical layer.

4.4.1 Thalamo-cortical connections

The orientation map creation provides the lgn positions for the thalamus. We use the previously generated ON and OFF lgn neurons. This is a slight deviation from Kurth and Albers, who did not use the correct lgn neuron density and furthermore do not split the dummy lgn in ON and OFF layers. The cortical size of $5\text{ mm} \times 5\text{ mm}$ allows for linear mapping from visual field to cortex. Structured input is only provided to L4CE_ON and L4CE_OFF. The projection from thalamic neurons to the cortex may be described by Gabor filters (fig:7a).

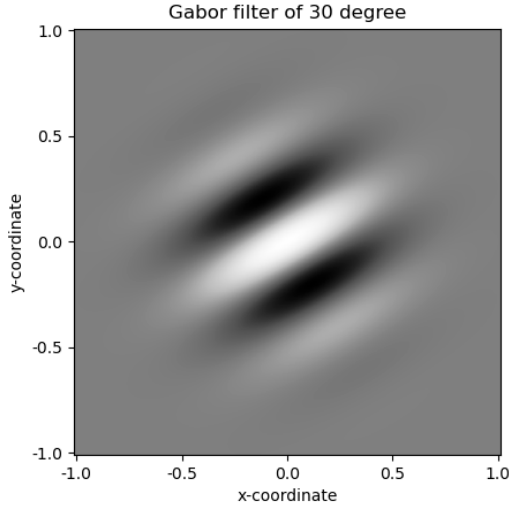
$$g(x, y, \lambda, \theta, \phi, \sigma, \gamma) = \exp\left(-\frac{x' + \gamma^2 y'}{2\sigma^2}\right) \cos\left(2\pi \frac{x'}{\lambda} + \phi\right) \quad (6)$$

$$x' = x \cos(\theta) + y \sin(\theta) \quad (7)$$

$$y' = -x \sin(\theta) + y \cos(\theta) \quad (8)$$

The connection profile is the underlying function determining the spatial connection probability a thalamic neuron has to the L4C neurons. Gabor filters may be described by seven parameters: θ determines the angle of the filters ellipse as depicted in Figureig:7a with 30° , the phase determines whether the Gabor centre is a peak or valley. Figure:7a shows the 0° phase corresponding to thalamic ON neurons, while a phase of 180° would characterize OFF neurons. The orientation map couples to the angle parameter and the phase to the ON and OFF identity of a thalamic neuron. Although the Gabor equation as written in equation:6 allows for negative values, negative probabilities do not make any sense. The ON thalamus connects to the L4C_ON where values are positive. Negative values on the other hand connect to L4C_OFF with a probability of the absolute value of the function. Correspondingly does the OFF thalamus connect the other way around to L4C. x and y are the distance in horizontal and vertical direction of target and source neuron. Palmer and Jones [JP87] found that $\gamma = 0.6$, $\lambda = 0.389\text{ mm}$ and $\sigma = 0.165\text{ mm}$. The only parameter left is the ellipse angle which is related to the orientation map and hence $\theta \in 0^\circ, 30^\circ, 60^\circ, 90^\circ, 120^\circ, 150^\circ$.

The problem of assigning θ arises due to the lack of knowledge how in biology the Gabor filter projection emerges. Also unknown is how or even if the interaction of many gabor filters creates the orientation map (Kenneth [Mil10]). But if the relation between the orientation map



(a)

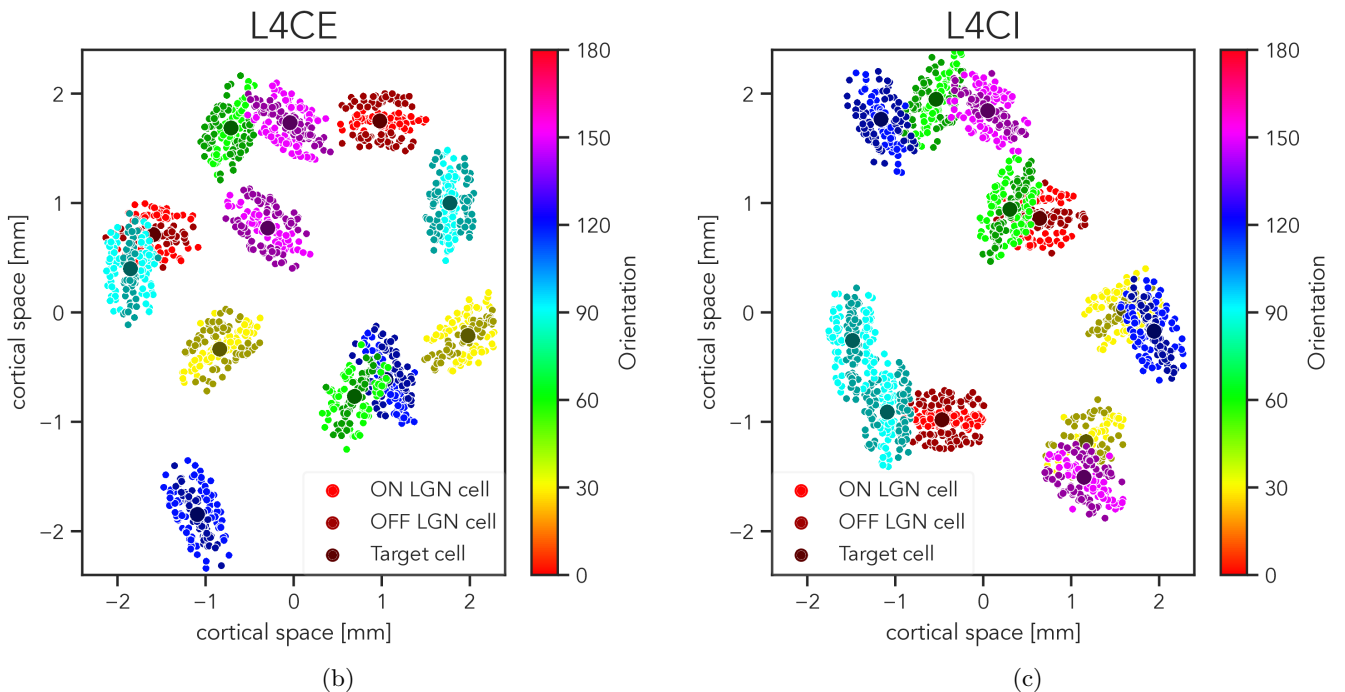


Figure 7: a) Gabor filter. A gabor filter is described by its angle (here 30°), its phase (here 0°), a wavelength and by the decay determining how strongly the amplitude decays with distance. b) Thalamo-cortical connection profiles of ON and OFF neurons in L4CE. c) Thalamo-cortical connection profiles of ON and OFF neurons in L4CI. (Figures b) and c)) were personally communicated by J. Albers.)

and the thalamic Gabor projection is unknown, Gabor angles may not be assigned forward from thalamus to the cortex. For this reason the prior knowledge of the artificial orientation map is required. It allows to circumvent the Gabor angle assignment problem by determining the connections backwards. Each cortical neuron searches for its thalamic sources instead of identifying the cortical targets of each thalamic neuron. The advantage of this reciprocal connection is that the Gabor angle for every cortical neuron is known. All the information is encoded in the orientation map. Every cortical neuron is connected with a Gabor angle equal to its preferred orientation to the thalamus. Since filtering with a Gabor filter is commutative the assumption that connecting forward and backward is an equal situation is validated. The backward case does work analogous to the ON OFF interaction in the forward case. When calculating the connections from for example L4C_OFF to the thalamus, areas of positive values correspond to the OFF thalamus and negative ones to the ON thalamus (fig:7b, 7c). The L4C_OFF to thalamus connections follow an in that sense inverse scheme. The connection weight is the same for every thalamo-cortical connection, the cortical orientation preference is solely achieved by the connection probability but not the synaptic strength.

4.4.2 Push-pull connections

Approximately 15 times more cortical neurons than thalamic neurons exists. In consequence each thalamic neuron will drive multiple nearby cortical neurons. In consequence these are correlated in their input. The split in ON and OFF cells furthermore induces cortical anti-correlated neurons. Utilizing the Hebbian rule (Hebb [Heb49]), correlation introduces stronger interconnection between correlated, and weaker interconnection between anti-correlated cortical neurons. But considering computational feasibility, calculating every correlation is non feasible. Therefore only the most prominent (anti-)correlations are implemented.

Let us imagine two nearby L4CE_ON_0 neurons. Since they both prefer the same drifting grating angle, they connect with the same Gabor filter function to the thalamus. Because they are so close to each other, both will receive almost identical thalamic inputs. If now one of these neurons fires through a thalamic stimulus, the other will almost certainly also fire. Therefore these neurons are positively correlated and establish connections between each other. Now we move one of the neurons to L4CE_OFF_0 while the other remains in L4CE_ON_0, but we keep the spatial position the same. Then according to the thalamic ON and OFF rate separation in picture:10 the one neuron will always receive a high input while the other always receives low input. They are almost perfectly anti-correlated and hence do not wire together.

Correlations arise through the overlap of Gabor filters in the input layer L4C. When Gabor filters of different angle overlap, a checkerboard pattern (Top row in fig:8) arises upon multiplication. The sum of all contributions (and hence the correlation) is close to zero. This is why we may neglect all correlations between two neurons that do not share the same orientation preference. Now we only focus on pre- and postsynaptic neurons having the same orientation preference. Two correlating neurons possess a positive sum of their multiplied Gabor filters. Two very close neurons basically have a perfect overlap (Bottom left picture in fig:8) resulting in the situation described in the previous paragraph. On the other hand a negative correlation arises, if we shift the spatial position of the post-synaptic by an odd multiple of half of the spatial wavelength ($(2n + 1) \cdot \lambda/2, n \in \mathbb{Z}$). The shift here occurs perpendicular to the Gabor filters Θ angle. Integrating all contributions results in a negative number accounting for a negative correlation. When we further shift the filters distance to a whole wavelength ($n \cdot \lambda, n \in \mathbb{Z}$) the correlation gives rise to strong positive correlations again (Bottom left picture in fig:8)

As pointed out above, the Gabor filter is the driving force of the push-pull connectivity. Furthermore knowing the parameters of the Gabor filter suffices to determine the push-pull connectivity. We may calculate the correlation between two neurons by determining the correlation coefficient of two Gabor filters as described in equation:9. From the result we notice that the correlation of two identical Gabor filters essentially is a Gabor filter again. However, the standard deviation is now different with $\sqrt{2}\sigma$ and an additional constant multiplication pre-factor arises. To connect cortical neurons with each other we need to translate the correlation function into a probability function. Nevertheless, it is unknown how many connections the correlation actually causes. Therefore the constant pre-factor of the correlation function requires separate calibration without

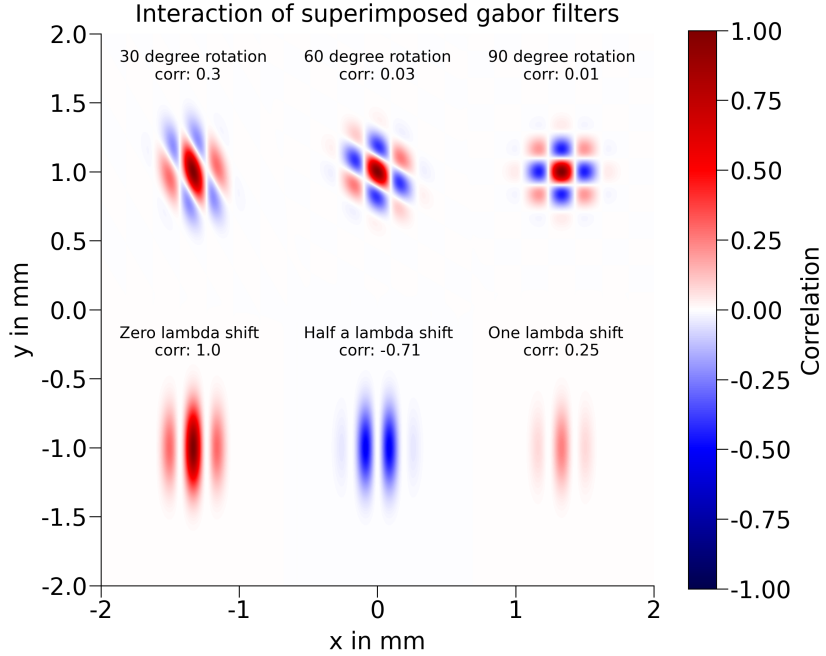


Figure 8: Shared input overlap of two neurons residing in the ON layer under rotation and perpendicular shift. When rotating the preferred angle of one of the neurons, a checkerboard pattern arises. Shifting the spatial distance perpendicular to the preferred orientation mediates strong correlation, when moved by a whole wavelength. However, strong suppression arises under a shift of half a wavelength

any dependence on the constant occurring in equation:9. The total number of connections in L4C is well constrained such that an increase of push-pull connections must coincide with a decrease in isotropic connections. We split the total number of synapses in L4C between the isotropic and the push-pull connectivity. From this constrain and tests for the fraction of push-pull connections that stabilizes the network and orientation map the most (see sec:7.5), we consistently determine the pre-factor.

$$\begin{aligned}
\rho_{ab}(x_s, y_s) &\sim \int_{-\infty}^{\infty} \int_{-\infty}^{\infty} g(x, y) \cdot g(x + x_s, y + y_s) dx dy \\
&= \int_{-\infty}^{\infty} \int_{-\infty}^{\infty} \exp\left(-\frac{x^2 + \gamma^2 y^2}{2\sigma^2}\right) \cdot \exp(i(2\pi \frac{x}{\lambda} + \psi)) \\
&\quad \cdot \exp\left(-\frac{(x + x_s)^2 + \gamma^2(y + y_s)^2}{2\sigma^2}\right) \cdot \exp(i(2\pi \frac{x + x_s}{\lambda} + \psi)) dx dy \\
&= \int_{-\infty}^{\infty} \exp\left(-\frac{(\sqrt{2}x + \frac{1}{\sqrt{2}}x_s)^2}{2\sigma^2}\right) \cdot \exp(i(2\pi \frac{2x}{\lambda} + 2\psi)) dx \cdot \int_{-\infty}^{\infty} \exp\left(\frac{\gamma^2(\sqrt{2}y + \frac{1}{\sqrt{2}}y_s)^2}{2\sigma^2}\right) dy \\
&\quad \cdot \exp\left(-\frac{\frac{1}{2}x_s^2}{2\sigma^2}\right) \cdot \exp(i(2\pi \frac{x_s}{\lambda} + \psi)) \cdot \exp\left(-\frac{\gamma^2 \frac{1}{2}y_s^2}{2\sigma^2}\right) \\
&= \text{const} \cdot \exp\left(-\frac{x_s^2 + \gamma^2 y_s^2}{2(\sqrt{2}\sigma)^2}\right) \cdot \exp(i(2\pi \frac{x_s}{\lambda} + \psi))
\end{aligned} \tag{9}$$

Above we found out that depending on the location of both neurons (ON or OFF layer), the correlation must be positive or negative. The missing accessory is considered by a phase shift in ψ of the Gabor filter which equates a sign change in front of the function. Changing the layer (ON or OFF) of the pre- or post-synaptic neuron or the efficacy (E or I) of the pre- synaptic neuron gives rise to a phase shift of π . The equation:10 covers all eight possible cases and assigns the Gabor filter describing the correlation to them.

$$\begin{aligned}
p_{\text{ON},\text{ON}}^{\text{E}}(x,y) &= p(\Delta x, \Delta y, \lambda, 0, \gamma, \sqrt{2} \cdot \sigma) \\
p_{\text{ON},\text{OFF}}^{\text{E}}(\Delta x, \Delta y) &= p(\Delta x, \Delta y, \lambda, \pi, \gamma, \sqrt{2} \cdot \sigma) \\
p_{\text{ON},\text{ON}}^{\text{I}}(\Delta x, \Delta y) &= p(\Delta x, \Delta y, \lambda, \pi, \gamma, \sqrt{2} \cdot \sigma) \\
p_{\text{ON},\text{OFF}}^{\text{I}}(\Delta x, \Delta y) &= p(\Delta x, \Delta y, \lambda, 0, \gamma, \sqrt{2} \cdot \sigma) \\
p_{\text{OFF},\text{OFF}}^{\text{E}}(\Delta x, \Delta y) &= p(\Delta x, \Delta y, \lambda, 0, \gamma, \sqrt{2} \cdot \sigma) \\
p_{\text{OFF},\text{ON}}^{\text{E}}(\Delta x, \Delta y) &= p(\Delta x, \Delta y, \lambda, \pi, \gamma, \sqrt{2} \cdot \sigma) \\
p_{\text{OFF},\text{OFF}}^{\text{I}}(\Delta x, \Delta y) &= p(\Delta x, \Delta y, \lambda, \pi, \gamma, \sqrt{2} \cdot \sigma) \\
p_{\text{OFF},\text{ON}}^{\text{I}}(\Delta x, \Delta y) &= p(\Delta x, \Delta y, \lambda, 0, \gamma, \sqrt{2} \cdot \sigma)
\end{aligned} \tag{10}$$

Here we use that a phase of 2π is equivalent to a phase of 0 (equation:10 adopted from Kurth and Albers)

4.5 External input

The visual cortex of macaque approximately has a size of 1200 mm^2 (Vanni et. al. [VHWA20]) while Kurth and Albers network only accounts for around 16 mm^2 . However, the visual cortex is strongly interconnected with itself and with other cortical areas. In consequence omitting all neurons and synapses of the non modeled cortical parts drastically reduces the input which cells in our down scaled network receive. Hence a correction of the missing input by adding random background activity is required. The external input contributes to driving the network, but is not allowed to carry any information itself. Kurth and Albers therefore introduced Poisson generators which generate Poisson distributed spike trains. They modulate them by the parameter background rate, which controls the Poisson neurons firing rate.

5 Research questions

As described above (sec:3.3.1), there exist many efforts to build neural networks as biologically realistic as possible. The earlier studies were more concerned about creating large scale computational feasible models reproducing a stable activity. Subsequently connectivity patterns recreating realistic ground states of neural activity were developed. Following that, specific connectivity patterns and simple input models were developed focusing more about the dynamical state.

We want to extend these previous approaches by enhancing the biological plausibility and capability of the driven state. We therefore build on a network presented by Kurth and Albers, however, we only use L4AB and L4C for reasons of computational feasibility. On the one hand we want to find out how to correctly calibrate the already existing parameters as for the patchy and push-pull connectivity. On the other hand we want to add further experimental connection patterns. The goal of these connectivity patterns is to retrieve the orientation map and to create steep tuning curves. Furthermore the question of how each connectivity scheme individually affects the orientation tuning arises. Are additional assumptions about connectivity and weights required to achieve the desired state? Is the network also tuned to other inputs then drifting gratings and if not, what is required to achieve this sensitivity?

The books understanding vision [Li14] and spatial vison [Li00] by Zhaoping Li show that dashed lines are observed as a coherent object. Therefore in the cortex iso-orientation domains of preferred angle that are not directly activated by the thalamus must be elicited. In L4AB exists the patchy connectivity which asserts long-range connections between iso-orientation domains of same preferred angle. We hypothesize that the patchy connectivity and the above described feature of the cortex are related.

Beyond the computational feasibility, the choice of sub layers from the model of Kurth and Albers allows for addressing these questions. L4C is the primary layer of visual input in V1 (Vanni et al. [VHWA20]). From L4C the incoming activity is spread to the other layers, among them L4AB that shares anatomical features with the layers outside L4. Thus L4, split into L4AB and L4C, allows

for addressing the stated research questions.

6 Methods

The methods section is split into two parts: i) the extensions and modifications to the model of Kurth and Albers and ii) the analysis of the network activity. The former describes the calibration of already implemented features as well as additional connectivity patterns added to the model. The latter concerns about both, well established measures of network activity and new measures specifically tailored to for example simulated spatial network activity.

6.1 Extensions and modifications

In the following we describe a model of layer 4 in macaque monkey. It is the primary visual input receiving layer located in V1. For reasons of computational feasibility the area of 25 mm^2 ($5 \text{ mm} \times 5 \text{ mm}$) in the centre is used. Compared to that, a macaque monkey possesses around 1200 mm^2 (Vanni et. al. [VHWA20]). The small cortical tissue under a patch of 25 mm^2 surface of layer 4 represents the central field of vision. Another advantage of using a small part of layer 4 is that the retinotopic mapping becomes easier. Retinotopic mapping describes the characteristic of overlapping receptive fields nearby cortical neurons in L4 show. In general more retinal centralized points are mapped on a larger part of the cortex, than retinal off center points are. Conveniently, when cutting out only a small piece out of the center, retinotopic mapping is approximately linear, if we approximate the function found by Daniel and Whitteridge [DW61] (Equation:11).

$$f(\theta) = 180 \cdot M \sin(\theta) \text{ mm} \quad (11)$$

Furthermore we neglect the magnification factor such that we just super impose thalamic and cortical layer.

This thesis is based on a scale-able model of V1 of macaque monkey build by Kurth and Albers. For its possibility to efficiently simulating large spiking neuron assemblies, we use the NEST simulator (Gewaltig and Diesmann [GD07]). The efficiency is required to implement realistic connection profiles while sufficiently reproducing large scale mechanisms such as the orientation map (sec:2) and in particular to adequately implement the long range patchy connectivity.

6.1.1 Correction for V1 inputs

Since we limit our adapted model to layer 4 of V1, the omitted layers 2/3, 3, 5 and 6 must be replaced by an external input. Replacing each external neuron by a Poisson process provides for both, the simplest realization and the least correlation structure. The argumentation for poisson generators is the same as for the external input (sec:4.5). We use the connectivity evaluated by Kurth and Albers to account precisely for the number of corrected connections. First we notice that each neuron in L4 would receive several hundreds of synapses from the external layers. However, all of these synapses carry as assumed per definition independent Poisson processes. Adding two Poisson processes with rates ν_1 and ν_2 results in another Poisson process with rate $\nu_1 + \nu_2$. Let us now look at a neuron in L4 receiving for example 100 connections from neurons in the external V1 layers and assume that each of these neurons carries its layers average firing rate ν_{mean} . We then might replace these 100 neurons by one neuron with firing rate $\nu = 100 \cdot \nu_{\text{mean}}$. Since all neurons in each of the six L4 sub-layers receives the same amount of synapses, each of them might be replaced by a Poisson generator with rates $\nu = \nu_{\text{mean}} \cdot \text{num_conns}_{ij}$. Here num_conns_{ij} represents the average number of connections from external layer j to a L4 sub-layer i.

6.1.2 Retina Model

The model proposed by Kurth and Albers used the thalamus as input instance. However, in biology the retina is the first instance of image processing. The retina is the link between the visual world and the brain, every signal is processed by it before entering the thalamus. Rod and cone cells in the retina process intensity and wavelength information. For reasons of simplicity and computational efficiency only cone cells are considered. The resulting network is grey-scale driven. Rod cells basically perceive the lights intensity and postpone that information to the thalamus, which translates it into spikes. Technically we model the retina by performing a filter operation on an arbitrarily given picture. The filtered pictures intensity is translated into firing rates of thalamic ON and OFF neurons.

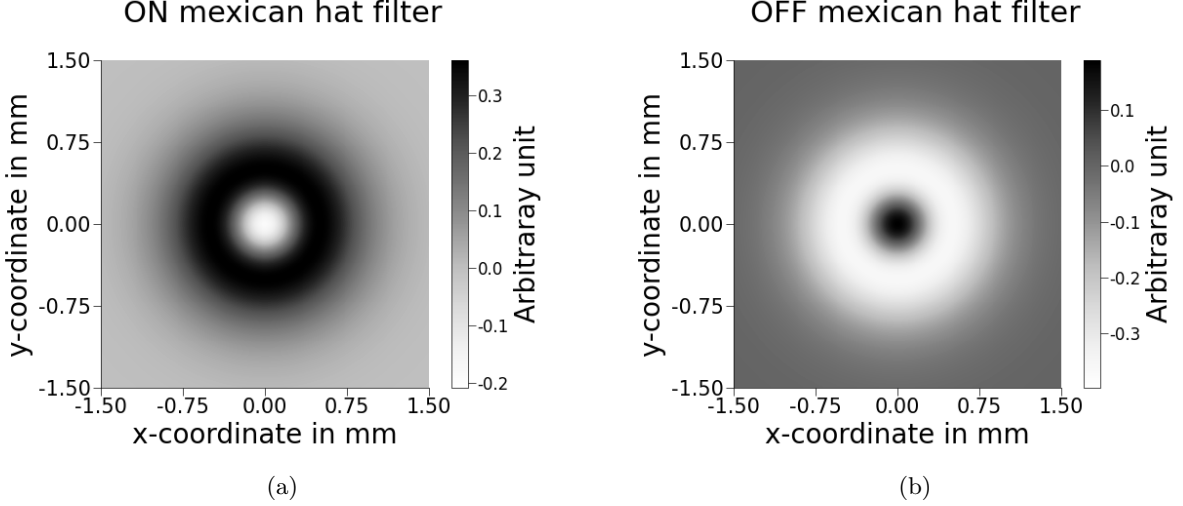


Figure 9: a) Mexican hat ON filter kernel. Equivalently this function represents the receptive field of the thalamic neurons. b) Mexican hat OFF filter kernel.

Each rod cell in the brain receives an intensity signal and postpones it to the thalamic layer. Each thalamic neuron receives input from multiple rod cells weighted by a lateral distance dependent function. We might describe this behaviour by an equation functionally behaving as the following (Understanding Vision [Li14]):

$$O = \text{baserate} + \sum_{x,y} S(x,y) \cdot K(x,y) \quad (12)$$

Where O is the rate of the thalamic neuron. $S(x,y)$ is the intensity of the rod cells and $K(x,y)$ the smoothing kernel. The smoothing kernel has a Mexican-hat like shape, which itself consists of the difference of two Gaussian functions (eq:13).

$$K(x,y) = \frac{\omega_c}{\sigma_c} \exp\left(-\frac{x^2 + y^2}{2\sigma_c^2}\right) - \frac{\omega_s}{\sigma_s} \exp\left(-\frac{x^2 + y^2}{2\sigma_s^2}\right) \quad (13)$$

Mexican-hat-functions may have one of two types of flavors when observed in the thalamic context. Either they are "ON" (fig:9a) or "OFF" (fig:9b) depending on the parameter choice. An ON cell fires rigorously when presented a bright dot with a dark surrounding and an OFF cell vice versa. All ON cells filter the given picture with an ON filter. Meanwhile all thalamic OFF neurons filter with an OFF filter ultimately creating two split inputs for each picture (fig:10).

The rates calculated by equation:12 in the thalamic ON layer show high values at areas of high intensity and vice versa, whereas in the OFF layer high rates are observed at low intensity areas. In the highly symmetrical case of a grating, the OFF layer is the negative of the ON layer (fig:10) and a 180° phase shifted version of the ON layer. Filtering a highly asymmetrical picture, however results in an edge detected version of this picture (fig:14).

6.2 Hebbian inspired weight modulation

Previously we accounted solely for the connection probability of pairwise interactions, but completely ignored the connection weights. The simplest network configuration (as for example in Kurth and Albers) would draw the weight for every synapse from the same Gaussian distribution. Indeed this makes sense in the case of push-pull and patchy connections, because all target and source neurons possess the same orientation preference. However, in the medium range isotropic connectivity, neurons of different preferred orientation interact with each other. Therefore Billeh et. al. [BCG⁺20] proposed to modulate the connection probability and weight of all connections dependent on the orientation preference difference $\Delta\theta$. We choose a slightly different ansatz and do not modulate the connection probability, but only the weight of all connections. Different

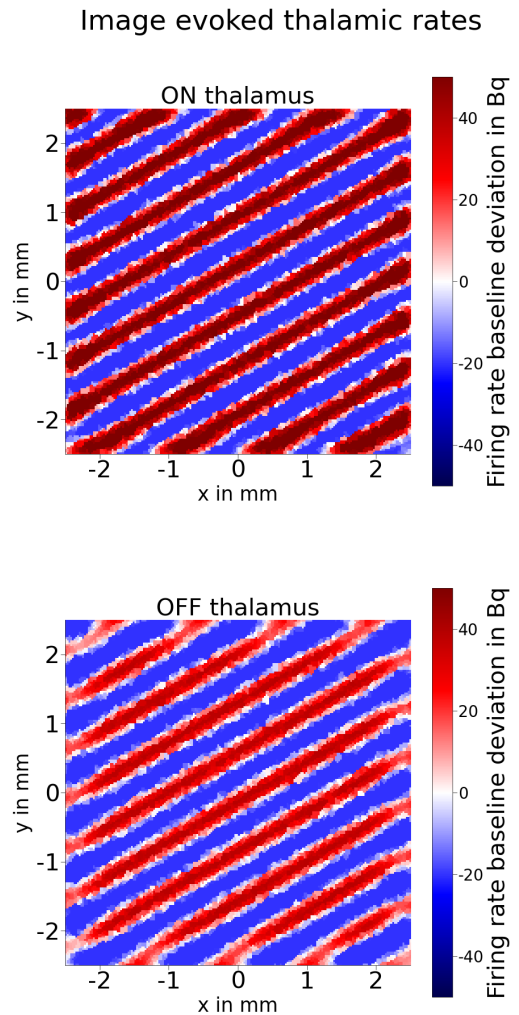


Figure 10: Thalamic ON and OFF input received by filtering the grating 4a with ON (fig:9a) and OFF (fig:9b) kernels. The Retina model translates the intensity into thalamic firing rates, which drive the cortical layer. This picture depicts the filter part of equation:12, the base rate accounts for 20 Hz. Since negative rates do not make any sense there are no firing rates below -20 Hz in the baseline deviation.

realizations are chosen dependent on the source neurons efficacy. We justify the weight modulation by arguing with Hebb's rule, which states that "neurons that fire together wire together" (Hebb [Heb49]). This implies both, a higher quantity and a higher weight between positively correlated neurons. Hebb's rule is related to spike time dependent plasticity (STDP Bi and Poo [BP98]) describing the strengthening of a synapse when the target neuron spikes shortly after receiving a spike from the source neuron. However, our synapse distribution is unchanged due to the computational non-feasibility of redistributing the synapses accordingly. Hebb's "rule" might be understood more as a loose but widely applicable principle than a strict rule to force on the network.

In our case we notice that neurons with the same preferred orientation should strongly fire when shown their preferred moving grating. Meanwhile neurons with different preference should not fire together. For example a connection between two 0° neurons would then have according to Hebb's rule a strong weight. Whilst a connection from 0° to 90° should be rather weak. We propose the existence of a smooth curve determining the isotropic weight dependent on the orientation preference difference of source and target neuron based on Hebb's rule. Experimentally preliminary boundary conditions on the possible functions one could use only exist sparsely. Therefore we are relatively free to choose our own function. However, there are a few logical restrictions on the possible functions. First it must be symmetric due to the symmetry in the Gabor filter. Second it should have a peak value at $\Delta = 0^\circ$ and a valley at $\Delta = 90^\circ$. And at last the convergence "speed" from peak to valley should be modulateable. Equation:14 is one possibility satisfying all requirements. W_{0ij} describes the base source and target layer dependent peak conductance (eq:1,2) which we usually set to 0.0046 nS. W_{Hj} and W_{Lj} are the high and low peak conductance's and $Width_j$ controls how fast the weight converges to its lower boundary. All three depend on the efficacy of their source population j . Figure:11 shows one realization of the weight modulation using example parameters.

$$W(\delta_\Theta) = W_{0ij} \cdot \left(W_{Hj} - \frac{(W_{Hj} - W_{Lj})}{\exp\left(\frac{(\Delta_\theta - 90^\circ)^2}{Width_j^2}\right)} \right) \quad (14)$$

Another break of the efficacy's symmetry is possible by directly controlling the weights of $E- > E$, $E- > I$, $I- > E$ and $I- > I$, where a factor of 1 represents the initial case of 0.0046 nS, a factor of 2 then equals an amplitude of 0.0092 nS etc. Furthermore we introduce for traditional reasons the g factor, which is the very same as changing the $I- > E$ and $I- > I$ factor at the same time by the same value. In random balanced networks (Brunel et. al. [Bru00]) a g factor of 4 to 5 is required to stabilize the firing rates.

6.3 Elliptical connectivity

While the exponential distance dependent connection probability model (sec:4.1) fitted well with excitatory source neurons in Kurth and Albers analysis, it fails to adequately describe inhibitory neurons (not shown here). Additionally some experiments find inhibitory connection profiles to be rather elliptical than circular in certain brain areas. For example Peng et. al. [PTP⁺21] who investigate the rat presubiculum find elliptical connection profiles of inhibitory neurons. They furthermore show that the elliptical profile is advantageous over circular projecting neurons in discerning angle inputs. Of course it is not simply possible to draw conclusions from features in rat presubiculum and apply them to macaque V1. But we may vindicate the inferring by outlining the crucial similarities of structure and purpose in the presubiculum and V1. The orientation map is V1's pivotal point assigning every neuron a preferred orientation. Meanwhile the head tuning map (Taube [Tau07]) of presubiculum does a very similar thing of assigning every neuron a preferred head orientation angle. Essentially both perform the very same computational task of reacting to the angle of their input. Exactly that is their crucial difference, the input. While the thalamus receives input from the visual field, the presubiculum receives input from the rat's head position. Nevertheless, since there is no huge difference between the layers function themselves, it seems likely that the brain would solve a similar problem with a similar solution. Therefore it is justified to test the effect of elliptical inhibitory neurons. We adjust the circular connectivity from eq:1 to eq:15. Although it seems legitimate to implement elliptical inhibition inferred from rat data, we may not simply take the exact ellipsis parameters from [PTP⁺21] as they possibly could vary dramatically across species.

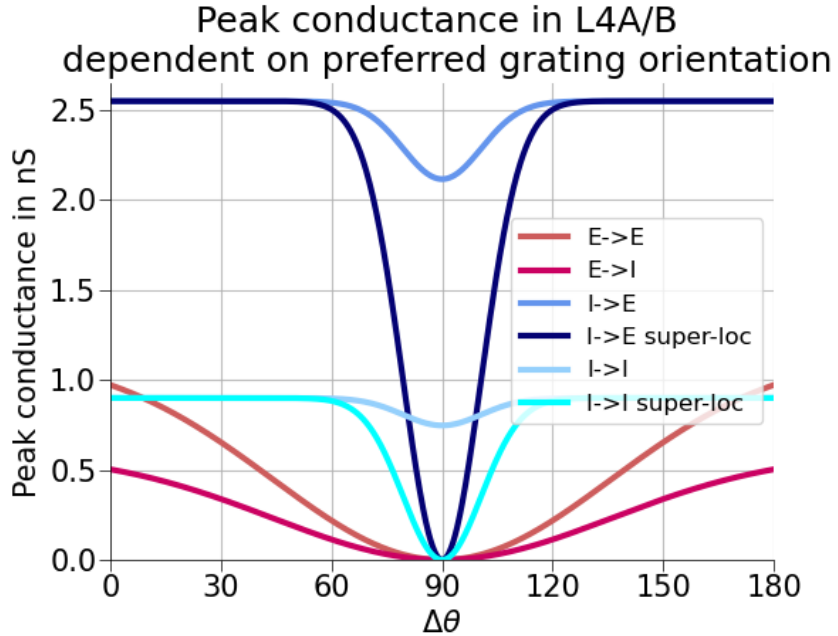


Figure 11: Quantitative representation of the peak conductance (eq:1,2) between two neurons dependent on their efficacy and preferred angle difference in the Hebbian inspired scheme (eq:14). All neurons possess their highest conductance if they target neurons of same preferred orientation and their weakest conductance peak when connecting to neurons with an orientation preference difference of 90°. Note that the peak conductance is not the same as the evoked PSP and from this plot one can not infer that inhibition is stronger than excitation. For the evoked PSP see Figure:40, 39

$$P = P_{0AB} \cdot \exp\left(\sqrt{\left(\frac{\Delta x \cdot \cos(\phi) + \Delta y \cdot \sin(\phi)}{c \cdot \lambda_{AB}}\right)^2 + \left(\frac{\Delta x \cdot \sin(\phi) - \Delta y \cdot \cos(\phi)}{d \cdot \lambda_{AB}}\right)^2}\right) \quad (15)$$

p_0 and λ of equation:15 have the same interpretation of zero distance probability and decaying strength as in the circular connectivity (eq:3). However, three additional parameters are required to describe an ellipse. ϕ determines the ellipse orientation and c and d determine the long and short axis of the ellipse. But the constrain of having a fix number of synapses reduces the degrees of freedom to two.

$$N_{conn} \propto \int_0^\infty \int_0^\infty p(x, y) dx dy = \int_0^{2\pi} \int_0^\infty r \cdot p(r) dr d\phi \quad (16)$$

Figure:12 shows the connections per distance an elliptical neuron asserts. Meanwhile Figure:13b depicts the spatial connections of one elliptical inhibitory neuron with ellipses angle of 0°. When reaching higher ellipses long axis values, the connections per distance curve flattens and has a less prominent peak, meaning the connections are more uniformly distributed over the distance from the source neuron.

The relation of N_{conn} being constant is satisfied when $c = \frac{1}{d}$ (eq:16), therefore knowing the ellipse angle and the long axis is sufficient for a full description of the ellipse. Some notices on the elliptical inhibition profile:

1. I. e. a long axis of $c = 2$ will result in a connection probability along the ϕ axis being stretched by a factor of 2 and a stretching perpendicular to the phi axis of $\frac{1}{2}$.
2. A long axis of $c = \frac{1}{2}$ equals the situation of a long axis of $c = 2$ but with a ϕ shift of 90°, therefore only the ellipse space for $c \geq 1$ is relevant.
3. the average connection distance increases with increasing long axis (fig:12).
4. When setting $c = 1$ and $d = 1$ the connection probability collapses to the circular symmetric

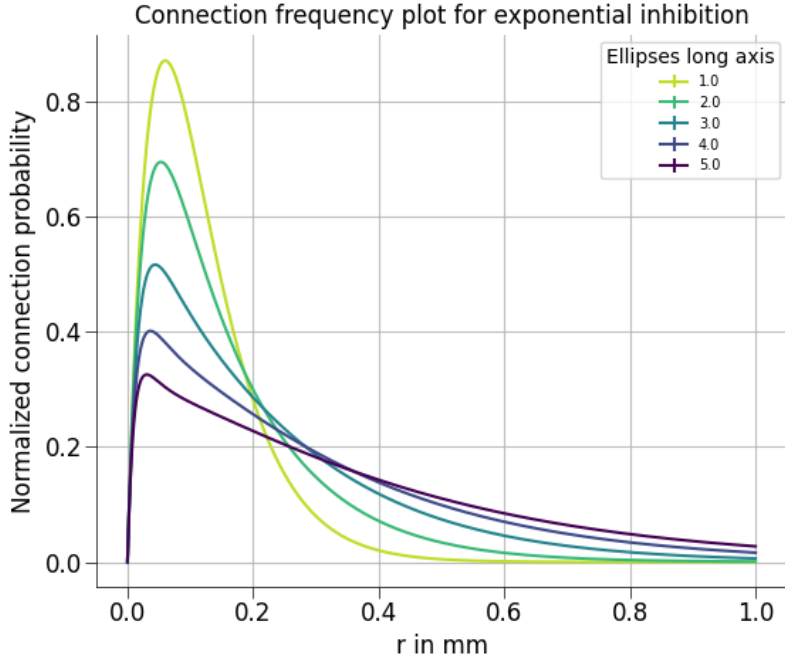


Figure 12: Normalized connections per distance an inhibitory neuron asserts dependent on its ellipses long axis averaged over the radial angle. With higher ellipses long axis, the curve gets more flattened and the average connection distance increases.

case eq:3.

Now we are left with the task of finding appropriate parameters for ellipsis angle and long axis. Peng et. al. [PTP⁺21] do not provide any data on how the ellipses angles are aligned. Therefore the easiest and hence most probable solution of drawing every inhibitory neurons ellipsis angle randomly is used. The continuous 180° ellipsis angle space is split into 10 discrete equally distant angles and every inhibitory neuron is randomly assigned one of these angles.

We already argued that rat and macaque might be too different to simply adopt the ellipsis long axis from the presubiculum. Nevertheless, we calculate the ellipsis long axis from Peng et. al. [PTP⁺21] to have a first guess of the order of magnitude. Peng et. al. [PTP⁺21] define the polarity index of an ellipse as $polarity = \frac{c}{d}$ with the long axis c and the short axis d. Since in our model $c = \frac{1}{d}$, the polarity simplifies to $polarity = c^2$. This then lets us transform the measured polarity of around 6 to 10 to a long axis of 2.5 to 3 (fig:13b).

6.3.1 Super-localized inhibition

The isotropic connectivity solely depends on the distance of source and target neuron. This random model does not consider for specific connection motifs found in experimental data such as in Peng et. al. [PTP⁺21]. One striking result they find is that inhibitory neurons which target an excitatory neuron will likely be targeted back. Such connectivity's are called "reciprocal motifs". We hypothesize that "reciprocal motifs" balance the networks activity, because they suppress active rather than random neurons. We want to test the effect by increasing the number of "reciprocal motifs". An intuitively implementation would consist of first connecting the E to the I population. Subsequently the sources of every I neuron would be printed out and finally an corresponding backwards connection would be added. However, doing so for hundreds of thousands of neurons is computationally impossible with the currently available soft and hardware. In consequence a computationally more efficient way is required. We utilize the spatial component of our network and implement a new connectivity scheme called super-localized inhibition. A controllable percentage of the inhibitory neurons is super-localized. This refers to neurons connecting with a 100% chance to excitatory neurons in a certain radius and with a 0% chance to neurons outside this radius (fig:13a).

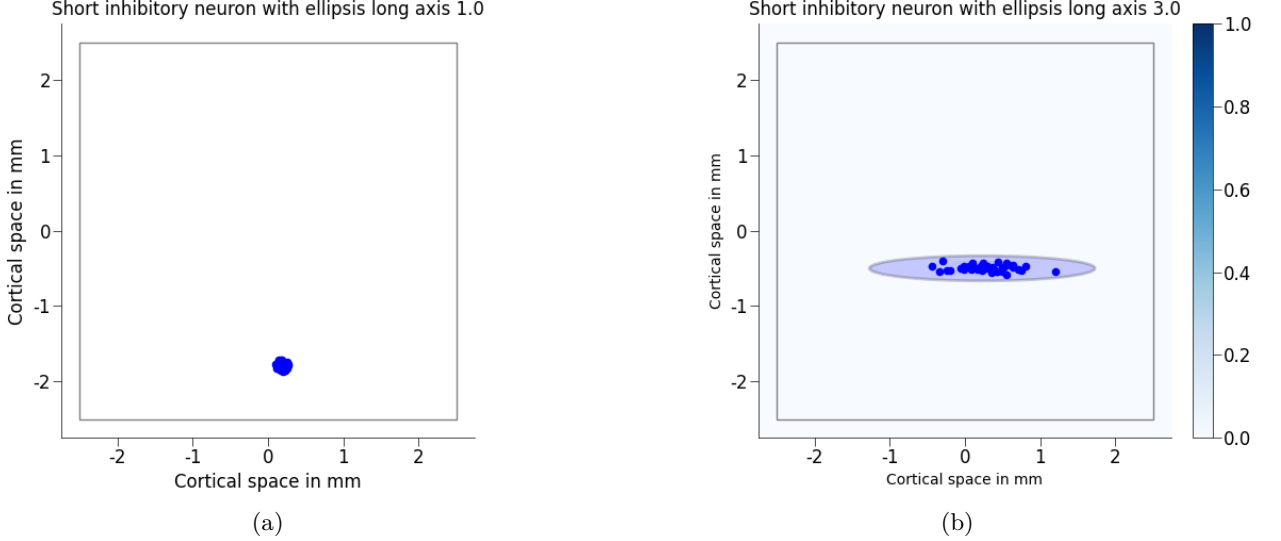


Figure 13: a) Target neurons of one super-localized inhibitory neuron with ellipsis long axis of 1.0.
b) Target neurons of one non super-localized inhibitory neuron with long axis of 3.0.

Since again the number of asserted synapses must stay constant it is possible to calculate an effective radius (eq:17). The super-localized inhibitory neurons only act on a pretty local scale compared to all other neurons. Hence vindicating the name super-localized. The number of "reciprocal motifs" super-localized neurons participate in is strongly enhanced because each excitatory neuron is targeted by all inhibitory neurons in a certain radius.

$$2\pi \cdot \int_0^\infty p_0 \cdot r \cdot \exp\left(-\frac{r}{b}\right) dr = 2\pi \cdot \int_0^\infty 1 \cdot r \cdot \Theta(r - R_{loc}) dr$$

$$p_0 \cdot b^2 = \frac{R_{loc}^2}{2}$$

$$R_{loc} = b \cdot \sqrt{2 \cdot p_0}$$
(17)

$$N_{exp} = 2\pi \rho \cdot p_{0E} \cdot p_{0I} \int_0^\infty r \cdot \exp\left(-\frac{r}{b_E}\right) \cdot \exp\left(-\frac{r}{b_I}\right) dr$$
(18)

$$N_{local} = 2\pi \rho \cdot p_{0E} \int_0^R r \cdot \exp\left(-\frac{r}{b_E}\right) dr$$
(19)

$$R_{loc} = \sqrt{2 \cdot p_{0I}} \cdot b_I$$
(20)

$$\frac{N_{local}}{N_{exp}} = \frac{b_E(b_E - \exp(-\frac{R_{loc}}{b_E}))(b_E + R_{loc})}{p_{0I}(\frac{b_E \cdot b_I}{b_E + b_I})}$$
(21)

(22)

Equation:21 calculates the factor by which "reciprocal motifs" are enhanced when using super-localized inhibitory neurons compared to the isotropic inhibition. ρ is the density of inhibitory neurons, p_{0E} and p_{0I} are the zero distance connection probabilities and b_E and b_I are the connection probability decay constants. Filling the equation with our values used for L4C results in a relative factor of 1.5, meaning that 1.5 times more reciprocal connections exist in the super-localized inhibition than in the exponential inhibition.

Even higher numbers of reciprocal connections require us to further localize inhibitory connections and we may do that by introducing multapses. If a neuron has more than one connection to another neuron, we call it a multapse. Technically we just need to reduce the radius of the super-localization even more but connect from I to E multiple times to keep the total number of synapses constant. Equation:23 describes the modified super-localized radius introducing the new parameter $n \in \mathbb{N}$, where n represents the number of multapses each inhibitory neuron asserts on each excitatory neuron in its reach. A multapicity of 4 enhances the relative factor of "reciprocal connections" to 1.85 of circular connections.

$$R_{loc} = b \cdot \sqrt{\frac{2 \cdot p_0}{n}} \quad (23)$$

We may also introduce an ellipticity to the super-localized inhibitory neurons similarly to the exponential case. Super-localized inhibitory neurons achieve their polarization by asserting all connections in the area enclosed by the ellipsis parameterized by a long axis of $2 \cdot R_{loc} \cdot c$ and a short axis of $2 \cdot R_{loc} \cdot d$.

6.3.2 Network description

Kurth and Albers describe their full network in a standardized way (Nordlie et. al. [NGP09]) which we adopt to fit our model. Table:1 gives a brief overview on the neuron model and connectivity, the excitatory reversal potential was measured by Langmoen and Hablitz [LH81]. Meanwhile Table:2,3,4,5 summarizes the number of neurons and the number of synapses whose parameters are shown by Table:7. The connectivity parameters of Table:1 are determined in Table:6.

6.4 Network analysis

In the previous paragraphs we introduced all building blocks of the computational model, but how do we actually measure their effectiveness and their success? In order to answer this questions, we first introduce the input shown to our retina and then discuss several benchmark's to evaluate the network. Analysis tools concerning standard spike train operations such as the spike train binning, cv calculation and PSD evaluation are performed using elephant (Denker and Kern [DK23]).

6.4.1 Retina input

The orientation map is basically an edge detector, determining the angle of a moving bar, hence only edges in various forms may trigger our models features. Three different types of inputs are relevant to test the networks functioning (fig:14): the grating covers the whole visual area periodically with stripes representing the strongest possible geometrical input. Meanwhile the single line is a weaker input only covering a small area of the cortex but appears more frequently in nature. The dashed line with its discontinuous input is an even weaker input than the line. Its main purpose is to investigate the patchy connectivity. Since patchy connections are long-range we hope to construct a network that can elicit an iso-orientation domain not directly by the thalamus but by proxy through another iso-orientation domain of same orientation preference (sec:5).

6.4.2 Orientation map retrieve and tuning curves

When building our network the orientation map played a major role. Not only the thalamo cortical, but also the intra-areal connections in L4 are strongly influenced by it. Hence the most important measure of this thesis is the orientation map retrieve, which reconstructs the orientation map using each neurons preferred input angle response. The procedure is basically the same as in the orientation map creation (sec:4.3). When a neuron shows its maximal response to an input of certain angle, we assign the neuron this angle as preferred orientation. The preferred orientation for every neuron is calculated and color coded in a 2D spatial map creating a retrieved orientation map. Subsequently we compare the original orientation map to the retrieved one by determining the number of correct retrieved neuron orientations. Furthermore we split the retrieved orientation map in layers and efficacy's such that six retrieved orientation maps emerge.

We describe the workflow more precisely. First retina model is given a black screen for 1s of biological time, such that a resting state can establish. Then we show the 0° drifting input for 2s. Now we repeat and show the retina model again a 1s second long black screen after which the 30° input appears for 2s. This process is carried on until all grating angles were converted by the retina model. The total time accounts for 1s of pre-simulation time and 6×2 s of input with 6×1 s subsequent black screen adding up to 19s of biological time. Comparing a neurons response (number of spikes) during each drifting grating orientation reveals its preferred orientation.

The orientation map is only able to check, whether or not a neurons orientation was correctly

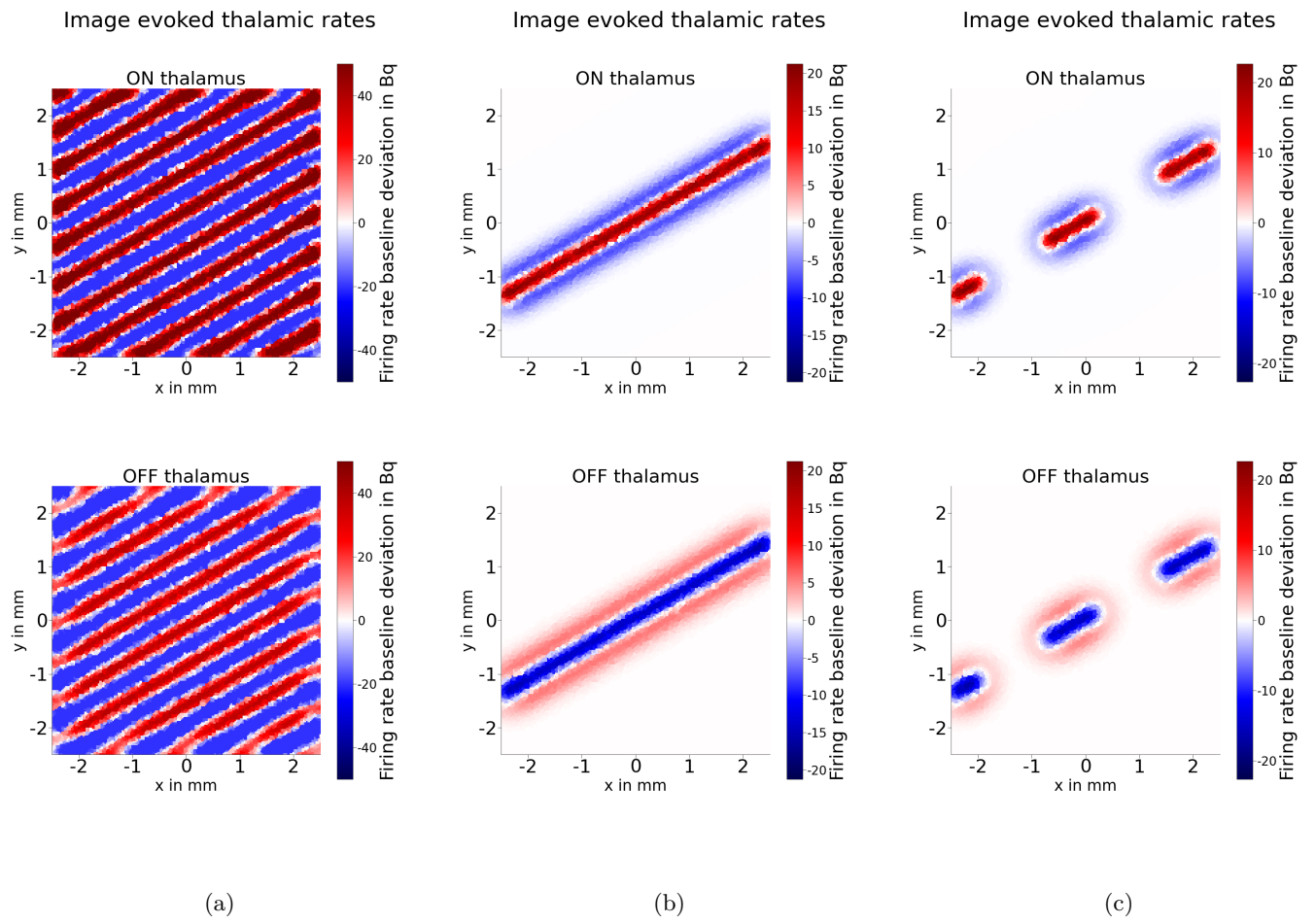


Figure 14: Inputs fed into the network. a) Grating, b) Line, c) Dashed line. These pictures depict the filter part of equation:12, the base rate accounts for 20 Hz. Since negative rates do not make any sense there are no firing rates below -20 Hz in the baseline deviation.

recovered. However, it does not contain any information about how prominent or scarce the activity at the preferred orientation surpassed its competitors. Tuning curves on the other hand provide us with that information by displaying a neurons activity dependent on the grating angle. Since each tuning curve is only capable of presenting one neuron, we need to average above populations. Box plots provide a convenient way to do so. We furthermore introduce the orientation prominence defined as:

$$prominence = \frac{\nu_{\Delta\theta=0^\circ} - \nu_{\Delta\theta=90^\circ}}{\nu_{\Delta\theta=0^\circ} - 0} \quad (24)$$

Equation:24 determines the difference between the preferred response $\nu_{\Delta\theta=0^\circ}$ and the most unpreferred response $\nu_{\Delta\theta=90^\circ}$. This difference is then normalized to the preferred rate. All values lie between 1 to $-\infty$ where 1 represents maximal tuning, 0 is no tuning at all and negative values indicate an anti tuned network.

6.4.3 Calculation of the g factor and PSP for conductance based neurons

Current based neurons receive a constant increase in their membrane potential indifferent of their internal state. We may calculate the PSP elicited by each excitatory input with $PSP_e = 2 \cdot \frac{e \cdot \tau_{syn}}{C}$ with 2 being the synapse weight, C the capacity of the target neuron and τ_{syn} resembling the synapse time constant. For the inhibitory input computational neuroscience uses the g factor (Brunel [AB97]) enhancing the inhibitory strength compared to the excitatory one to $PSP_i = g \cdot PSP_e$.

For conductance based neurons on the other hand this concept is highly non trivial. The charge influx (which is proportional to the potential influx) is modulated by the conductance and the membrane potential, which both depend on time. This equation gets non analytically solvable when accounting for the leak term which also depends on the membrane potential. Therefore we apply some approximations to determine parameters comparable to the current based model. Utilizing equation:1 we first take care of the leak term. Its time constant is about 31 ms, while that of excitatory and inhibitory synapses is 2 ms and 5 ms. In a rough approximation the leak time constant is much larger than the synapse ones. Therefore the leak term may be assumed to be zero during the charge influx of a single spike. We notice that at the equilibrium $|U_i - U_l| = 5$ mV and $|U_e - U_l| = 65$ mV, while the synapses elicit a PSP of around 0.8 mV in the inhibitory and of around 1.8 mV in the excitatory case. Therefore the single spike potential gain is much smaller than the potential difference $U_i - U_{reversal}$ (at higher membrane potentials the ratio becomes smaller for inhibitory neurons). Hence the change in $U_i - U_{reversal}$ during the spike is negligible and we can keep U_i constant. Applying this two crude approximations the PSP response may be calculated as:

$$\Delta V(t_0) = \int_{t_0}^{\infty} \frac{t}{\tau} \exp\left(1 - \frac{t}{\tau}\right) H(t - t_0) \frac{B}{C} \cdot (U(t_0) - U_{reversal}) dt = \tau \cdot e \frac{B}{C} \cdot (U(t_0) - U_{reversal}) \quad (25)$$

Equation:25 has only the one free parameter $U(t_0)$ resembling the membrane potential at the charge influx onset. The formula of current based neurons is defined by $\tau \cdot e \frac{A}{C}$ (Kuhn et. al. [KAR04]). Note that A is a current (1 μ A) while B is a conductance (1 nS). As the conductance based evoked PSP is dependent on the membrane potential also the g factor is. Therefore we calculate an average g factor. Calculating the mean of the evoked IPSP divided by the evoked EPSP provides us with the average g factor which we may compare with the current based g factor.

6.4.4 Raster plots of spiking activity

To display the spiking activity of the model neurons we employ the standard representation via raster plots. It shows the neuron ids on the vertical and the time on the horizontal axis with dots indicating the times, where a neuron spiked. Experimental setups usually employ around 100 neurons located in a small vicinity. The simulation on the other hand posses the spiking data of all 1.4 million neurons of the whole 25 mm² area. A raster plot of that size is neither spatially sortable nor interpretable in the usual sense. For this reason we only show every 800th neuron and sort by preferred orientation as determined by the artificial orientation map. Therefore we can only infer superficial network properties from this kind of plot, such as orientation tuning and large scale correlations. The bin size is 0.1 ms just like the simulation resolution and the activity is

registered for 19 s of biological time, which is much larger than ordinary experimental measurement times.

6.4.5 Firing rate histogram's

The most basic neural activity measure is the firing rate representing the numbers of spikes per time. When representing the firing rate, one may average it over all neurons or display it in a firing rate histogram. The overall average gives a quick check, if the network shows realistic activity at all. Firing rate distributions on the other hand are a more complex measure resolving the overall firing rate behaviour of the neurons more precise. First we determine the average firing rate of each spike train. Subsequently they are condensed into a histogram split into 15 bins between the minimal and maximal firing rate value.

6.4.6 Coefficient of variation

The coefficient of variation is defined by $\frac{\sigma}{\mu}$, where μ is the average time between two spikes and σ its standard deviation. The cv measures the regularity of a spike train, a cv of 0 indicates a perfect regularity in spiking activity, while higher cvs correspond to strongly irregular spiking. Neurons in experimental data show most often a cv between 0.8 and 1.2 (Softky et. al. [SK93]), for comparison, a poisson process has a cv of 1. We calculate the cv of single neurons and display them in a frequency plot.

6.4.7 Power spectra

From the time spike plot we may calculate two types of power spectra. First the power of the population average and second the average of the power of single neurons. The first tells us something about oscillations of the whole population while the latter provides us with information about single neurons. Additionally the power spectra are individually evaluated for the driven and resting network state. Therefore $2 \times 2 = 4$ power spectra for each simulation are calculated. We use the Welch PSD function of the elephant library [DK23], which is a smoothed version of the classical power spectrum. For the parameters a frequency resolution of 1000 Hz (is equal to bin size of 1 ms) an overlap of 0.5 and six segments are chosen.

6.4.8 Spatial activity

While the raster plot is an appropriate tool to visualize activity in the time domain and simple population features, it has shortcomings in representing spatial patterns. Therefore we create a heat-map showing the spatially resolved activity integrated over a certain time frame. Each time frame aggregates 10 ms of spike activity of each 10th neuron interpolated onto a 200×200 grid. Furthermore we show the thalamic ON and OFF firing rates at the current point in time below. In the very bottom we depict the raster plot with a black bar indicating the currently aggregated area.

6.4.9 Contrast in-variance

Contrast in-variance refers to the brains ability to perceive drifting gratings independent of their contrast. The tuning curves in a contrast invariant network differ in height, but not in their shape, when presented drifting gratings of different contrast (Skottun et. al. [SBS⁺87a]). For visualization we plot the tuning curves of orientation map retrieves with drifting gratings of different contrast together. Then each tuning curve is normalized to its maximal firing rate value to extract the shape.

6.4.10 Signal to noise ratio

The signal to noise ratio is defined as:

$$\frac{s}{n} = \frac{E[s^2]}{\sigma^2} \quad (26)$$

We want to apply it on noisy thalamic inputs to determine how strong the added noise is compared to the underlying signal. Given an arbitrary noise influenced picture we know all the thalamic rates,

since the noise is already added we write $v_{lgn} = s + \sigma$ and because noise and signal are uncorrelated it follows that $E[s^2] = v_{lgn}^2 - \sigma^2$. Plucking this into equation:26 results in equation:27

$$\frac{s}{n} = \frac{E[v_{lgn}^2]}{\sigma^2} - 1 \quad (27)$$

The expected value of the thalamic firing rate is $E[v_{lgn}^2] = \frac{\sum_i v_{lgn}^2}{N_{lgn}}$, for σ it is known that the noise is equally distributed in a certain interval bin which results in $\sigma = \frac{bin}{\sqrt{12}}$. Finally we might calculate the signal to noise ratio as in equation:28

$$\frac{s}{n} = \frac{\sum_i v_{lgn}^2}{N_{lgn}} \cdot \frac{\sqrt{12}}{bin} - 1 \quad (28)$$

Table 1: General description of model of layer 4 in macaque primary visual cortex

Neuron and synapse model	
Subthreshold dynamics	$C \frac{dV}{dt} + [V - E_L]G_l + [V - E_e]G_e(t) + [V - E_i]G_i(t) = 0,$ $G_j(t) = \sum_k B_j \frac{t}{\tau_j} e^{1-t/\tau_j} H(t),$ $j \in e, i$ $G_j(t)$ are the synaptic conductance's U_j are the reversal potentials $(U_i = 0\text{mV}, U_e = -70\text{mV})$ here H denotes the Heaviside function. B_j are the peak conductance's
Spiking	If $V(t-) < V_{\text{th}}$ and $V(t+) \geq V_{\text{th}}$, 1. Set $V(t) = V_{\text{reset}}$ in $(t, t + \tau_r]$ 2. Emit spike with time stamp t .
Delays	
Delay	Synaptic delay is $d_0 + r \cdot v_c + \mathcal{N}(0, \sigma_d)$ where r is the Euclidean distance between pre- and post-synaptic neurons.
Stimulation	
External input	Independent Poisson spike trains with fixed rate displayed in Table:12 and population-specific in-degrees shown in Table:2.
Connectivity	
Isotropic connections	Establish connection with probability $P_{AB}^{0,\text{iso}} e^{-\frac{r}{\lambda_{AB}}}$ where B is the pre-, A the post-synaptic population, v of A resides, B has X synapses, and r the Euclidean distance between neurons that are to be connected.
Patchy connections	Connect neurons with identical orientation preference with pair-wise Bernoulli connectivity with connection probability P_{AB}^{patchy} where B denotes the and A the post-synaptic population in an ellipse with axis parameters summarized in Table:11.
Push-pull connections	Connect neurons with identical orientation preference with spatially dependent connection probability
Super-localized inhibitory neurons	Super short inhibitory connections $P_{AB} = 1$ if the distance between source and target is smaller than $r_{loc} = \lambda_{AB} \sqrt{2P_{0AB}}$ where B is the inhibitory pre- A the excitatory post-synaptic population, λ_{AB} is the isotropic connectivity decay factor and P_{0AB} is the zero distance connection probability 20% of the neurons in L4AB and 50% of the neurons in L4C are super-localized
Elliptical inhibition	Elliptically projecting inhibitory neurons $P_{AB}^{0,\text{elliptical}} P_{0AB} \cdot$ $\exp\left(\sqrt{\left(\frac{\Delta x \cdot \cos(\phi) + \Delta y \cdot \sin(\phi)}{c \cdot \lambda_{AB}}\right)^2 + \left(\frac{\Delta x \cdot \sin(\phi) - \Delta y \cdot \cos(\phi)}{d \cdot \lambda_{AB}}\right)^2}\right)$ Where the parameters as the are used, ϕ describes the ellipses angle, c the ellipses long axis, and d the ellipses short axis

Table 2: Network size under a $5 \text{ mm} \times 5 \text{ mm}$ patch of cortex

Network size		
Layer	Number of excitatory neurons	Number of inhibitory neurons
4A/B	571 779	147 544
4C	675 646	128 704

Table 3: Single neuron in degrees under a $5 \text{ mm} \times 5 \text{ mm}$ patch of cortex

Inter-areal single-neuron in degrees				
Layer	4A/BE	4A/BE	4CE	4CI
4A/BE	201	93	591	103
4A/BI	113	61	347	68
4CE	66	27	460	130
4CI	42	23	363	117

Table 4: External V1 in degrees under a $5 \text{ mm} \times 5 \text{ mm}$ patch of cortex

External V1 in degrees								
Layer	2/3E	2/3I	3BE	3BI	5E	5I	6E	6I
4A/BE	56	36	34	39	174	32	300	64
4A/BI	30	22	15	24	94	20	175	42
4CE	17	9	14	19	95	16	307	54
4CI	8	6	4	15	63	13	242	49

Table 5: In degrees from thalamus under a $5 \text{ mm} \times 5 \text{ mm}$ patch of cortex

Thalamic single-neuron in degrees		
Layer	Indegree of excitatory neurons	Indegree of inhibitory neurons
4A/B	51	30
4C	238	187

Table 6: Parameters for the network connectivity

Connectivity		
P_{AB}^0	Table 10	Peak connection probabilities
ψ	0.4	Patchiness parameter
ξ	0.35	Relative frequency of push-pull connections
λ_{vX}	Table 8, Table 9	Characteristic lengths of isotropic connectivity
a, b	Table 11	Size of ellipses parametrized by lenght of semi-major and semi-minor axis

Table 7: Neuron, synapse and delay parameters for network simulation

Neuron parameters		
$\tau_{m,E}$	31 ms	Excitatory membrane time constant
$\tau_{m,I}$	10 ms	Inhibitory time constant
τ_r	2 ms	Absolute refractory period
$\tau_{syn,E}$	2.0 ms	Excitatory synapse time constant
$\tau_{syn,I}$	5.0 ms	Inhibitory synapse time constant
$C_{m,E}$	245 pF	Excitatory membrane capacity
$C_{m,I}$	103 pF	Inhibitory membrane capacity
E_L	-70 mV	Reversal potential
V_{reset}	-69 mV	Reset membrane potential
V_{th}	-40 mV	Threshold
Synapse parameters		
J_{XE}	1.0 nS	Synaptic weight excitatory neurons
g_{mean}	2.0	Average relative inhibitory synaptic efficacy
J_{XI}	$-g \cdot J_{XE}$	Synaptic weight inhibitory neurons
Delay parameters		
d_0	0.5 ms	Delay offset
v_c	0.3 mm/ms	Conduction speed
σ_d	0.05 ms	Temporal jitter of delay distribution
Stimulation		
ν_0	$0 \frac{\text{spikes}}{\text{s}}$	Baseline rate

λ_{vB} [mm]		Target Layer		Source Layer	
		L4AB	L4C	L4AB	L4C
L4AB		0.261	0.215		
L4C		0.121	0.141		

Table 8: Estimated characteristic lengths for projections from excitatory neurons to the different cortical layers. Numeric values are derived from experiments by Sincich et. al. [SB01] and - for lack of data - refined by qualitative inspections of the tracing studies by Fitzpatrick et. al. [FLB85].

λ_{vB} [mm]		Target Layer		Source Layer	
		L4AB	L4C	L4AB	L4C
L4AB		0.062	0.062		
L4C		0.062	0.062		

Table 9: Estimated characteristic lengths for projections from inhibitory neurons to the different cortical layers. Numeric values are derived from estimates based on Kritzer et. al. [KCS92] combined with data from Packer et. al. [PY11].

Population	Peak connection probability P_{AB}^0			
	4A/BE	4A/BI	4CE	4CI
4A/BE	0.043	0.099	0.055	0.124
4A/BI	0.008	0.293	0.031	0.395
4CE	0.027	0.139	0.103	0.819
4CI	0.017	0.119	0.081	0.738

Table 10: Peak connection probabilities for our model of macaque primary visual cortex. Target populations are given in rows, source populations in columns.

Semi-minor and major axes [mm]		
Source Layer	Semi-minor axis	Semi-major axis
L4ABE	2.2	3.3

Table 11: Semi-minor and major axes describing ellipses for patchy connectivity. Semi-minor and major axes describing an ellipse centered at a source neuron confining the region in which patchy connections to neurons with the same preferred orientation can be established. Data from Angelucci et. al. [ALW⁺02].

Mean V1 external rates [Hz]							
L23AE	L23AI	L3BE	L3BI	L5E	L5I	L6E	L6I
0.943	3.026	0.943	3.026	7.733	8.664	1.094	7.851

Table 12: Average firing rates in the external V1 layers

7 Results

In the previous section we introduced multiple alterations to L4C and L4AB of the network constructed by Kurth and Albers. The enhancements are consecutively applied to the base network finally arriving at the fully improved network.

7.1 Isotropic connectivity orientation map retrieve

At first we retrieve the orientation map using the model without intra-areal connections to verify that the input routine works properly. To achieve that we just set the weights of all connections from L4 to L4 equal to zero and provide no external V1 input.

Figure:15 depicts the retrieved orientation map, most orientations are predicted correctly in the excitatory layers of L4C (fig:16). Therefore the thalamo-cortical connectivity combined with the retina model works as intended. Nevertheless, the orientation tuning does not show a very prominent peak. In the inhibitory layers the orientation map retrieve does not work since there are no connections targeting them. L4AB receives weak and unstructured input resulting in neurons showing some activity.

Subsequently we try to retrieve the orientation map with the isotropic connections being activated (sec:4.1). The weight modulation is not considered for yet. Drifting gratings (fig:14a) drive the network.

The retrieved orientation map (fig:17) is very different to the artificial orientation map fed into the network (fig:6b). In the excitatory layers some sparse structure is observable, while the inhibitory layers just show noise. Since the retrieve worked using a network without weights, the isotropic connections must hinder the orientation map from being retrieved. We observe a "spill over excitation" from the preferred neurons to the non preferred ones. The average firing rate accounts to 52 Hz in L4AB. However, increasing the average g factor and in consequence lowering the activity produces fewer retrieved orientations (not shown here).

7.2 Hebbian inspired weight modulation enables orientation map retrieve

The isotropic connectivity prohibited due to the "spill over excitation" the orientation map from being retrieved. We therefore lower the excitatory weights between neurons of different preferred orientation such that less activity between them is transmitted. Furthermore the inhibitory weights are modulated less such that neurons of different preference can suppress each other. Excitatory and inhibitory modulation are qualitatively consistent with the experimental findings of Znamensky et al. [ZKM⁺24]. The Hebbian inspired weight modulation is implemented as visualized in Figure:18. Again, we try to retrieve the orientation map from the neural activity after stimulating the network with moving gratings.

Evaluating Figure:19 we find that the three layers perform differently well in retrieving the orientation map, L4A/B performs the worst and L4CE_ON the best with 48% (fig:20). Furthermore the orientation map is visible in the inhibitory populations of L4C although less prominent as in their excitatory counterpart. Tuning curves show a rather low tuning prominence of 10%. Due to less excitation in the network the average firing rate decreases compared to the non weight modulated case to 22 Hz.

7.3 Super-localized inhibition increases number of correct retrieved orientations and tuning steepness

In order to reduce the firing rate as predicted by sec:6.3.1, 50% of the inhibitory neurons in L4C are changed to project in a super-localized manner . In L4AB we only modify 20% of the neurons. The reason for different percentages are the push-pull and patchy connectivity introduced in a later stage to the network (see sec:7.6,7.5). We furthermore expand the weight modulation of Figure:18 to account for super-localized inhibitory neurons as shown in Figure:21.

Once again we retrieve the orientation map consulting the drifting grating input. The tuning prominence increases to 21% in all excitatory layers of L4. Furthermore the number of correctly retrieved orientations increases slightly in L4C and strongly in L4AB (fig:23, 22). The firing rate

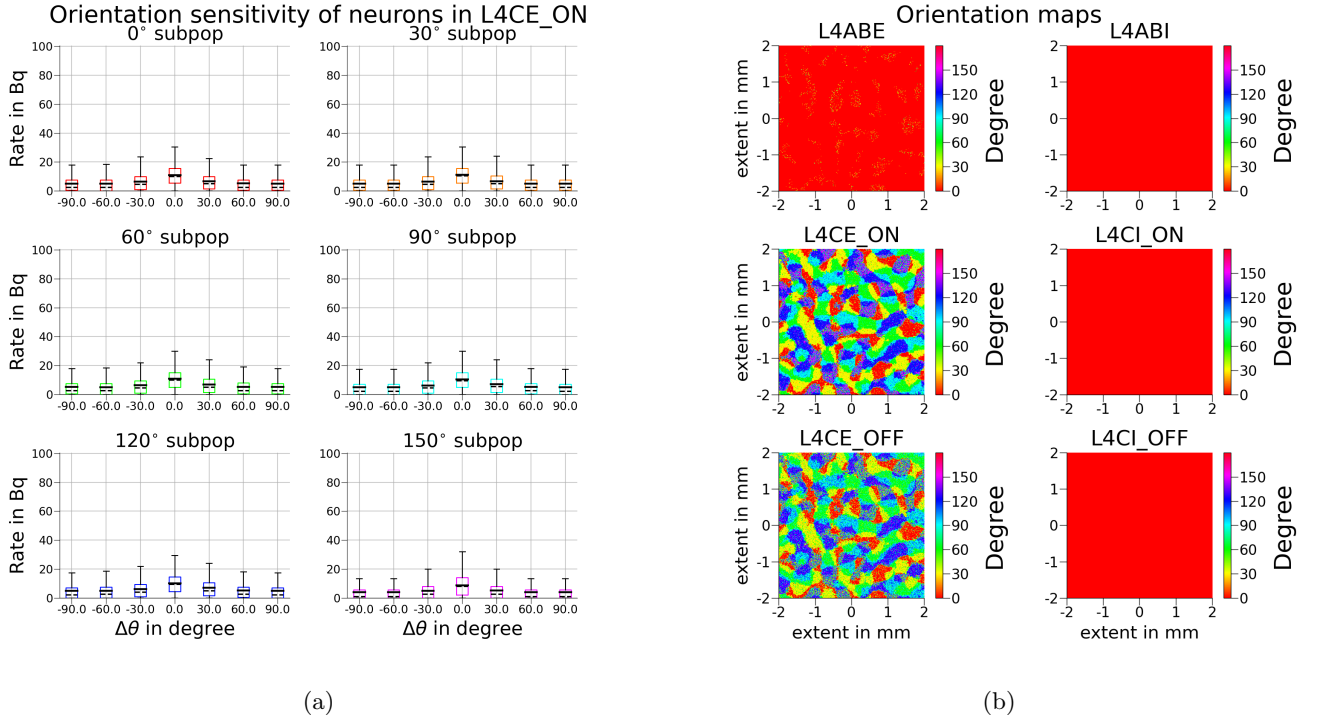


Figure 15: a) Tuning curves for the sub populations in L4CEON showing the response of the population over the difference between preferred orientation and showed grating orientation. The dashed line indicates the median while the solid one represents the average. b) retrieved orientation map, note that the inhibitory layers and L4ABE do not show any orientation tuning since the thalamus does not project to them. About 89% in L4CEON and 76% in L4CEOFF of the orientations are predicted correct when the recurrent connectivity is removed.

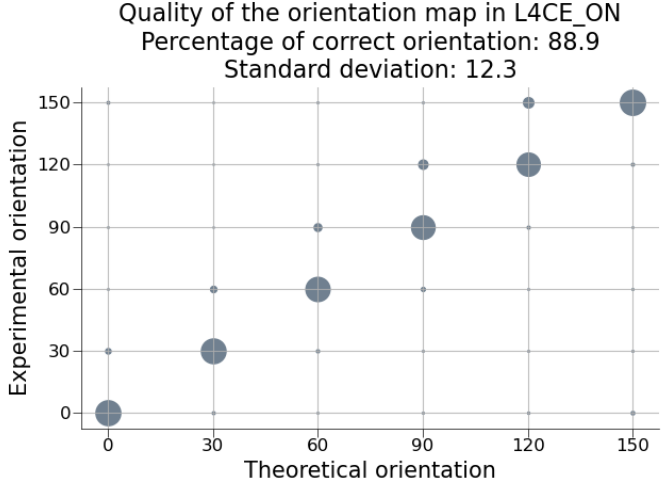


Figure 16: The horizontal axis represents the assigned preferred orientations, while the vertical axis shows the recorded preferred orientation. The dot size is proportional to the fraction of neurons showing maximal response in this category. For example a large dot at $x = 0^\circ$ and $y = 30^\circ$ indicates that neurons assigned the 0° preference react strongly to a 30° grating. Furthermore the fraction of total correct predicted orientations is shown.

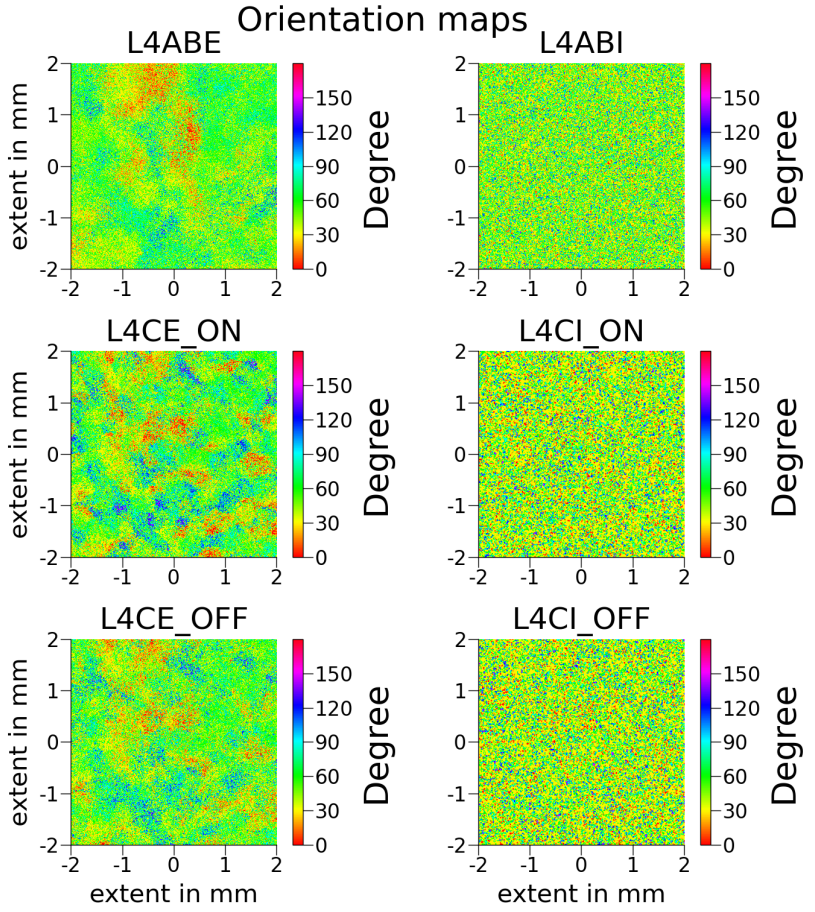


Figure 17: Retrieved orientation map of a network possessing only the iso-connectivity in the cortex. The retina is shown the 6 different moving gratings, then every neuron is assigned the grating orientation it send the most spikes to. The iso-connectivity is not sufficient to retrieve the orientation map.

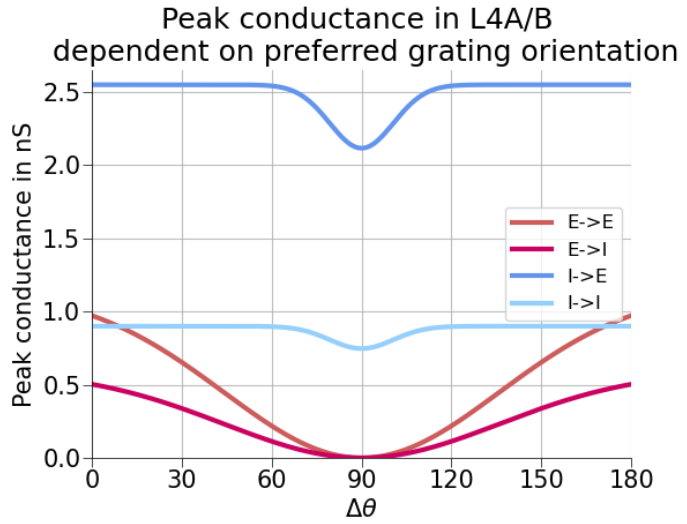
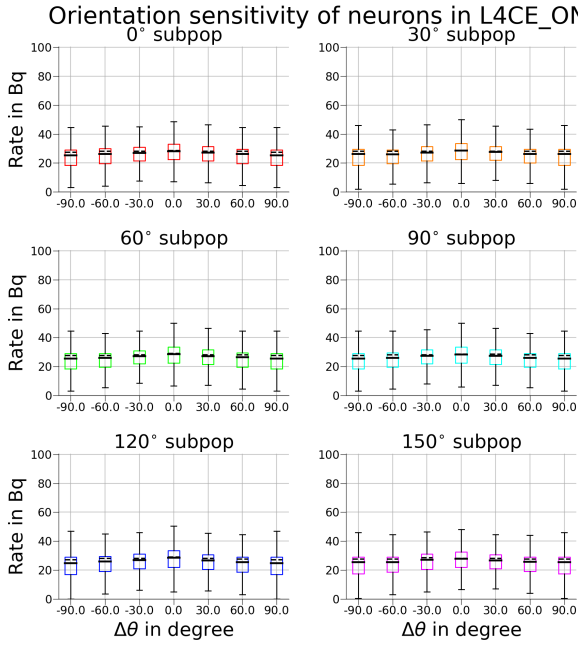
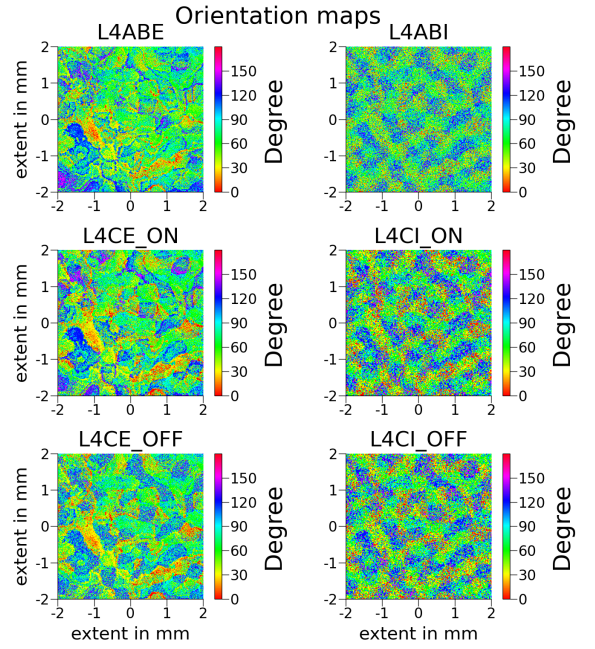


Figure 18: Visualization of the weight modulation used for the peak conductance B (see eq:1,1) in L4AB. The modulation in L4C is similar but has a 5% stronger excitation.



(a)



(b)

Figure 19: Model employing the Hebbian inspired weight modulation. a) Tuning curves resolved by preferred orientation in L4ABE. They show the response of the population over the difference between preferred orientation and the showed grating orientation. The dashed line indicates the median while the solid one represents the average. b) Retrieved orientation map utilizing the weight modulation as described in figure:18. The percentage of correct retrieved orientations is 48% in L4CE-ON, 44% in L4CE-OFF and 31% in L4ABE (baseline of 17%).

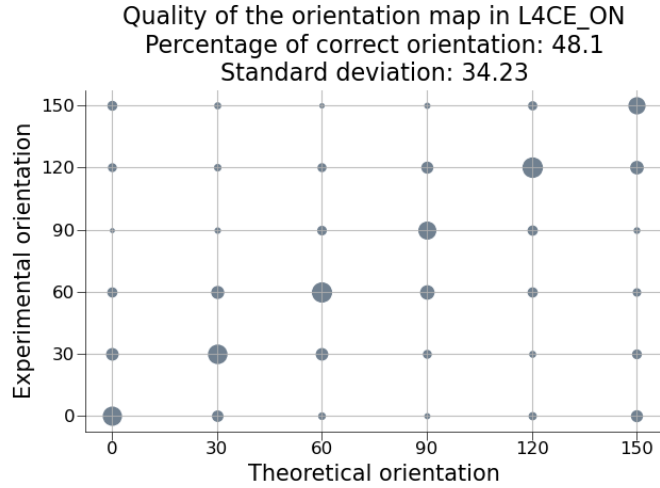


Figure 20: Model employing the Hebbian inspired weight modulation. The horizontal axis represents the assigned preferred orientations, while the vertical axis shows the recorded preferred orientation. The dot size is proportional to the fraction of neurons showing maximal response in this category. For example a large dot at $x = 0^\circ$ and $y = 30^\circ$ indicates that neurons assigned the 0° preference react strongly to a 30° grating. Furthermore the fraction of total correct predicted orientations is shown.

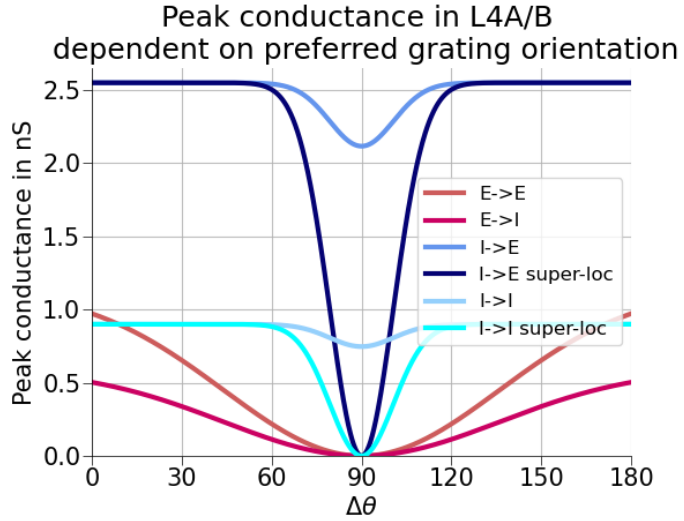


Figure 21: Visualization of the weight modulation used for the peak conductance B (see eq:1,1) in L4AB. The modulation in L4C is similar but has a 5% stronger excitation. This is an extension of Figure:18 including super localized inhibitory neurons.

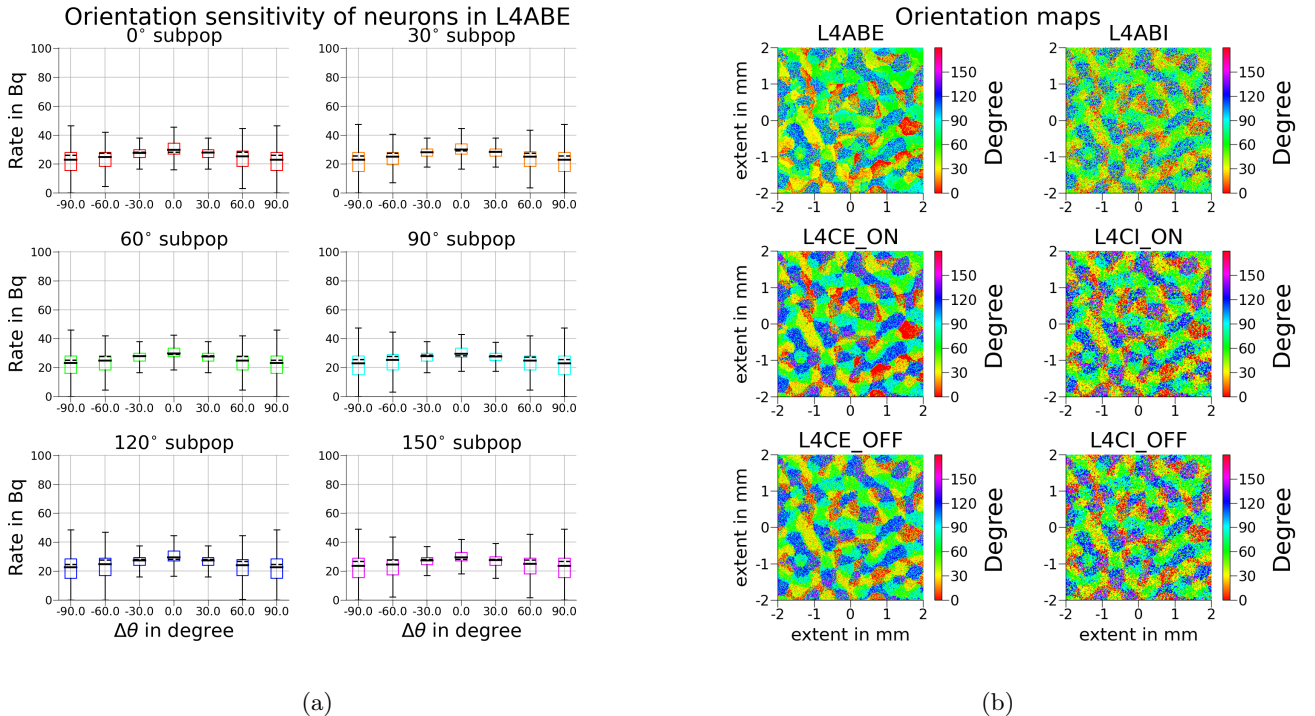


Figure 22: Model with added super-localized inhibition. a) Tuning curves resolved by preferred orientation in L4ABE. They show the response of the population over the difference between preferred orientation and the showed grating orientation. The dashed line indicates the median while the solid one represents the average. b) Retrieved orientation map using super localized inhibitory neurons.

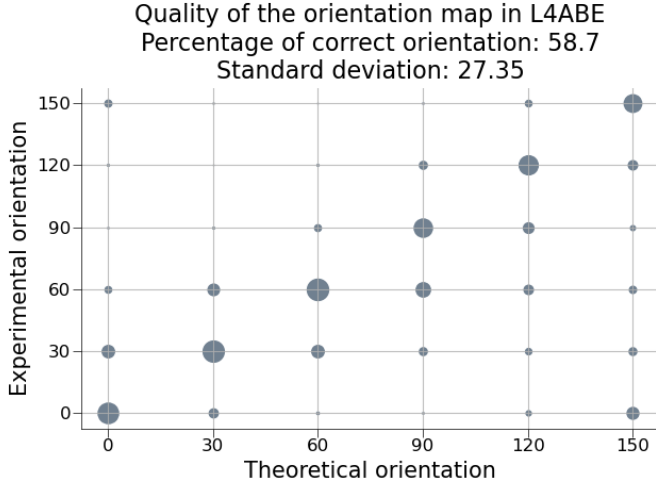


Figure 23: Model with added super-localized inhibition. The horizontal axis represents the assigned preferred orientations, while the vertical axis shows the recorded preferred orientation. The dot size is proportional to the fraction of neurons showing maximal response in this category. For example a large dot at $x = 0^\circ$ and $y = 30^\circ$ indicates that neurons assigned the 0° preference react strongly to a 30° grating. Furthermore the fraction of total correct predicted orientations is shown. L4C retrieves about 69% of the neurons orientation preference correct.

however is barely lowered to 21 Hz. Super-localizing some inhibitory neurons therefore displays an un-predicted effect.

7.3.1 Reciprocal motifs do not enhance excitation-inhibition balancing

Since the super-localization of the inhibitory neurons only shows a slight decrease of the average firing rate from 22 Hz to 21 Hz we want to test whether further increase of reciprocal connections changes the situation. Section:6.3.1 describes the enhanced number of reciprocal connections utilizing equation:23 putting forward the hypothesis of increased balancing following the argumentation of Peng et. al. [PTP⁺21]. They argue that reciprocal connections could maintain the balance between excitation and inhibition. However, introducing super-localized inhibitory neurons does only show a slight decrease of the average firing rate from 22 Hz to 21 Hz (sec:7.3). Hence we test whether further localization and therefore enhanced the number of reciprocal connections does change the situation. We simulate the network with multipicities of $m \in 1, 2, 3, 4$. The result is an insignificant change in the firing rates and orientation tuning, barely any effect is noticeable. We therefore do revert the multiplicity and proceed with the network of Section:6.3.1.

7.4 Elliptical inhibition steepens tuning curves and rises correct predicted orientations in L4AB

The initial motivation for including elliptical inhibition stems from Peng et. al. [PTP⁺21]. They measure elliptically projecting inhibitory neurons located in the presubiculum of rat, which is computationally very similar to macaque V1 (see also sec:6.3). Additionally they showed an increased orientation tuning when changing from a circular to an elliptical projection.

We can further argue that elliptical inhibition works fine combined with the weight modulation. Because elliptical inhibitory neurons on average assert connections on a larger distance than circular ones do (fig:24). Therefore they target more excitatory neurons preferring different orientations than themselves. This is further enhanced by us putting forward that inhibitory neurons are modulated less than excitatory ones (sec:7.2). In consequence inhibition suppresses neurons of different preferred orientation stronger than the excitatory neurons can elicit them. An ellipses long axis of 3.5 is chosen for all non super-localized inhibitory neurons. Then the orientation map is retrieved feeding drifting gratings into the network.

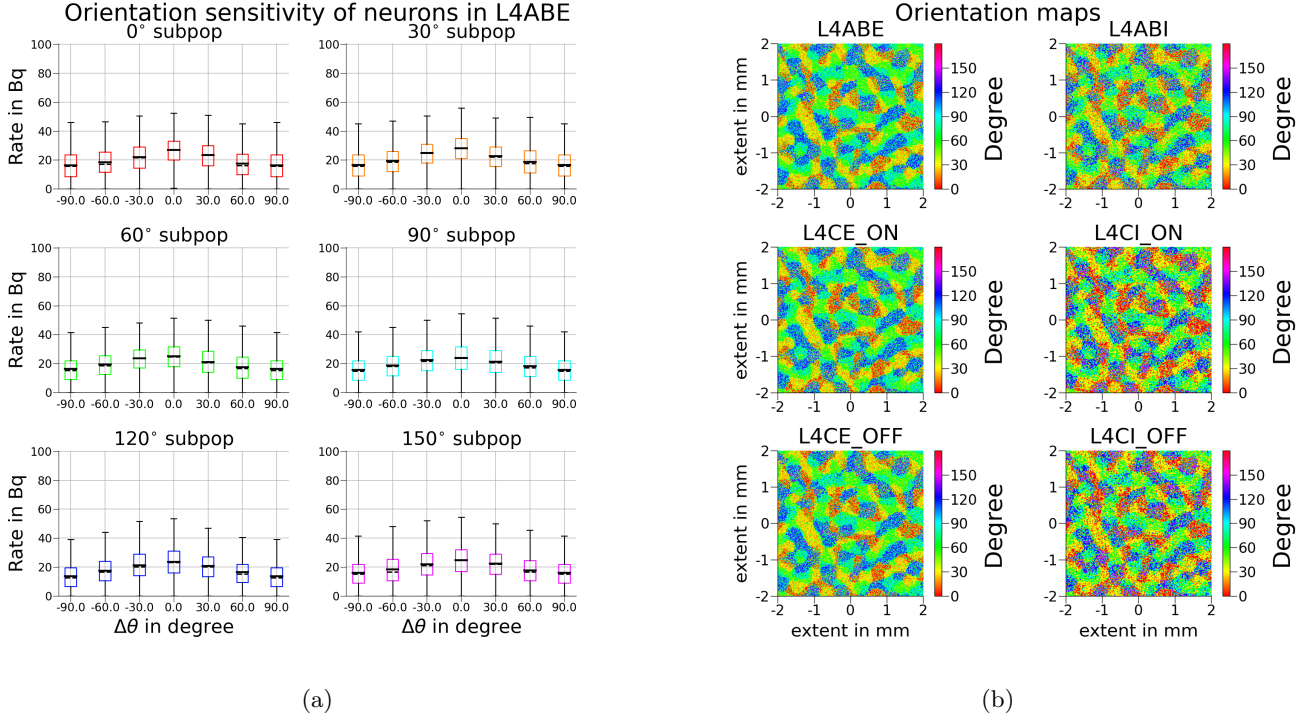


Figure 24: Network with added elliptical projecting inhibition. a) Tuning curves for the different orientation preferring populations in L4ABE. The response of the population dependent on the difference between preferred orientation and grating orientation is shown. The dashed line indicates the median while the solid one represents the average. b) Retrieved orientation map using elliptical inhibition with a long axis of 3.5. The tuning prominence accounts for 38%.

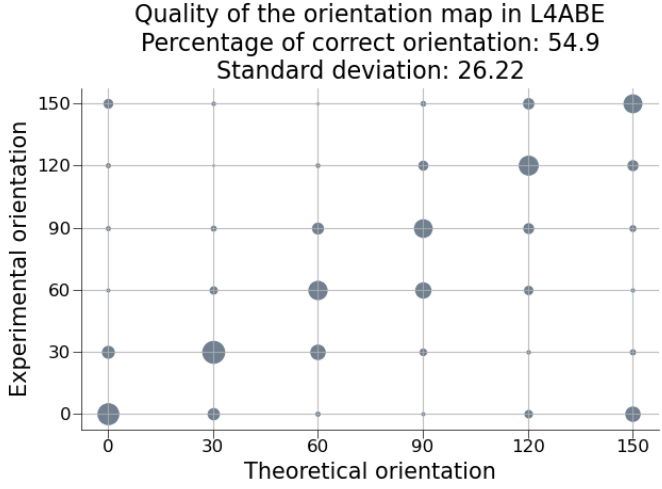


Figure 25: Network with added elliptical projecting inhibition. The horizontal axis represents the assigned preferred orientations, while the vertical axis shows the recorded preferred orientation. The dot size is proportional to the fraction of neurons showing maximal response in this category. For example a large dot at $x = 0^\circ$ and $y = 30^\circ$ indicates that neurons assigned the 0° preference react strongly to a 30° grating. Furthermore the fraction of total correct predicted orientations is shown.

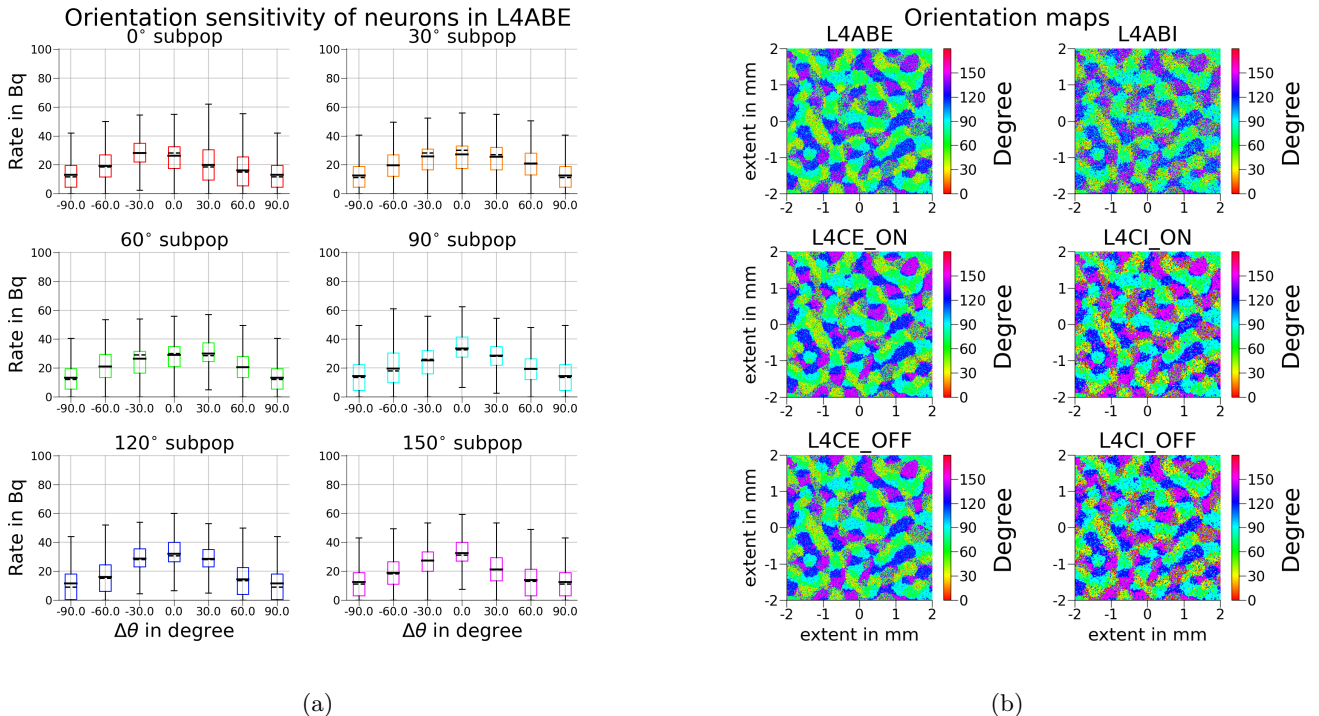


Figure 26: Network with added push-pull connectivity. a) Tuning curves of a network employing elliptical inhibition, super-localized inhibition, weight modulation and push-pull connectivity under stimulation of a moving grating. b) Retrieved orientation map with push-pull connectivity of $frac_{pp} = 35\%$ and weight factor of 1.07 incorporated into the network.

Adding elliptical inhibition steepens the tuning curve by elevating the tuning prominence from 20% to 38% (fig:24). Meanwhile the number of correct predicted orientations slightly decreases from 59% to 55% in L4ABE. Furthermore the average firing rate decreases from 22 Hz to 18 Hz.

7.5 Push-pull connectivity increases tuning prominence

In the following we include the push-pull connectivity from section:4.4 into L4C, accounting for the thalamo-cortical induced correlations. The push-pull connectivity enhances the number of intra-iso-orientation-domain connections. Simultaneously less connections between neurons of different preferred orientations exist. We therefore expect less "spill over" between iso-orientation domains of different preferred orientation. In consequence the tuning prominence and correct predicted orientations should increase.

An optimal orientation map retrieve with drifting gratings (fig:14a) occurs when the parameters are chosen such that $w_{pp} = 1.07 \cdot w_{high}$ and a fraction of push-pull connections of $frac_{pp} = 35\%$ is used. The firing rate and correct retrieved orientations stay the same with 18Hz and 55% (fig:27,26). The main effect is apparent in L4C, where the correct predicted number of orientations and the firing rate increase. This makes sense since the push-pull connectivity only is located at L4C. However, L4AB is more interesting than L4C, as it is the first non-input stage of cortical computation.

We may also test the case of push-pull connectivity without elliptical inhibition. Doing so reverses the average firing rate back to 22 Hz as in the super-localized network (sec:7.3). Furthermore the number of correct retrieved orientations in L4C_ON increases to 72%. Meanwhile the correct retrieved numbers in L4AB decreases to a value of 44% between that of the weight modulated network and the super-localized one. The tuning prominence decreases to 22%.

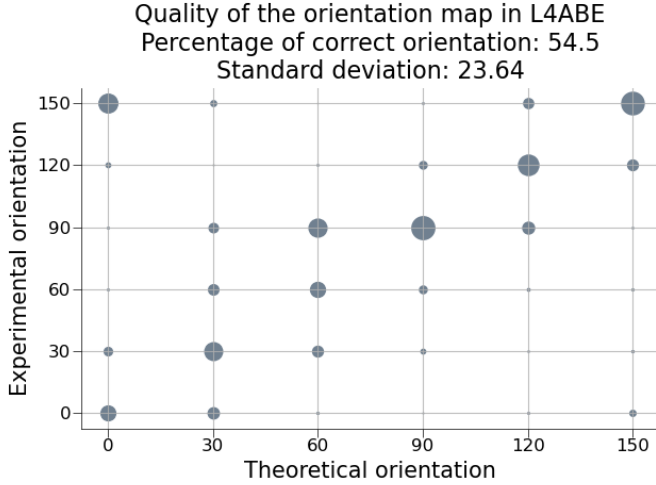


Figure 27: Network with added push-pull connectivity. The horizontal axis represents the assigned preferred orientations, while the vertical axis shows the recorded preferred orientation. The dot size is proportional to the fraction of neurons showing maximal response in this category. For example a large dot at $x = 0^\circ$ and $y = 30^\circ$ indicates that neurons assigned the 0° preference react strongly to a 30° grating. Furthermore the fraction of total correct predicted orientations is shown.

7.6 Patchy connectivity further increases correctly predicted orientations and tuning prominence in L4ABE

Similar to the push-pull connectivity the patchy connectivity increases intra-iso-orientation-domain connectivity. Therefore it should further increase the firing rate of the neurons of preferred orientation and steepen the orientation prominence. In addition to that also long range connections between iso-orientation domains of same preferred angle are enhanced. This should increase the stabilization these domains exert on each other. We find the most beneficial network state when choosing $frac_{patchy} = 40\%$ and $w_{patchy} = 1.07 \cdot w_{high}$.

Retrieving the orientation map with drifting gratings now provides for 81% of correct predicted orientations (fig:29, fig:28b) in L4A/B. This is a significant jump from the previously 55% retrieved orientations. This is the first network state where the number of correct predicted orientations is higher in L4AB than in L4C (see tab:13). Firing rate and tuning prominence increase in L4ABE to 20 Hz and 68%. Therefore this network state exhibits the highest number of correct retrieved orientations and the steepest tuning curves.

Figure:30 visualizes spike trains of neurons in the different layers. All neurons tend to fire at a similar time with a fixed frequency creating the vertical stripes. Preferred neurons have a three times higher firing rate than non preferred ones (fig:28a).

We want to test what happens if elliptical inhibition or push-pull connectivity or both is omitted while the patchy connectivity persists. Omitting both results in an firing rate increase to 22 Hz a tuning prominence of 30% and 70% correct retrieved orientations. Only omitting the push-pull connectivity keeps the average firing rate constant at 19 Hz, decreases the tuning prominence to 55% and even increases the correct predicted orientations to 88%. The last case only omits the elliptical inhibition (inhibition is circular again) and reaches an average firing rate of 23 Hz, a tuning prominence of 32% and a number of correct retrieved orientations of 51%.

7.7 Intermediate parameters

The network state of section:7.6 is able to retrieve a large fraction (81%) of the orientation correctly. In the following we want to summarize the enhancements in each step.

Table:13 shows the percentage of correctly retrieved orientations and the tuning prominence for the excitatory layers in each step of adding a feature to the network. The no intra-areal connectivity network initially performs the best in retrieving orientations in L4CEON and has already

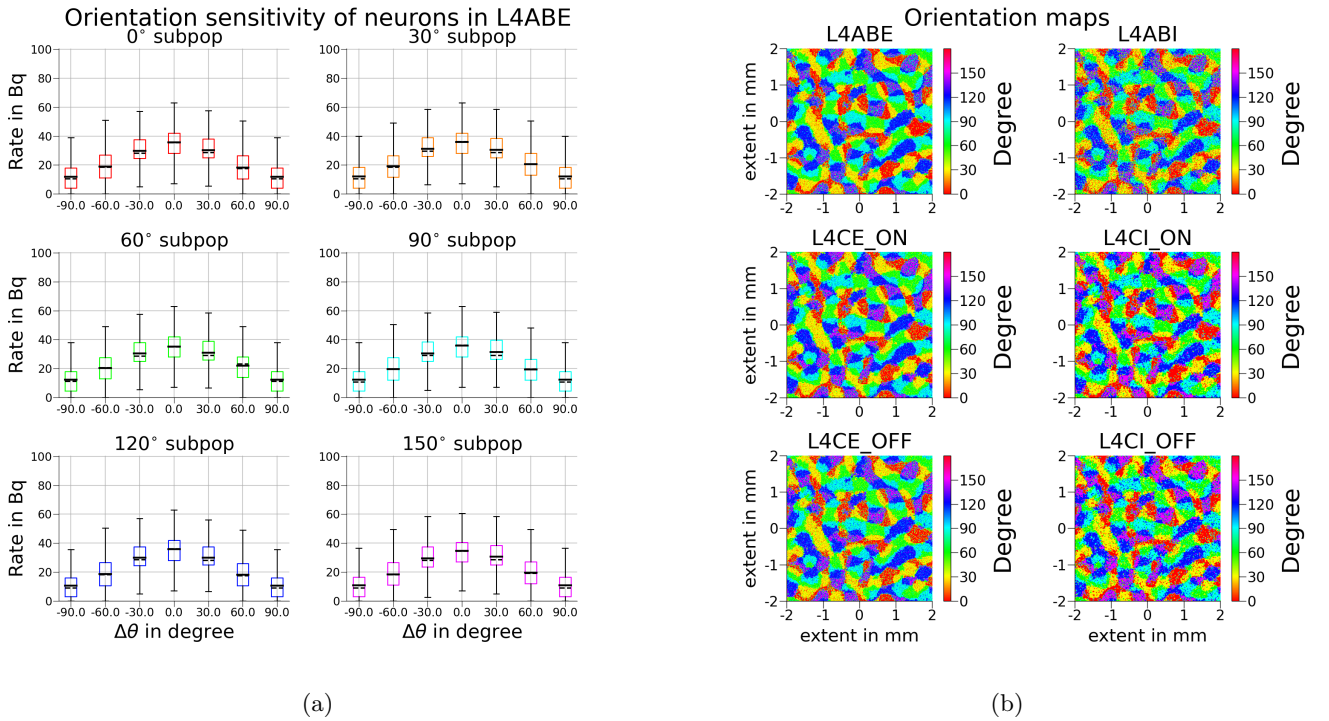


Figure 28: a) Tuning curves of a network employing elliptical inhibition, super-localized inhibition, weight modulation, push-pull connectivity and patchy connections under stimulation of a moving grating. b) Retrieved orientation map with patchy connectivity of $frac_{patchy} = 40\%$ and weight factor of 1.07 incorporated into the network.

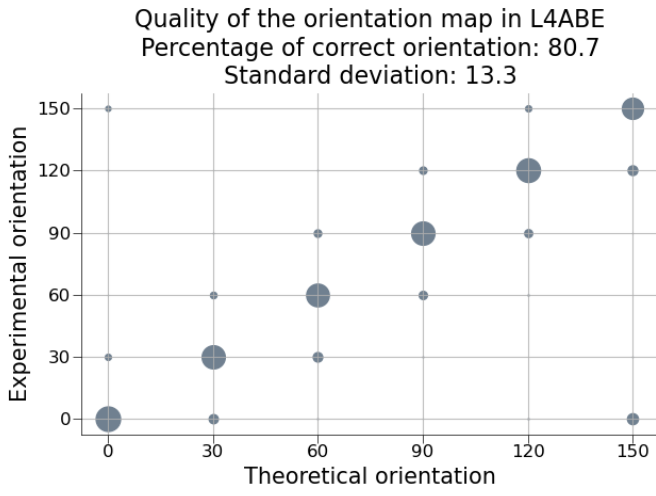


Figure 29: The horizontal axis represents the assigned preferred orientations, while the vertical axis shows the recorded preferred orientation. The dot size is proportional to the fraction of neurons showing maximal response in this category. For example a large dot at $x = 0^\circ$ and $y = 30^\circ$ indicates that neurons assigned the 0° preference react strongly to a 30° grating. Furthermore the fraction of total correct predicted orientations is shown.

Raster plot

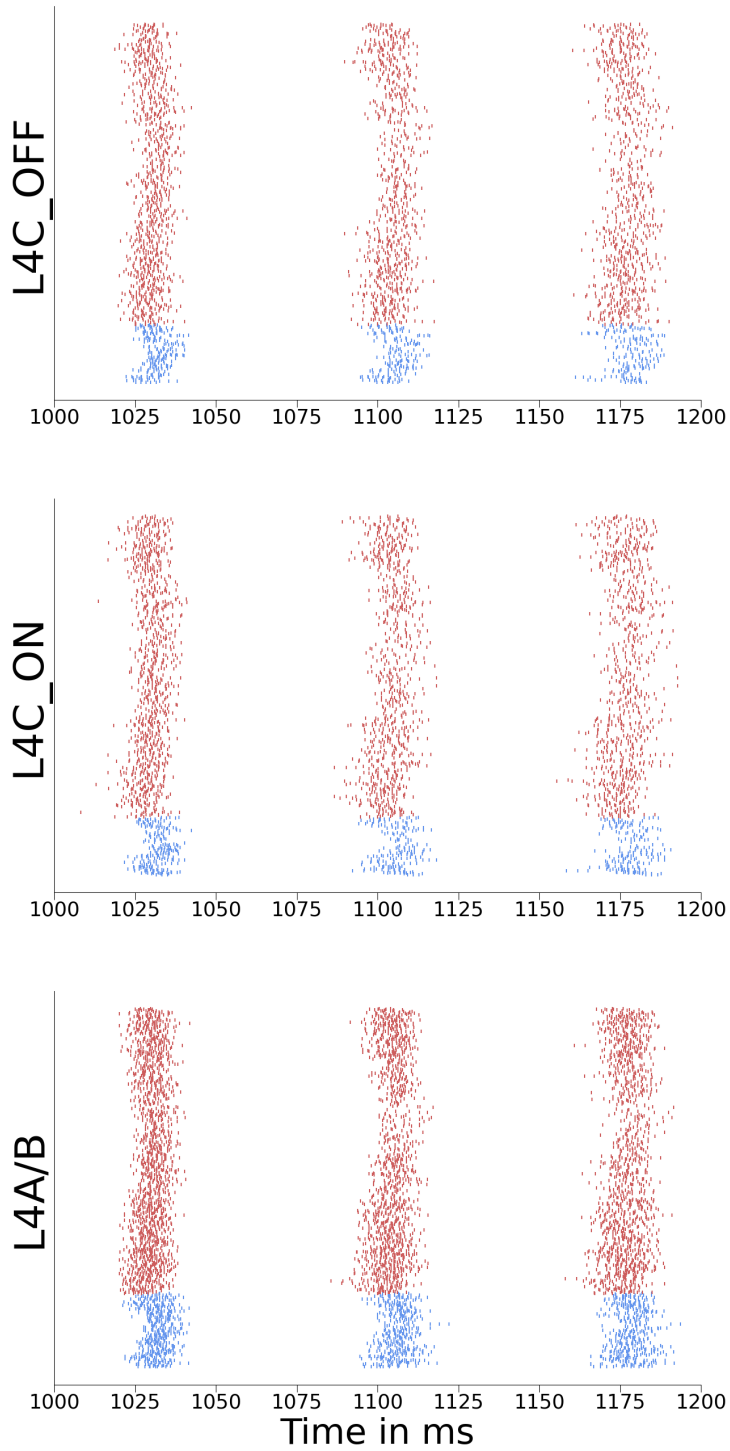


Figure 30: Raster plot slice of 200 ms long simulation, neurons tend to fire all together resulting in the vertical stripes. The neurons are sorted by their preferred orientation resulting in the visible dense blocks.

	L4ABE Retrieved orientations	L4CEON Retrieved orientations	L4COFF Retrieved orientations	L4ABE Tuning prominence	L4CEON Tuning Prominence	L4CEOFP Tuning prominence
No intra-areal connections	17%	89%	76%	0%	55%	45%
Weight modulation	31%	49%	44%	6%	10%	9%
super-localized inhibition	59%	69%	66%	23%	23%	23%
elliptical inhibition	55%	51%	49%	40%	40%	40%
push-pull connectivity	55%	81%	79%	62%	60%	60%
patchy connectivity	81%	81%	79%	68%	60%	60%

Table 13: Percentage of retrieved orientations and tuning prominence of the excitatory layers at each stage of feature.

a comparably steep tuning. However, the final network performs better in retrieving orientations in L4CEOFP and L4ABE. Additionally the orientation prominence is better in all layers in the full model.

7.8 Additional network measures

The patchy connectivity including network (sec:7.6) is able to retrieve most orientations (81%) correct, shows a high orientation prominence (68%) and has firing rates of 19 Hz. We now want to test the network for further capabilities dependent on the input, analyze its statistics and test for additional parameters.

7.8.1 Super-localized inhibition performs best when being circular

Assigning a certain fraction of the inhibitory population to be super-localized enhanced the correct retrieved orientations (sec:7.3). Furthermore we found out that elliptical inhibition in non super-localized inhibitory neurons is beneficent for the orientation map retrieve. This leaves the case of elliptical super-localized inhibitory neurons open. However, since super-localization reduces the average connection distance and ellipticity increases it, we expect a worsening effect. We try out different ellipses long axis values for super-localized inhibitory neurons while non super-localized neurons retain their ellipses long axis of 3.5. Using various ellipses long axis in between 1.0 to 4.0 reveals that the effect on the network is negligible for a long axis of 1.0 – 3.0. Increasing the ellipsis long axis further than 3.0 even has a negative influence on the number of correct predicted orientations. Conceding with increased ellipses long axis the average firing rate of the network rises. This could potentially be the reason for the decrease in retrieved orientations. We proceed with an super-localized ellipsis long axis of 1.0 (circular).

7.8.2 Patchy connectivity allows for dashed line retrieve

All network constructions previous to applying patchy connections are able to retrieve the orientation map with different accuracy's using drifting gratings. However none of them is able to retrieve the orientation map using solid or even dashed lines (not shown here). We now feed solid and dashed line input into the patchy network and retrieve the orientation map.

Both inputs succeed in retrieving the orientation map (fig:31) way above the random baseline of 16.6%. The number of retrieved orientations and the tuning prominence show an equally high value (fig:31). The exhibited average firing rate of both networks in L4ABE is also the same with 13 Hz. However, the firing rate is much lower than that in the grating driven network which fires on average with 19 Hz (sec:7.6). The similar performance of a solid line and a dashed line driven network is surprising as the line should provide more input.

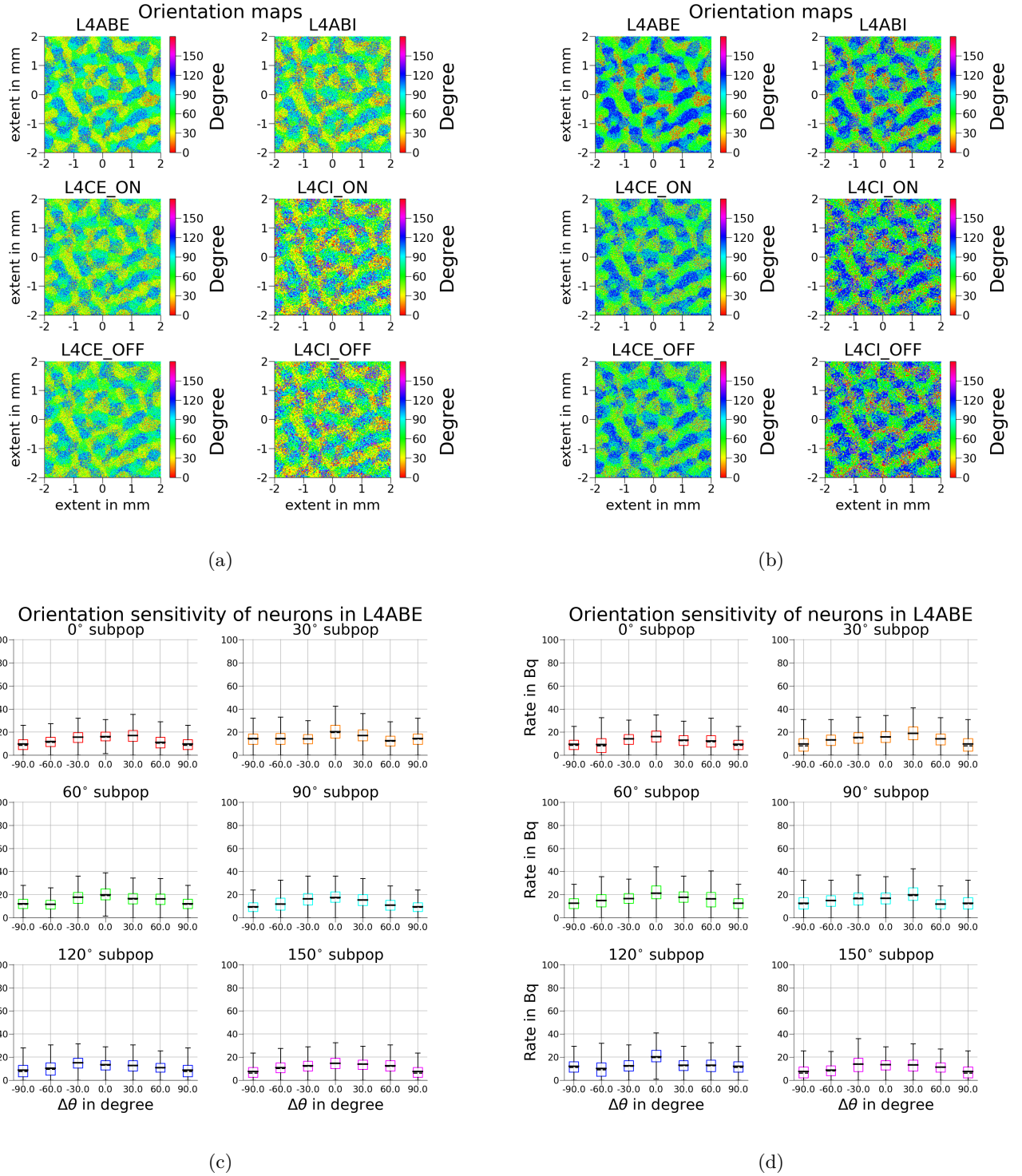


Figure 31: a) Retrieved orientation map using solid lines (fig:14b), it predicts 46% of the orientations correctly b) Retrieved orientation map using dashed lines (fig:14c) predicting 46% of the preferred orientations correct. c) is the to a) corresponding tuning curve with tuning prominence 40%. d) is the to b) corresponding tuning curve with tuning prominence of 40%.

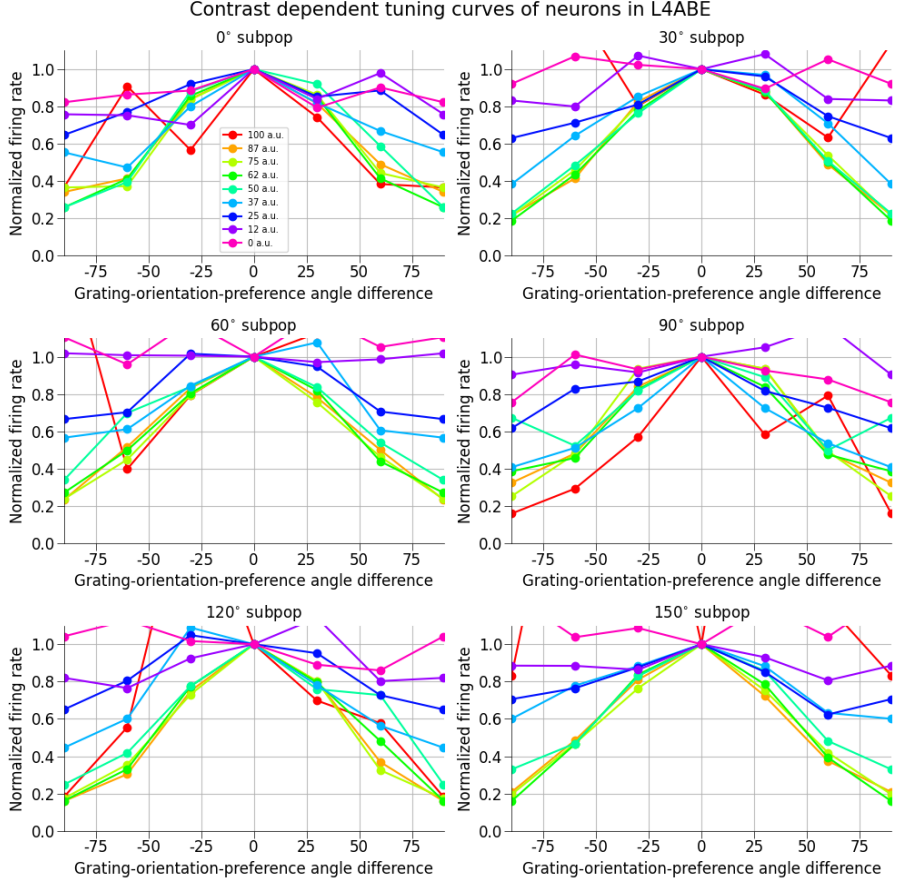


Figure 32: Normalized tuning curves of different network simulations using various grey-scale peak values in the grating input. All peak values in previous simulations accounted for a contrast value of 87%. In the range of 100% to 37% the average tuning curves exhibit an almost identical shape. At 25% contrast the average tuning curves and hence also the orientation map retrieve start to diffuse, any further contrast decrease leads to the loss of orientation tuning. Note that the contrast scale is arbitrarily chosen and 100% is just set such by us.

7.8.3 The network's response is contrast in-varient

Contrast in-variance describes the ability of a network to exhibit the same tuning curve shape indifferent of the intensity of the grating input. Neuron responses in V1 of cat have been shown to be contrast in-varient (Sclar et. al. [SF82], Skottun et. al. [SBS⁺87b]). To test whether the network shows a contrast in-varient response we vary the grey scale peak value of our gratings and plot the resulting normalized average tuning curves in L4ABE above each other. The term contrast is coupled to differences in light intensity. Nevertheless, this concept is not applicable to the network, as there is no connection to light intensity. Therefore we just define some value to be 100% contrast and test in which range around this arbitrarily chosen value the tuning curve does not change shape.

In Figure:32 an almost perfect overlay of the normalized average tuning curves in the range of 100% to 37% is observe. In this area the network's response is contrast in-varient. Furthermore at 25% a transition towards a different shape is apparent. Below this value the response occurs to be non contrast in-varient. Since tuning curves of 12% and 25% do not consistently possess a peak in center anymore, they do not reproduce the orientation map.

7.8.4 Spatial and temporal grating frequency shift

In the previous simulations gratings with a spatial frequency of 2 mm^{-1} and a temporal frequency of 1 Hz are used to retrieve the orientation map. However, many experiments cover a wide range of temporal and spatial frequencies in the gratings and show that the orientation tuning still works.

	0.7 Hz	1.0 Hz	1.5 Hz
1 mm ⁻¹	38%	72%	70%
2 mm ⁻¹	77%	76%	80%
3 mm ⁻¹	57%	44%	48%

Table 14: Percentage of correct predicted orientations dependent on the spatial and temporal frequency of the drifting grating input.

We want to test whether our network can still reproduce the orientation map when both frequencies are varied. We test this dependency by running the network under all possible combinations of $f \in \{0.7 \text{ Hz}, 1.0 \text{ Hz}, 1.5 \text{ Hz}\}$ and $\frac{1}{\lambda} \in \{1 \text{ mm}^{-1}, 2 \text{ mm}^{-1}, 3 \text{ mm}^{-1}\}$.

The network is able to retrieve the orientation map with varying performance under various combinations of grating frequencies in the space and time domain (tab:14). Especially when using gratings of spatial frequencies below 3 mm^{-1} a high number of orientations above 70% is retrieved. The exceptional case arises when the input oscillates with a temporal frequency of 0.7 Hz while the spatial frequency cycles once per milli meter. In this situation the wavelength does not fit to the thalamo-cortical Gabor wavelength anymore. Combined with the slow temporal oscillation neurons of different preferred orientation receive less differentiated input than in the 2 mm^{-1} and 1 Hz case. Gratings with spatial frequencies accounting for more than three cycles per milli metre retrieve below 60% of the neurons orientation correct. The reason for the worse performance becomes overt looking at Figure:33c. Calculating the thalamic firing rates with mexican hat filters in the retina model results in low rates when compared to gratings of lower spatial frequency (fig:33a, fig:33b).

7.8.5 Cortical waves

The raster plot in the patchy network (sec:7.6) shows low global oscillations of neuronal activity in the time domain. However, in order to draw conclusions on the spatial component from spike time plots the sorting of neuron ID's must be well defined. But since we possess the spiking data of 1.4million neurons (experimental data often consists of only 100 neurons) and we use a large spatial area there does not exist a well working sorting of the ID's dependent on their spatial position. Nevertheless, we may arrange the neurons by their sub-population identity. The lowest ID's belong to the 0° preferred orientation and largest ID's are part of the 150° sub-population. In this way sub-population differences could become visible.

The illustrated Figure:34 captures the spike time patterns of every 800th neuron within the comprehensive feature-enabled network driven by dashed lines. Once the activity is presented on the full 19 s time scale and once on shortened time scale of 200 ms providing another perspective. In the complete time scale no differences between the spiking activity of neurons of different orientation preference may be observed. The only visible feature are vertical stripes in Figure:34a. On a shorter time scale (fig:34b) these stripes appear to be several milliseconds of spike activity followed by a short time of silence. Neurons posses a different spiking activity onset implying some spatial structure. Therefore the spatial spiking activity is plotted.

Figure:35 presents a sequence of three in time consecutive spike activities responding to a drifting dashed line input. The dynamic unfolds with activity initiation in proximity to the cortex's upper right boundary (see fig:35a), gradually radiating throughout L4. Intriguingly, both the initial cell sparking the activity and the direction of activity propagation appear disconnected from the orientation map or the inputs spatial location. This waves are similar to the description of Muller et. al. [MCRS18]. They compare the experiment and theory of different types of waves in cat and macaque monkey. One type of observed wave is the traveling wave induced by strong cortico-cortical connections, which is similar to what is shown in Figure:35. We can calculate the speed of our traveling waves, the wave takes around 40 s to travel approximately 4 mm of space. Therefore the wavefront travels with a speed of around 0.1 ms^{-1} . The vertical stripes observed in the raster plot therefore are spatially outspreading waves of cortical activity.

The Power spectrum of the resting state shows qualitatively the same result for the population average and single neurons (fig:36). Peaks at 14 Hz and some higher harmonics are observable. The 14 Hz frequency is the slow oscillation frequency observed in the raster plot (fig:34). When the dashed line starts to drive the network, the power spectra shift their most prominent peak to 19 Hz (fig:37).

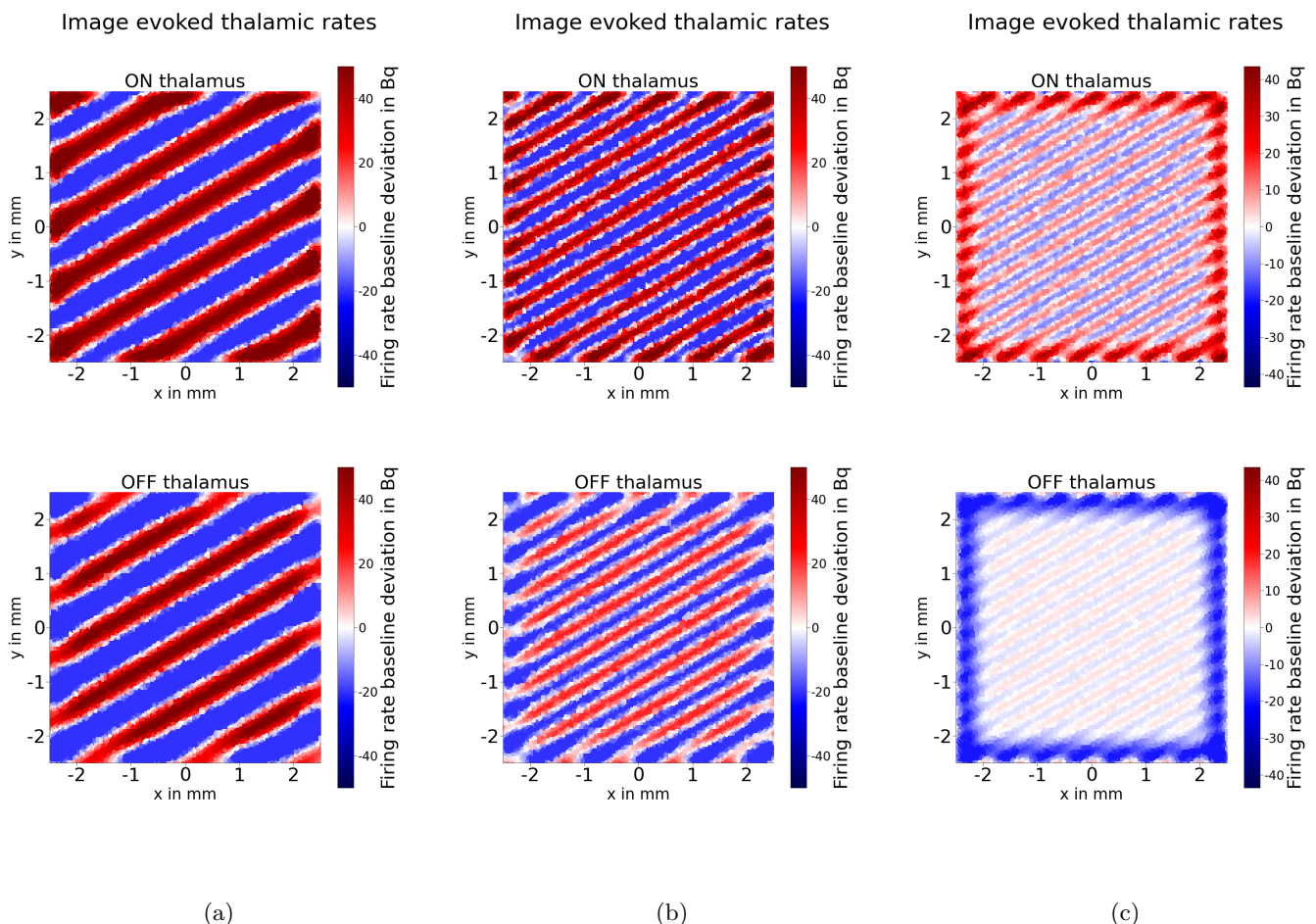


Figure 33: a), b), c) are the thalamic responses to gratings of spatial frequencies of 1 mm^{-1} , 2 mm^{-1} , 3 mm^{-1} .

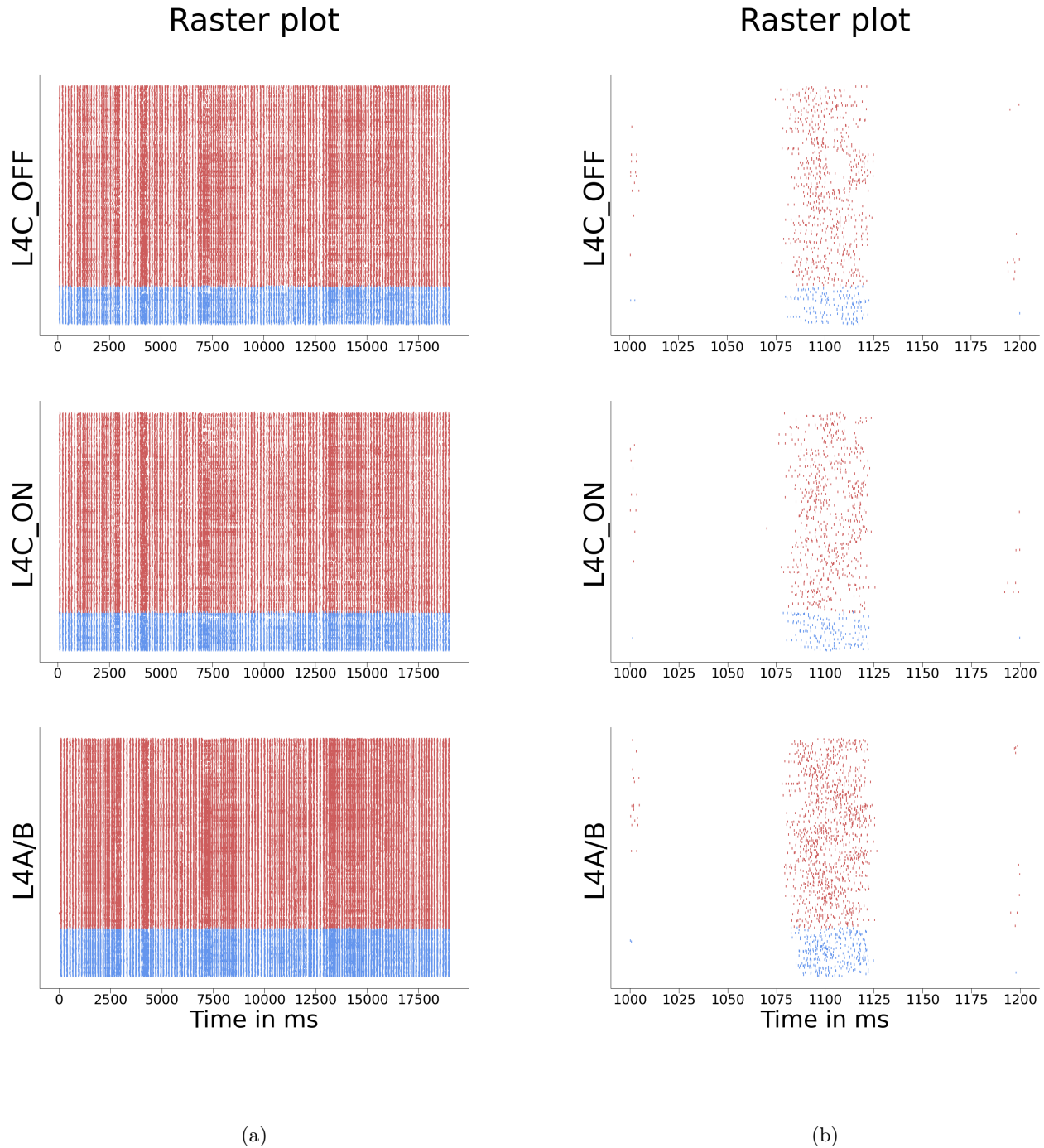
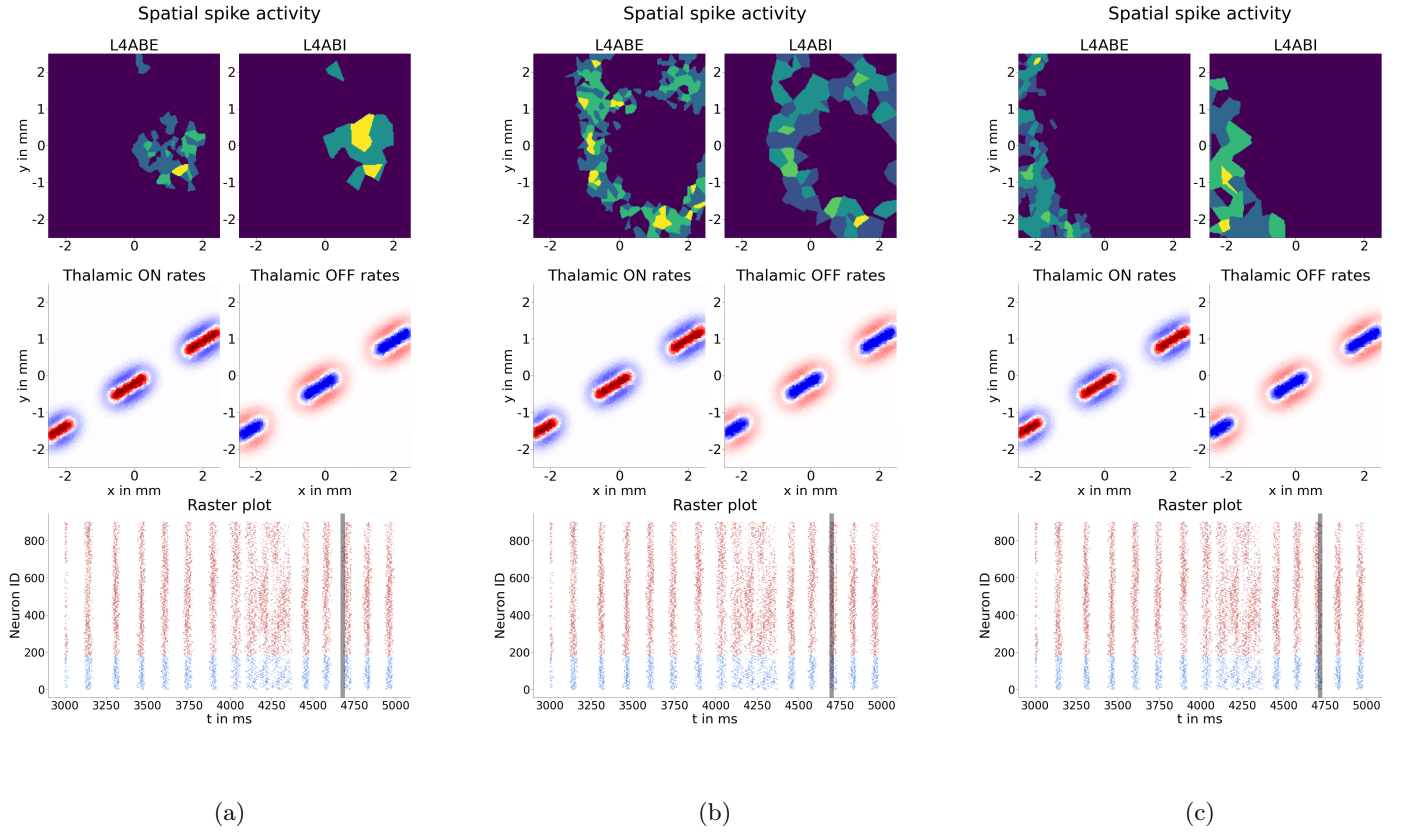


Figure 34: a) Spike time plot showing every 80th neurons spike trains for the full 19 s simulation time of the full network (using super-localized inhibition, push-pull connectivity, patchy connectivity, weight modulation and elliptical inhibition) and a dashed line input. All neurons in the network tend to fire together showing slow oscillations in the time domain. Whenever a grating is shown to the retina the slow oscillations frequency increases, the to the grating corresponding sub-populations exhibit the strongest firing rate increase. b) Same as in a) but on a zoomed in time scale.



(a)

(b)

(c)

Figure 35: a) Spatial plot integrating 10ms of spikes and interpolating that activity on a grid. b), c) subsequent plots showing the activity after a)

7.8.6 A noise resistant network

We might test the networks behaviour under adding noise to the thalamic input, in every time step we first calculate the thalamic rates as described in section:6.1.2 but each thalamic neuron receives an additional uniform distributed firing rate between -18Hz and 18Hz (fig:38).

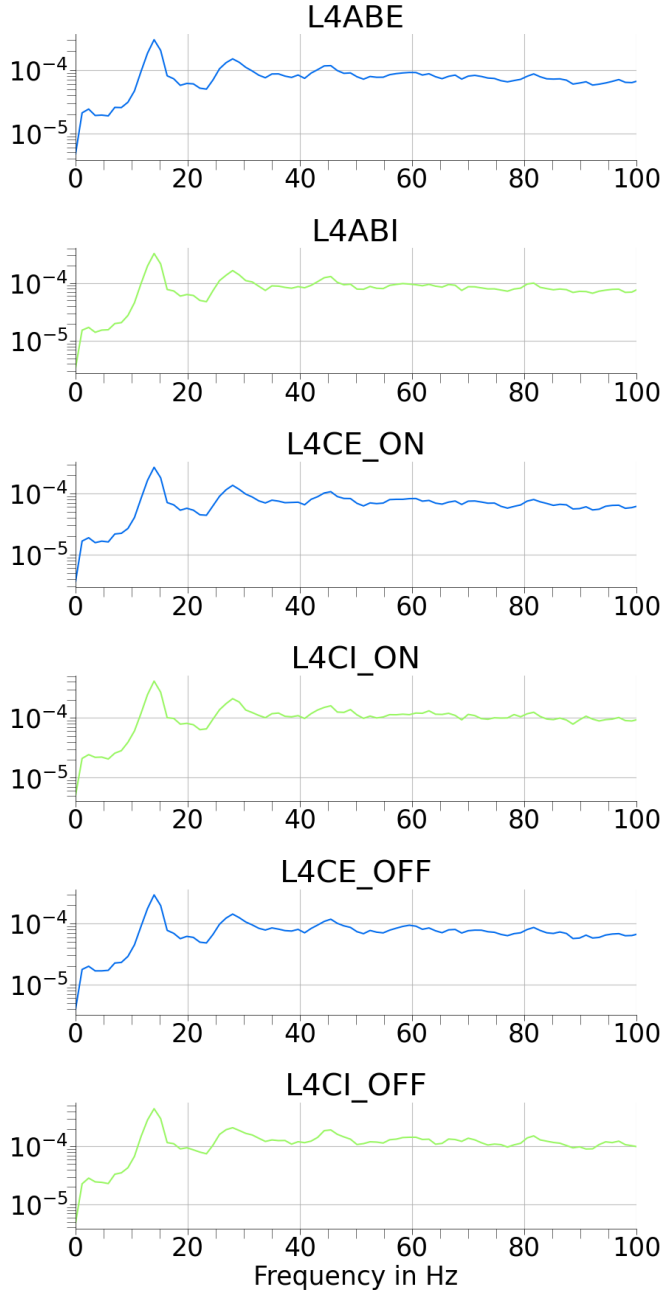
Running the network with different noise values ($\text{noise} \in 0, 6, 12, 18, 24, 30$) reveals that the number of correct retrieved orientations is 45% at 0 Hz and begins to deteriorate when exceeding 24 Hz. Following equation:28 we calculate the signal to noise ratio to be 0.75 when using a noise of 24 Hz

Table:15 summarizes the correct orientations resolved by layer and noise. As expected the network performs the best in L4ABE when no noise is added. With increasing noise the number of correct retrieved orientations steadily decreases in all layers. Even at a signal to noise ratio below 1.0 the network is still able to retrieve significantly more orientations correct than expected by the baseline of 16.6%. The situation of using 24 Hz is depicted in Figure:38.

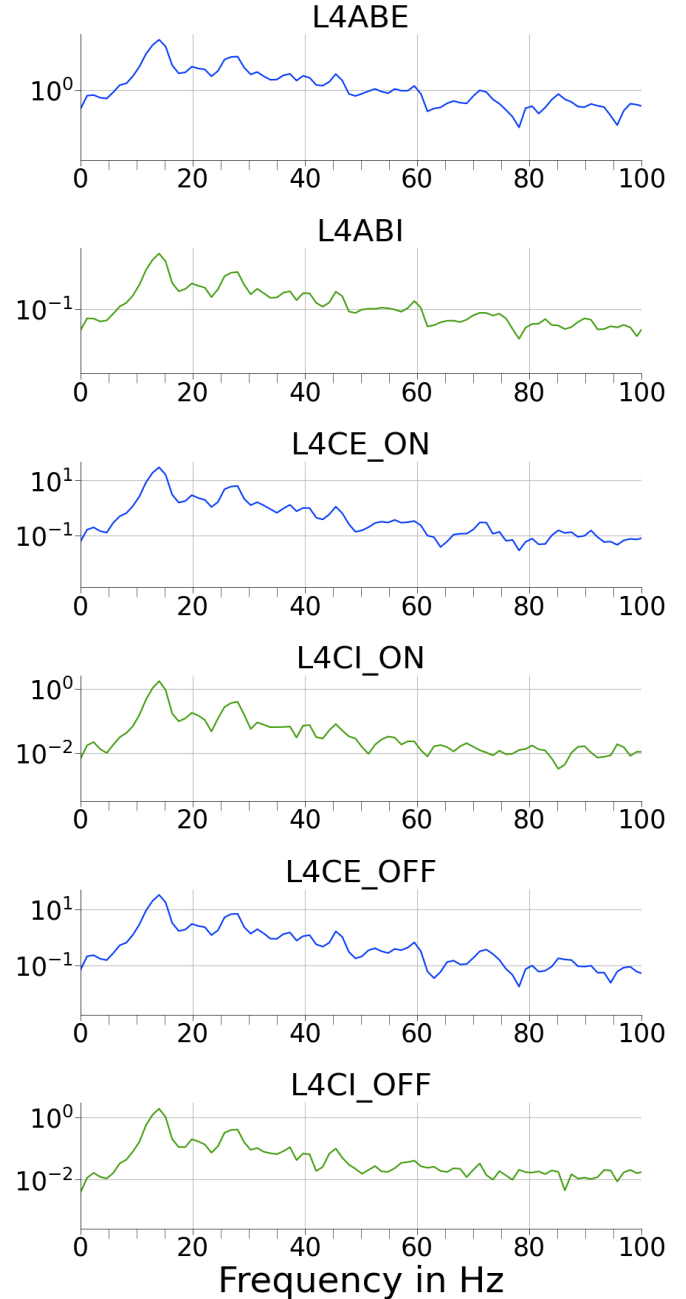
	L4ABE	L4ABI	L4CEON	L4CION	L4CEOFF	L4CEOFF	Signal to noise
0 Hz	46%	43%	39%	39%	39%	39%	inf
6 Hz	46%	43%	39%	40%	39%	40%	1.5
12 Hz	43%	39%	35%	35%	35%	35%	1.1
18 Hz	36%	33%	30%	30%	30%	30%	0.75
24 Hz	33%	30%	27%	27%	27%	27%	0.5
30 Hz	24%	22%	20%	20%	20%	20%	0.35

Table 15: Correct retrieved orientations dependent on the layer and noise bin of the uniform distribution. All simulations are performed with moving dashed lines (fig:14c). Furthermore the signal to noise ratio for each configuration is calculated according to equation:28.

Resting state power spectrum of single neurons Resting state power spectrum of the population



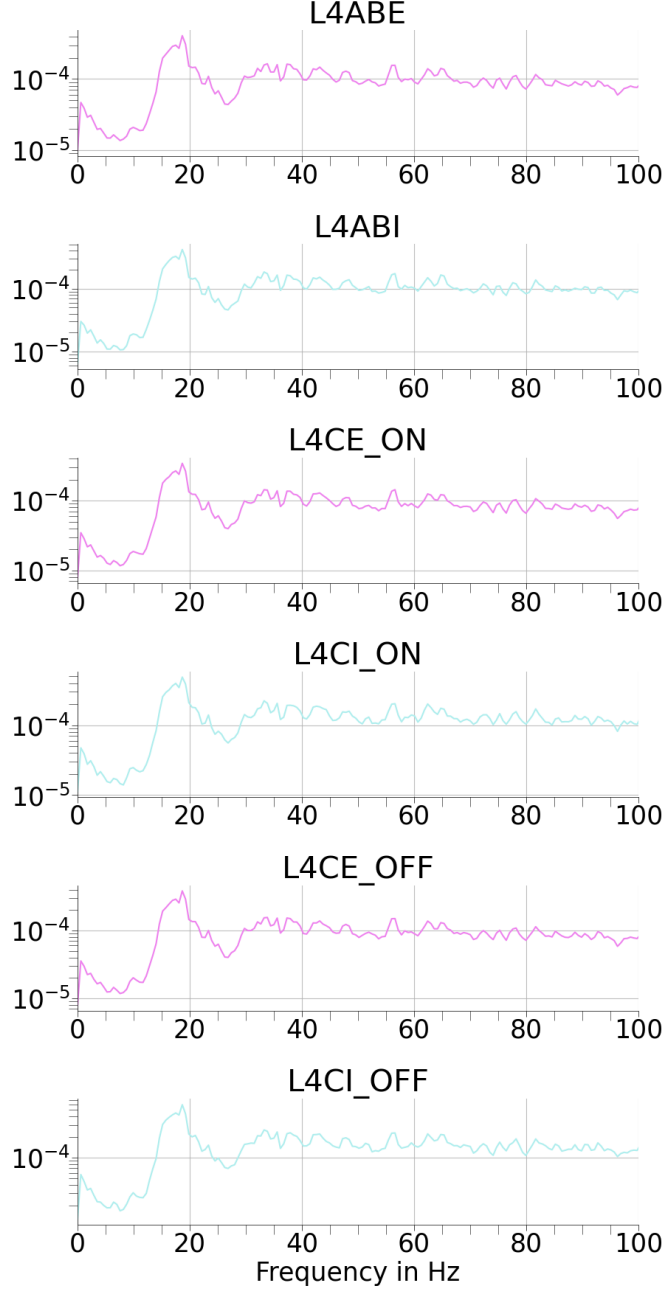
(a)



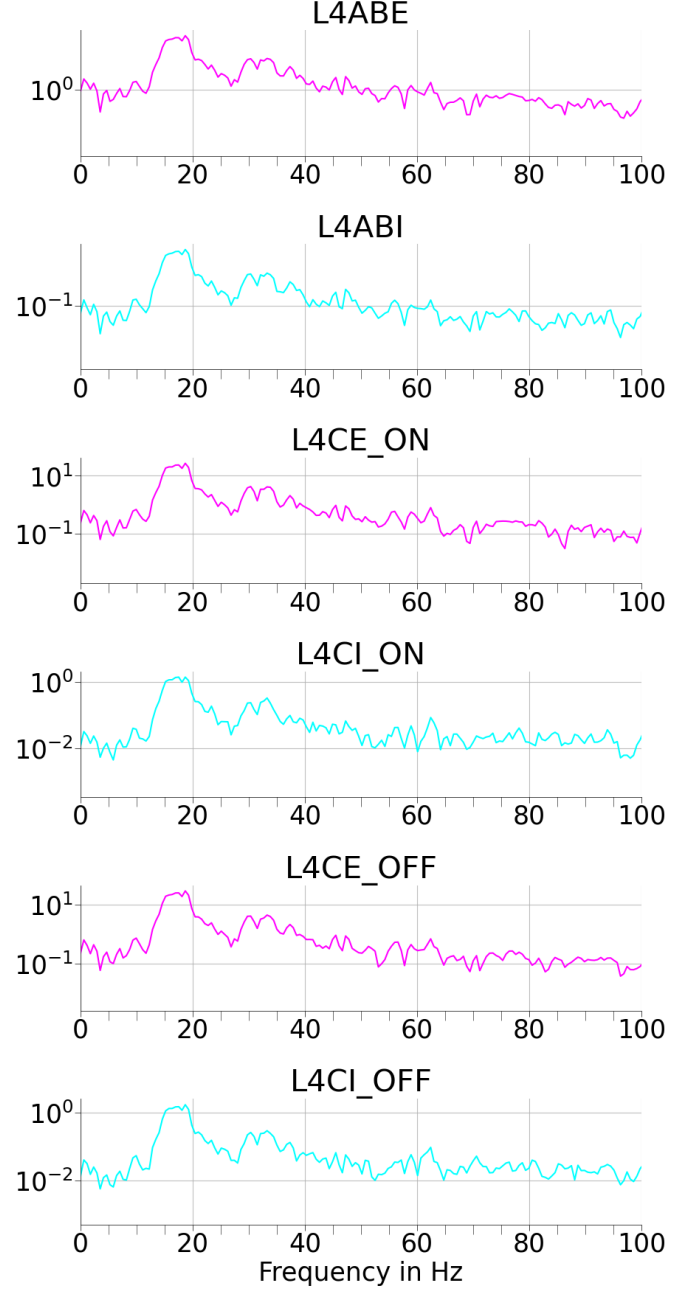
(b)

Figure 36: a) Power spectrum of the whole populations while no retina input is present, the most prominent peak appears at around 14 Hz representing the synchronized activity occurring during drifting grating experiments. Additionally the second harmonic at 28 Hz is visible. b) Power spectrum of single neurons, qualitatively the result is the same as in a) implying no population effects.

Driven state power spectrum of single neurons Driven state power spectrum of the population



(a)



(b)

Figure 37: a) Power spectrum of the whole populations in the driven state exhibiting peaks at 19 Hz and its higher harmonics. b) Power spectrum of single neurons in the driven network state. The result is qualitatively the same as in b) implying no population effects.

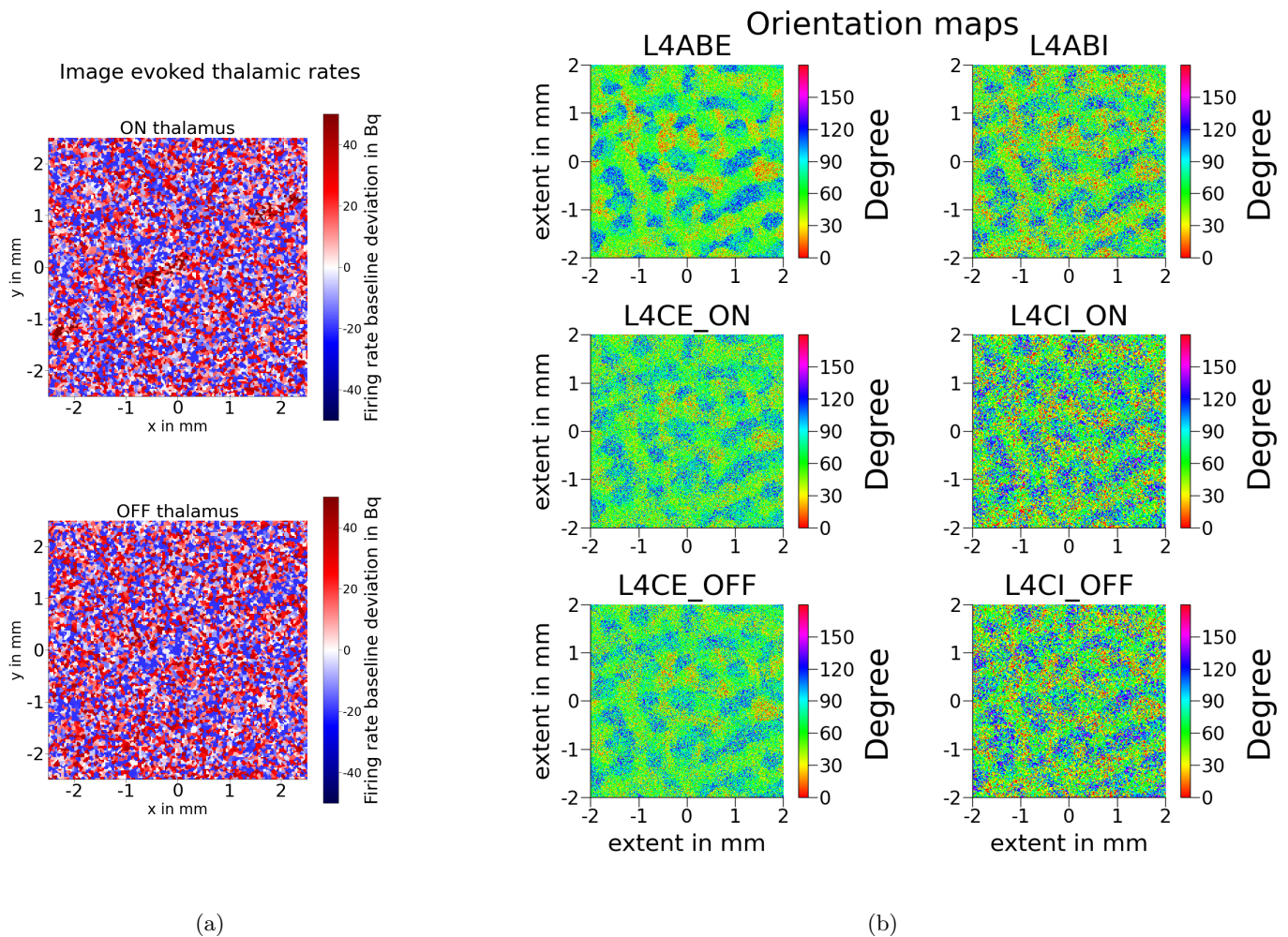


Figure 38: **a)** Evoked rates in the thalamus by a dashed line with uniform distributed random noise between -24Hz and 24Hz . **b)** Corresponding orientation map.

PSP dependent on the membrane Potential

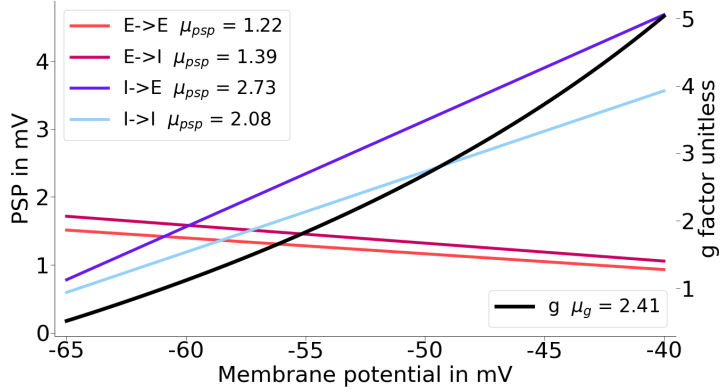


Figure 39: PSP's of neurons with same preferred orientation as used in section:7.6. The PSP's may be calculated by combining the peak conductance's B of weight modulation of Figure:11 with the conductance differential equations:1, 2, 25. Conductance based PSP's dependent on the membrane potential split in all four efficacy combinations. The membrane potential is shown in the range of the equilibrium potential to the spiking threshold. At higher membrane potentials inhibitory evoked PSP's are stronger than excitatory evoked ones, while at lower potentials excitatory evoked PSP's are stronger. Averaged over the whole membrane potential range the Inhibitory synapses elicit a stronger response than the excitatory ones. The average g factor is around 2

7.9 Conductance based neurons balance the network at g equal to one

We want to evaluate the E I network balancing using conductance based neurons. For this purpose the calculations for the approximated PSP in the current based case is consulted (sec:6.4.3). The parameter choices of the patchy network (sec:7.6) lead to PSP's in the form of Figure:39.

Figure:39 depicts the approximated (sec:6.4.3) PSP strengths of conductance based neurons dependent on the target neurons membrane potential. The conductance instantiated network shows stronger IPSP's at lower membrane potentials and higher ones at increased membrane potentials. For the EPSP's the situation is reversed. The voltage dependence in conductance based neurons technically leads to a membrane potential dependent g factor, which however has no use.

For further increase of the E I balancing at lower average g factors we lower the PSP's of all synapses to $\frac{2}{3}$ of their original strength. This will increase the inhibition induced by the leak term allowing for lower inhibitory synapse strengths. Therefore we decrease the inhibitory synapse strengths drastically compared to the situation of fig:39.

Figure:40 shows the voltage dependent PSP's and the average PSP's. Excitatory and inhibitory PSP curves cross at higher membrane potentials than in Figure:39. We expect this behaviour due to the above introduced excitatory strengthening changes. The average value for $E- > E$ is close to the average value of $I- > E$ indicating that the average g factor must be close to one.

Figure:41 visually encapsulates the firing rate distributions of two comparable networks, distinguished by their chosen E I balancing factors. Notably, both systems express comparable firing rates. Furthermore, the inhibitory firing rate distribution manifests as two distinct overlapping distributions in the configuration balanced at average g equal to 1 (fig:40), a feature prominently depicted in Figure 41.

7.10 Coefficient of variation

Figure:42 displays the coefficient of variation divided into the different layers of the network state of section:4.2 during stimulation. Excitatory coefficients of variation show an average of around 0.9 while inhibitory ones lie between 0.9 – 1.1. Experimental data lies in the same regime (Softky et. al. [SK93]).

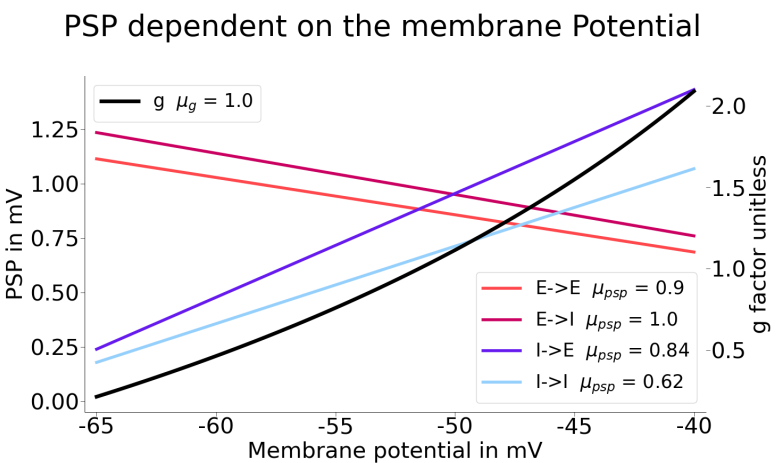
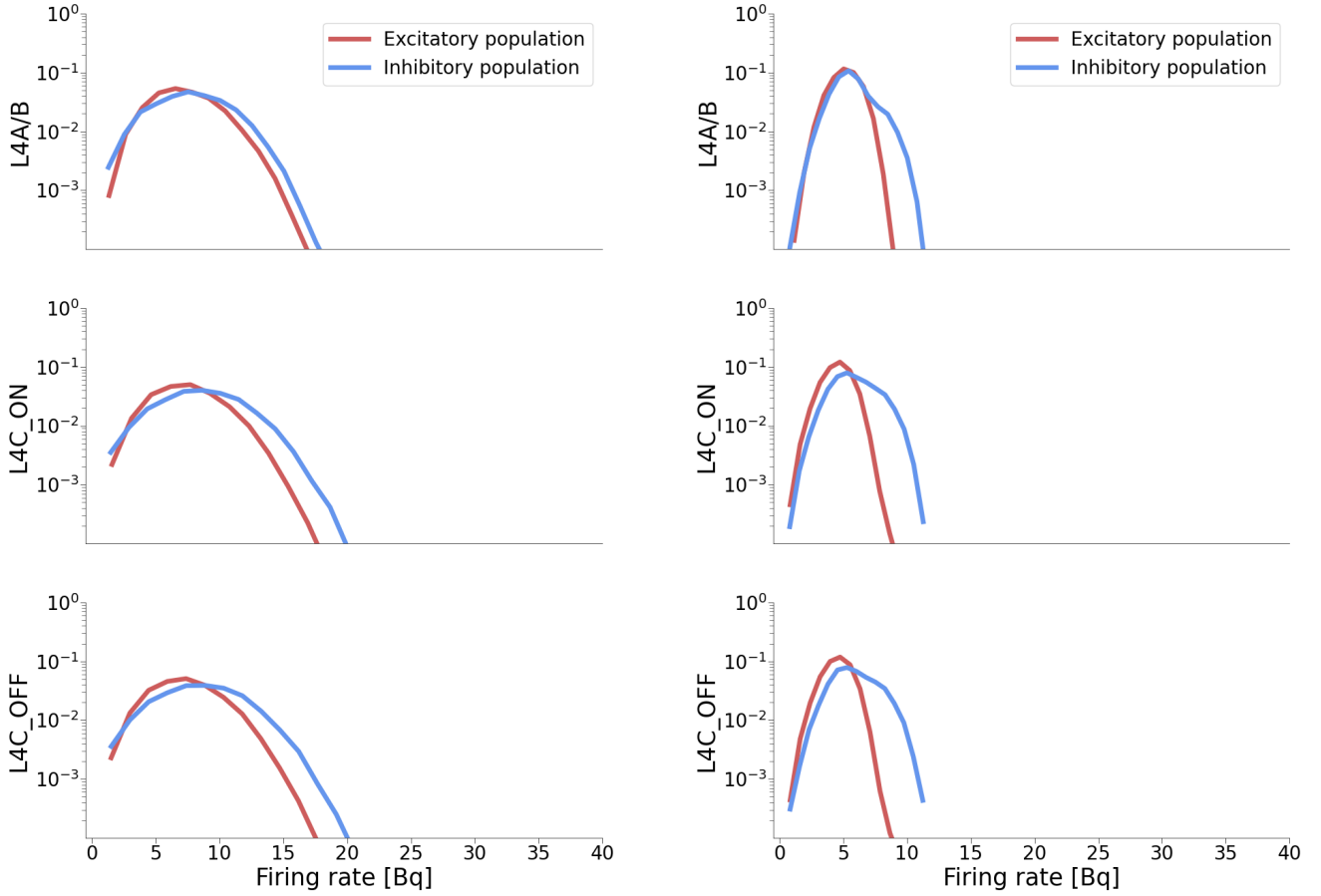


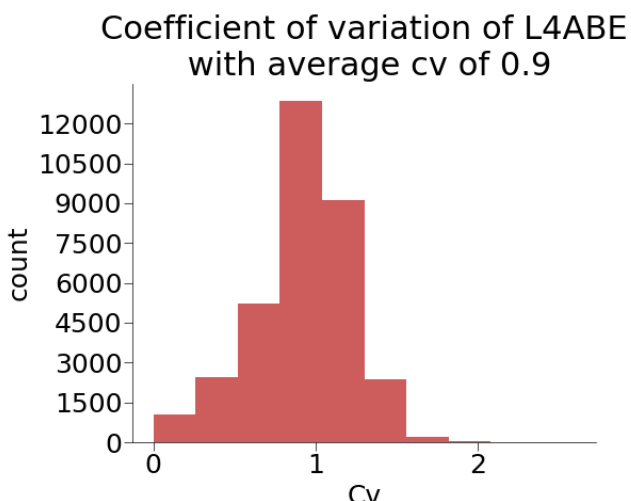
Figure 40: Same as fig:39 using the model of section:7.6, but with $I- > E$ and $I- > I$ weights being smaller by a factor of 2.4. Conductance based PSP's dependent on the membrane potential split in all four efficacy combinations. The membrane potential is shown in the range of the equilibrium potential to the spiking threshold. At higher membrane potentials inhibitory evoked PSP's are stronger than excitatory evoked ones, while at lower potentials excitatory evoked PSP's are stronger. Averaged over the whole membrane potential range the Inhibitory synapses elicit a stronger response than the excitatory ones. The average g factor is around 1



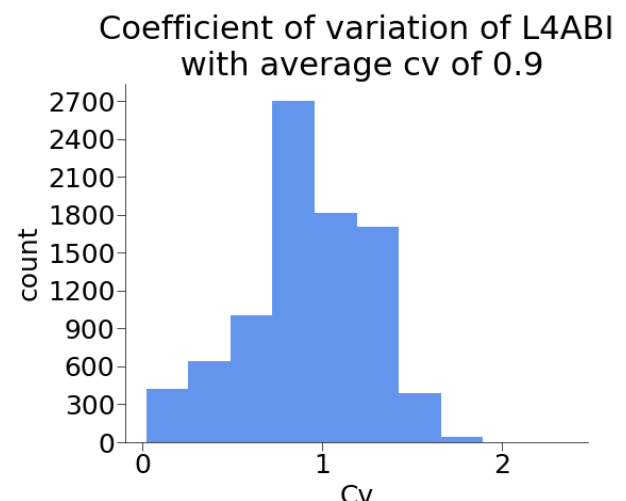
(a)

(b)

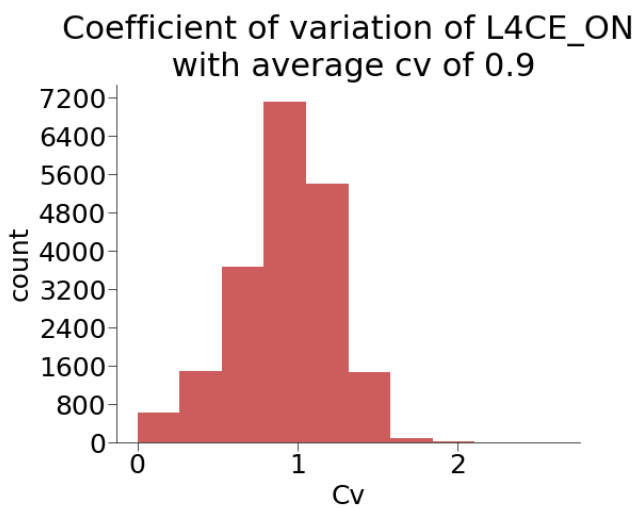
Figure 41: a) Firing rate distribution in a conductance based network as described in section:7.6. b) Firing rate distribution in the same network configuration as in a) but with the E I balancing changes introduced in fig:40. The firing rates similar in both systems. However, the fig:40 splits into two distributions in the inhibitory population



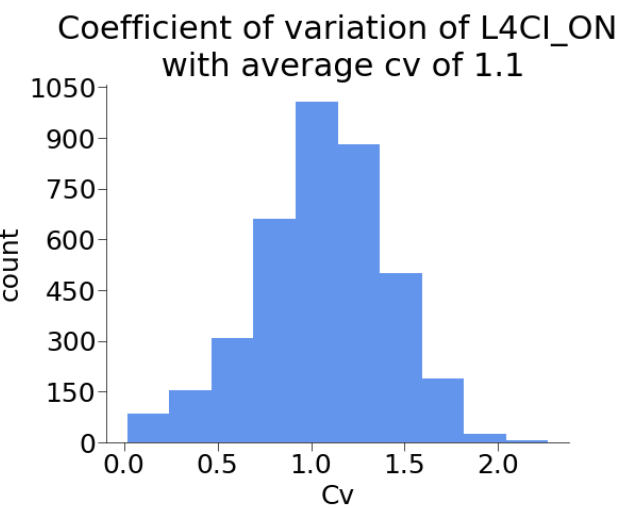
(a)



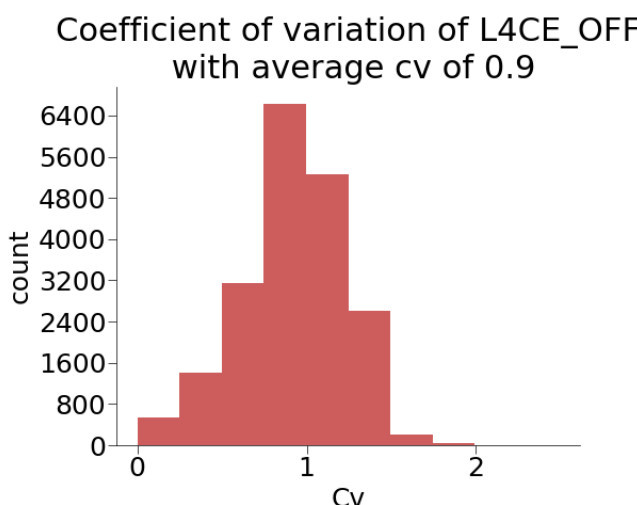
(b)



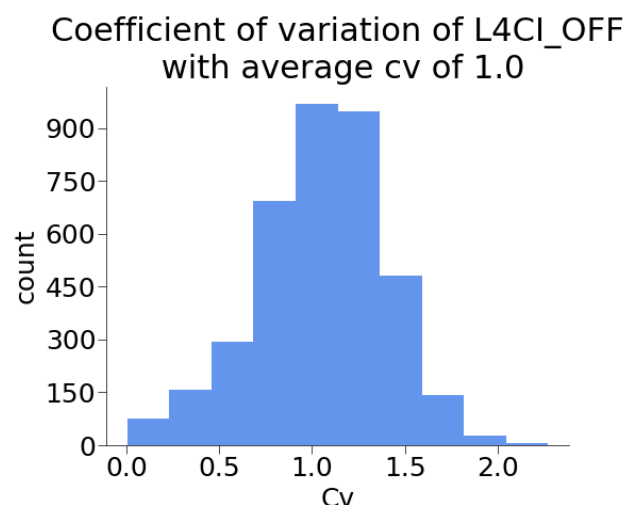
(c)



(d)



(e)



(f)

Figure 42: Coefficient of variation during stimulus in a) L4ABE, b) L4CEON, c) L4CEOFF, d) L4ABI, e) L4CION, f) L4CIOFF

8 Conclusion

8.1 Summary

The work presented in this thesis addresses the question of how the recurrent connectivity supports the orientation map and the emergence of steep tuning curves. We start with a network consisting of no other intra-areal features than the isotropic connectivity (sec:7.1). In order to investigate the proposed question we then subsequently add various connectivity patterns analyzing their individual effects. Starting with the weight modulation (sec:7.2), the network is able to retrieve the orientation map using moving gratings as input mainly in L4C. When using super-localized inhibitory neurons the model also allows for retrieves in L4AB (sec:7.3). Combining elliptical inhibition and push-pull connectivity further boost the networks capability to discernible grating angles from each other and enhances the number of correctly predicted preferred orientations (sec:7.5). The L4AB exclusive long range patchy connectivity elevates the orientation selectivity to a level where additionally to the grating also solid and dashed lines may extract the orientation map (sec:7.6).

Moreover the final network shows some other properties. The model is contrast invariant showing tuning curves of similar shape under a wide range of grating intensities (sec:7.8.3). Furthermore it is noise resistant and can retrieve the orientation map with a signal to noise ratio of 0.75 in the thalamic input (sec:7.8.6). Gratings of various temporal and spatial frequencies may retrieve the orientation map (sec:7.8.4). All features are produced in a network showing realistic E I balancing utilizing conductance based neurons.

8.2 Discussion

8.2.1 Choice of inputs

We introduced three different types of inputs (fig:14) driving the network after thalamic firing rate conversion by a retina model. The most important input is the drifting grating, which is abundantly used by experimental and theory studies (Understanding vision [Li14]). In our network it serves the purpose to first create the orientation map and then in many cases also to retrieve it. After using the grating for coarse calibration of the weight modulation, elliptical inhibition and push-pull connectivity, we eventually reach a state where the grating already retrieves almost all neurons correctly. At this point the solid and dashed line become more interesting because in contrast to gratings they are often encountered in nature. Indeed the network is able to retrieve the orientation map given a line like input if patchy connections are present.

8.2.2 Isotropic network

The initial fail of the orientation map retrieve may be accounted to the spill over excitation caused by excitatory neurons of different iso-orientation domains interacting strongly with each other. Consider for example the 0° grating which elicits the 0° iso-orientation domains, the activity in the 0° iso-orientation "spills over" to the 30° iso-orientation domains. In consequence every neurons activity is only sparsely influenced by its preferred orientation.

8.2.3 Weight modulation

The main issue of the failed orientation map retrieve consists of iso-orientation domains not being able to keep the activity within themselves. We solved this by modulating the connection weight such, that neurons in the same iso-orientation domain have a stronger coupling with each other than neurons in different ones do. This weight modulation is determined by three parameters: the high weight factor, the low weight factor and the width as described in equation:14. By testing out different variable combinations we end up with a well working set of parameters (fig:21). Also other simulation studies implement weight modulations such as Billeh et. al. [BCG⁺20] which choose a similar functional form as we do and observe orientation tuning. Furthermore Znamenskiy et. al. [ZKM⁺24] measured the conductance of neurons based on the difference of preferred grating orientation and find the conductance to be of similar shape as a tuning curve. Both studies find an enhanced connection strength between excitatory and inhibitory neurons of similar orientation.

8.2.4 Inhibitory effect

Elliptical projecting inhibition is one feature of inhibitory neurons Peng et. al. [PTP⁺21] find in the presubiculum of rat to enhance orientation tuning. Due to the similar purpose of rat presubiculum and V1 in macaque, we concluded in section:6.3 that it is reasonable to assume elliptical inhibition in V1. Akin to Peng et. al. [PTP⁺21] we also find the elliptically projecting inhibition to be beneficial for the orientation tuning. However, we may only hypothesize about the reason for the enhancement. One possibility is, that elliptically projecting inhibition supports the weight modulation in preventing spill over excitation (sec:7.1) to happen. According to the argumentation, the weight modulation impairs iso-orientation domains of different preferred angles to pass activity between each other. The very local inhibition hardly plays any role in that, since it mainly targets excitatory neurons in a close vicinity mostly being from the same iso-orientation domain. Since elliptical neurons possess a larger average connection distance, a larger portion of neurons outside of its own iso-orientation domain is targeted. Combined with the almost not decaying weight modulation of elliptically projecting inhibitory neurons, other iso-orientation domains are cooled down stronger.

Super-localized inhibitory neurons mainly affect the orientation tuning in L4AB, which is counter intuitive recalling that most super-localized neurons are located in L4C. We might resolve that issue by thinking about the form of projection from L4C to L4AB. Each excitatory neuron asserts distance dependent connections described by a linear term multiplied with an exponential (Ellipsis long axis of 1 in fig:12). For a possible explanation let us assume the same one iso-orientation domain in L4C and L4AB. Each neuron in L4AB receives most of its connections from L4C neurons being λ_{ij} apart. Now looking at one excitatory neuron located in L4AB, it will receive most of its inputs from λ_{ij} apart L4C neurons. These are therefore mainly located in a different iso-orientation domain. Hence the input from neurons outside our observed iso-orientation domain predominate the relevant input for the excitatory neuron in L4AB. Super-localizing inhibitory neurons in L4C prevent inhibition of these predominantly relevant λ_{ij} away neurons as they only target neurons very close by. This Subsequently strengthens the input in L4AB neurons of the same iso-orientation domain by L4C neurons.

In section:7.3 we found out that super-localizing a certain fraction of the inhibitory population leads to an enhanced orientation map retrieve. However, further localizing these inhibitory neurons did not show any effect at all (sec: 7.3.1) implying a transition of the average connection distance where the observed effect occurs. This raises the question where this transition point lies? We may utilize section: 7.8.1 concerning about super-localized inhibitory neurons being elliptical, which effectively raises their average connection distance. And indeed an elliptical long axis of 1.0 – 3.0 does not show any effect, but surpassing this value decreases orientation tuning. Therefore it may be concluded that undercutting a certain value of average super-localized inhibitory neuron connection distance increases orientation tuning and lowers the firing rates.

8.2.5 Function and implementation of the push-pull connectivity

We introduce the push-pull connectivity by arguing that the cortex must react to the correlated input from the thalamus with a connectivity pattern. This connectivity pattern shown in Figure:8 is determined by calculating the correlation coefficient, but for computational feasibility we omit all correlation interactions between neurons of different preferred orientations and justify this by arguing that the correlations are negligible. This statement slightly contradicts our own calculation shown in Figure:8 where the interaction between two neurons with 30° to each other rotated Gabor filters accounts for a correlation of 30%. However, most neurons of different preferred orientations are not close to each other decreasing most of these interactions drastically. Therefore we would expect only barely noticeable changes in the network state when implementing interactions between neurons of different preferred orientation.

Even though we have arguments implying a mathematical model to account for push-pull connections, there is an experimental lack of evidence to hard prove whether this model is true or false. Additionally there is no experimental hint on how many connections are influenced by the correlation and how strong the weights must be since real tissue does not discriminate connections into push-pull and isotropic but rather superimposes both. Therefore in a real brain a connection

would be influenced by push-pull correlation and isotropic connectivity at the same time. Hence we need to test how many connections should be push-pull and how strong their weight must be. This approach's weak point is, that we find the "real" values for weight strength and connection probability by searching a local maximum of the correct predicted orientations during an orientation map retrieve which might has nothing to do with each other. However, we find the fitting weight for 35% push-pull connections to work best with a weight close to that of the isotropic connectivity and since the main feature of L4C is the orientation map, the assumption and apparently working mechanism of the push-pull connectivity enhancing orientation tuning seems is sound and seems natural.

8.2.6 Function and implementation of the patchy connectivity

Experimental results show that long range excitatory connections in L4AB between neurons of the same preferred orientation exist. We implement them. However, we do not possess any information about the number and weight of these connections. Therefore we need to test for different values of connection numbers and weights and test their influence on the orientation map. Nevertheless, there is no prove if the orientation map is the correct metric to maximize for in order to find the "true" parameters for the patchy connectivity. Nor do we know if these two things are related at all. Although the assumption itself seems evident and most likely.

The grating is an object extending to the whole visual field in the model. Subsequently its response is delivered to the entire L4C which sends it up to L4AB. The patchy connectivity links neurons of same preferred orientation in L4AB together, but how does the network with the patchy connectivity retrieve a significantly larger amount of correct orientations? We may think of two reasons resulting in this behavior. Firstly a higher number of patchy connections directly results in a decrease of isotropic connections, which are responsible for the "spill over activity". And secondly our implementation of the patchy connectivity asserts connections in an ellipse around the source neurons indifferent of the distance. Hence resulting not uniquely in long range, but also in short range connections. Therefore we might think about the patchy connectivity in the long range inter-iso-orientation domain linking and the push-pull similar short range intra-iso-orientation domain part. As we know of the push-pull connectivity to enhance the orientation map in L4C it makes sense that the patchy connectivity's short range part has a similar effect.

Meanwhile the long range part is responsible for the possibility to activate iso-orientation domains that are not directly activated. As the solid and dashed line do not cover the whole field of vision, neurons outside this input area are not directly activated. However, even neurons that are further away from the center are retrieved correctly above the level of chance (fig:31b). Only the long range patchy connections can be the reason for that. The combination of the long and short range patchy connections enhances each other in our model.

8.3 Predictive coding

Predictive coding describes a hypothesis of how the brain processes information. According to it each layer tries predict the activity of its preceding layer, while errors between prediction and actual activity are feed-forwarded to subsequent layers (Rajesh et. al. [RB99]). Upon perceiving a dashed line, our model is able to observe its orientation correct when the patchy connectivity is active. The orientation map retrieve is not only enhanced in L4AB where the patchy connectivity resides but also the orientation tuning in L4C improves. Hence the higher level L4AB predicts the preferred orientation of each neuron better than L4C and then enhances orientation tuning in L4C by sending feedback signals.

Furthermore when using the dashed line in the patchy network (sec:7.6) iso-orientation domains tend to have their orientations retrieved correctly. Even if the iso-orientation domain is not directly traversed by the input and lies in the inter-spaces of the dashed line. Therefore L4AB does also recognises the dashed line as a coherent object and feedback's this information to L4C. Hence the two layer network possesses two features which are predicted by L4AB and feed-backed to L4C.

8.3.1 Frequency shift

In their study, Foster et al. [FGNP85] meticulously measured the firing rates of Macaque V1 and V2 neurons in response to gratings characterized by varying spatial and temporal frequencies. Their findings reveal an expansive region wherein neuronal activity exhibits pronounced strength. Our simulations reproduce this behaviour in the sense that the orientation map retrieve is covert by a wide range of inputs. However, since we just one to one mapped the thalamo cortical connections and do not account for different cell types (for example simple and complex cells) the precise region does not match the experimental one. Figure:33 discloses why the orientation map retrieve performs worse with high wavelength spatial frequencies. The mexican hat filters do not evoke high firing rate contrasts in the thalamus such that the thalamo-cortical input is rather low. The filter operation seems to be not tuned for that kind of input. This is also confirmed by theoretical calculations of the elicited response to a sinusoidal (Understanding Vision [Li14]), where it is shown that exceeding certain values of wave vectors results in low evoked activities.

8.3.2 Balancing the network at low g factors

Most previous studies such as the microcircuit (Potjans and Diesmann et. al. [PD12]) and the mesocircuit (Senk et. al. [SHvAD18]) use current based neurons for reasons of simplicity. However, current based neurons omit the membrane potential dependent effect of an impinging spike. Even more crucially they also allow for arbitrary low membrane potentials. Therefore it appears reasonable to assume a strong impact on the network balancing when changing the neuron model. Furthermore current based networks require bio-physiologically unrealistically high inhibitory synapse strengths. The g factor modulating the relative strength of an inhibitory neuron compared to an excitatory neuron is usually set above 4 (Brunel [Bru00]). As a matter of fact we require much lower average g factors using conductance based models. Figure:41 depicts that a conductance based model balances at low rates when using an average g factor(sec:6.4.3) of 2 or even 1.

But why does the conductance based neuron model allow for network balancing at lower g factors? When starting at the equilibrium potential (-65 mV) the inhibitory PSP is negligibly small compared to the excitatory PSP. Therefore the membrane effectively only integrates the excitatory signals. At a certain membrane potential the situation reverses and inhibition dominates above excitation (fig:39,40). This effect additionally gets bolstered by the leak term strengthening at higher potentials. The membrane potential always needs to transition through the high inhibition area before emitting a spike. Therefore the average g factor in the conductance based system is not representative. Consequently it also is not an appropriate measure to compare with the classical g factor in current based systems. A more significant value would be the maximal g factor which arises close to the threshold. In the case of the patchy network (sec:7.6) the maximal g factor is about 5 and in the modified version (fig:40) the maximal g factor accounts for 2. Nevertheless, independent of taking the average g factor or the maximal g factor a balanced network way below a g factor of 4 is possible. Additionally PSP's are usually measured at the resting potential (for example Peng et. al. [PBTK⁺17]) such that experimental studies mostly cover the minimal g factor case. Hence both of the presented network configurations do not contradict the experiment. Since both configurations balance the network, it is very probable that an experiment resembling configuration in-between these extremes does exist.

An unexpected feature of firing rate distribution of the lower g balanced network (sec:7.9) is its shape for the inhibitory neurons (fig:41b). It appears to consist of a mixture of two distributions, moreover the higher frequency distribution seems to possess fewer neurons in L4AB than in L4C. Since we also have less super-localized inhibitory neurons in L4AB than in L4C, it seems reasonable to identify the high frequency population as super-localized and the low frequency population as non super-localized. But why do they differ?, we did not alter their input, but their output. Paradoxically we would expect the super-localized inhibitory neurons to deactivate their excitatory sources and hence would expect them to have a lower firing rate than the non super-localized ones.

8.3.3 Network capabilities

Section:7.8 introduces some network capabilities also verified in various experiments. The advantage of our network compared to its predecessors (the microcircuit and mesocircuit) and compared

to other network models is the unification of various concepts. We implement multiple connectivity patterns and are able to reproduce many biological features at the same time. The most important capability is to retrieve the orientation map when using a dashed or a continuous line, but since we discussed this before in multiple sections of the discussions we will here mainly focus on the other features.

Similar to the problem of retrieving the orientation map with different retina inputs, is the business of retrieving the orientation map with different intensities but the same object. Figure:32 shows the normalized tuning curves of the network under gratings of different intensity. In a certain range all tuning curves overlap and hence the network is able to retrieve the orientation map similarly for this range. This behaviour is to be expected due to the experimental data of Skottun et. al. [SBS⁺87b].

Another network capability is the ability to retrieve the orientation map when presented gratings with different spatial and temporal wavelength (tab:14). Background for this test is that a biological retina should react to edges of different speed and size and not to a very specific input. And the data suggests that our network is able to operate on a large scale of different combinations of these two, but especially too large wavelengths seem to break the orientation map retrieval. The reason is probably that large wavelengths imply thick and no sharp edges resulting in a weaker translation into thalamic firing rates due to a misfit of Mexican hat filters and then a weaker propagation to the cortex caused by a misfit with the gabor wavelength.

And lastly the network is noise resistant (sec:7.8.6) meaning we may retrieve the orientation map using dashed lines even if we add uniformly distributed noise to the thalamic rates of the same order as the dashed line evoked deviations.

8.3.4 Network statistics

We might utilize the cv to compare our network statistics with experimental data to confirm proximity to a biologically reasonable state. Figure:42 shows the coefficients of variation separated into the six E I populations. The excitatory cv distributions have an arithmetic average of around 0.9 at an average firing rate of around 22 Hz, which is close to a poisson generator which has a cv of 1.0. The simulated cv matches the experimentally measured one analyzed by Softky and Koch [SK93].

8.3.5 Cortical waves

We observe spatial and temporal waves arising in the cortex indifferent of the type of input given into the network (sec:7.8.4). In the random balanced network by Brunel [Bru00] on the other hand they observe temporal waves only when certain parameter combinations of the g factor and the external input are fed into the network. For temporal waves to arise, a g factor of approximately 6 is required in the Brunel network and a high external input for fast waves and a low external input for slow waves. Our waves have frequencies of 14 Hz at the resting state and 20 Hz at the driven state being both even below the slow oscillations in the definition of Brunel. Nevertheless, the Brunel network does not possess a spatial component. Our waves stem most likely from the spatial propagation of activity dominated by strong cortico-cortical connections as described by Muller et. al. [MCRS18]. Meanwhile the waves of the Brunel network originate from a synchronization of all neurons dominated by the input. The temporal oscillations of these two systems are therefore most likely unrelated.

As we can determine the power spectra during the resting state and the grating driven state we may compare our results to the experimental literature. Spyropoulos et. al. [SBF18] measure among many other things the power spectrum of LFP's of macaque V1 during attention on a drifting grating and during no stimulus. Of course the experimental LFP signal is not the same as our spiking signal. The LFP is a combination of nonlinear filtering of the spikes and sub threshold dynamics. Therefore both are related but not quiet the same preventing us from a strict comparison.

In the resting state power spectra of two macaque monkey is measured by Spyropoulos et. al.

[SBF18] where oscillations at various frequencies are observed. Comparing this result to the simulated power spectrum of the population (fig:36a) reveals peaks at around 13 Hz and 30 Hz. Another experiment performed by Spyropoulos et. al. [SBF18] is concerned about the power spectrum under attention to a drifting grating. They find that the frequency peaks change when the monkey focuses on the drifting grating, which is also observable in the driven power spectrum of the simulation in Figure:37. As LFP and spiking signal show waves in the time domain it is likely the slow oscillations in our simulation are in principle observable in biology.

The presented network expresses oscillations during the driven and the resting state (fig:34). However, experiments do not find uniquely oscillatory behaviour in the visual cortex but also for example A I states (Brunel [AB97]). Indeed, looking at the noisy dashed line driven network (fig:35) we observe a transition in the raster plot. After the grating onset the oscillations start to diffuse. Therefore it seems plausible that certain inputs could result in an A I state.

9 Outlook

While the simulated network of L4 of macaque V1 is able to reproduce many features such as orientation tuning, contrast in variance and noise resistance under somewhat realistic conditions, it also leaves an abundance of questions open. These shortcomings could be overcome by integrating more advanced experimental data, which is done for example in the continuously developed Blue brain model [Mar06]. Furthermore simulations on a larger scale could provide for crucial insights. However, also experiments based on this thesis specifically looking for some of the assumed features could either confirm or deny some of the findings.

9.1 Neuron model

Neuronal simulations have the problem that they either can build small models with exact morphology or large models with very simplified neurons, where this thesis falls into the latter. Among the many types of neurons we only modeled one kind of excitatory and two types of inhibitory neurons, whereas even that is an over exaggeration since the inhibitory neurons differ only slightly in their projection and do not necessarily correspond to actual neuron types. A more realistic simulation should account for various types of neurons and their pairwise interactions. However, neither the experimental data nor the computational power yet exist to realize such a network. Furthermore we neglected dendrites in our point neuron model. However, dendrites may be computationally relevant as argued by London et. al. [LH05].

9.2 Connectivity, weight and plasticity

One major problem of experimental connection determination is the enormous amount of connections in the brain, for example patch clamping allows to record only from a few neurons in total as seen in Peng et. al. ([PBTK⁺17]), where eight neurons at once were measured. The number of possible motifs is extremely large, if one notices that each neuron receives somewhat 2000 inputs (Vanni et. al. [VHWA20]). Also different approaches deliver different results and it takes a huge effort such as in Potjans and Diesmann [PD12] to bring for example connectivity maps measured by patch clamping and dye injection together. Due to the few measured data only large scale structures as for example the patchy connectivity can be reliably measured, but all potential fine structure is non reproducible.

Another issue of modeling is the determination of weights, because the post synaptic potential depends on the current membrane potential of the neuron. This problem gets even worse when working with neuron models, for example how would one adequately translate the experimental weight into current based neuron models? With more computational power and more experimental knowledge, future studies could implement neurons with biologically plausible parameters mimicking real neurons way better.

Even though its a key feature of neural networks, we completely ignored plasticity in this thesis. However, the NEST simulator is able to simulate different plasticity models and even with our network size this would be still feasible. Future studies could implement plasticity and analyse

the network under different plasticity parameter choices. For example one could use this studies network and test whether the network is stable under the activation of plasticity, if it is, we could conclude that the configuration is a local minimum and strengthen the validity of connectivity choices.

9.3 Expanding the model

This thesis covers 25 mm^2 of L4 while a macaque monkey possesses around 1200 mm^2 (Vanni et. al. [VHW20]). Reason for this is the increased expenses of larger models requiring more computational power. Nevertheless, the model then also would need to cover the nonlinear part of retinotropic mapping. Furthermore one could include the other layers of V1 again as originally done by Kurth and Albers.

References

- [AB97] D J Amit and N Brunel. Model of global spontaneous activity and local structured activity during delay periods in the cerebral cortex. *Cerebral Cortex*, 7(3):237–252, 04 1997.
- [ACR⁺18] Ján Antolík, Rémy Cagnol, Tibor Rózsa, Cyril Monier, Yves Frégnac, and Andrew P Davison. A comprehensive data-driven model of cat primary visual cortex. *BioRxiv*, page 416156, 2018.
- [ALW⁺02] Alessandra Angelucci, Jonathan B. Levitt, Emma J. S. Walton, Jean-Michel Hupé, Jean Bullier, and Jennifer S. Lund. Circuits for local and global signal integration in primary visual cortex. *Journal of Neuroscience*, 22(19):8633–8646, 2002.
- [BCG⁺20] Yazan N Billeh, Binghuang Cai, Sergey L Gratiy, Kael Dai, Ramakrishnan Iyer, Nathan W Gouwens, Reza Abbasi-Asl, Xiaoxuan Jia, Joshua H Siegle, Shawn R Olsen, et al. Systematic integration of structural and functional data into multi-scale models of mouse primary visual cortex. *Neuron*, 106(3):388–403, 2020.
- [BDM04] Tom Binzegger, Rodney J Douglas, and Kevan AC Martin. A quantitative map of the circuit of cat primary visual cortex. *Journal of Neuroscience*, 24(39):8441–8453, 2004.
- [BDMK91] O Bernander, R J Douglas, K A Martin, and C Koch. Synaptic background activity influences spatiotemporal integration in single pyramidal cells. *Proceedings of the National Academy of Sciences*, 88(24):11569–11573, 1991.
- [BG93] T Bonhoeffer and A Grinvald. The layout of iso-orientation domains in area 18 of cat visual cortex: optical imaging reveals a pinwheel-like organization. *Journal of Neuroscience*, 13(10):4157–4180, 1993.
- [BKS⁺92] C. Beaulieu, Z. Kisvarday, P. Somogyi, M. Cynader, and A. Cowey. Quantitative Distribution of GABA-immunopositive and-immunonegative Neurons and Synapses in the Monkey Striate Cortex (Area 17). *Cerebral Cortex*, 2(4):295–309, 07 1992.
- [BP98] Guo-qiang Bi and Mu-ming Poo. Synaptic modifications in cultured hippocampal neurons: dependence on spike timing, synaptic strength, and postsynaptic cell type. *Journal of neuroscience*, 18(24):10464–10472, 1998.
- [Bro09] Korbinian Brodmann. *Vergleichende Lokalisationslehre der Grosshirnrinde in ihren Prinzipien dargestellt auf Grund des Zellenbaues*. Barth, 1909.
- [Bru00] Nicolas Brunel. Dynamics of Sparsely Connected Networks of Excitatory and Inhibitory Spiking Neurons. *Journal of Computational Neuroscience*, 8(3):183–208, 2000.
- [BZSF97] William H. Bosking, Ying Zhang, Brett Schofield, and David Fitzpatrick. Orientation selectivity and the arrangement of horizontal connections in tree shrew striate cortex. *Journal of Neuroscience*, 17(6):2112–2127, 1997.
- [DA01] Peter Dyan and L.F. Abbott. *Theoretical Neuroscience. Computational and Mathematical Modeling of Systems*. The MIT Press, 55 Hayward Street, Cambridge, MA 02142, 2001.
- [DK23] Michael Denker and Moritz Kern. Elephant 1.0.0, nov 2023.
- [DW61] PM Daniel and D Whitteridge. The representation of the visual field on the cerebral cortex in monkeys. *The Journal of physiology*, 159(2):203, 1961.
- [FGNP85] K H Foster, J P Gaska, M Nagler, and D A Paffen. Spatial and temporal frequency selectivity of neurones in visual cortical areas v1 and v2 of the macaque monkey. *The Journal of Physiology*, 365(1):331–363, 1985.

- [FLB85] D Fitzpatrick, JS Lund, and GG Blasdel. Intrinsic connections of macaque striate cortex: afferent and efferent connections of lamina 4c. *Journal of Neuroscience*, 5(12):3329–3349, 1985.
- [GD07] Marc-Oliver Gewaltig and Markus Diesmann. Nest (neural simulation tool). *Scholarpedia*, 2(4):1430, 2007.
- [GR12] Eustathia Lela Giannaris and Douglas L. Rosene. A stereological study of the numbers of neurons and glia in the primary visual cortex across the lifespan of male and female rhesus monkeys. *Journal of Comparative Neurology*, 520(15):3492–3508, 2012.
- [HA78] P. Heggelund and K. Albus. Orientation selectivity of single cells in striate cortex of cat: The shape of orientation tuning curves. *Vision Research*, 18(8):1067–1071, 1978.
- [Heb49] Donald O Hebb. Organization of behavior. new york: Wiley. *J. Clin. Psychol*, 6(3):335–307, 1949.
- [HSJY87] SH Hendry, HD Schwark, EG Jones, and J Yan. Numbers and proportions of gaba-immunoreactive neurons in different areas of monkey cerebral cortex. *Journal of Neuroscience*, 7(5):1503–1519, 1987.
- [HW59] DH Hubel and TN Wiesel. Receptive fields of single neurones in the cat’s striate cortex. *The Journal of physiology*, 148(3), 1959.
- [JP87] Judson P Jones and Larry A Palmer. An evaluation of the two-dimensional gabor filter model of simple receptive fields in cat striate cortex. *Journal of neurophysiology*, 58(6):1233–1258, 1987.
- [KAR04] Alexandre Kuhn, Ad Aertsen, and Stefan Rotter. Neuronal integration of synaptic input in the fluctuation-driven regime. *Journal of Neuroscience*, 24(10):2345–2356, 2004.
- [KCS92] MF Kritzer, A Cowey, and P Somogyi. Patterns of inter-and intralaminar gabaergic connections distinguish striate (v1) and extrastriate (v2, v4) visual cortices and their functionally specialized subdivisions in the rhesus monkey. *Journal of Neuroscience*, 12(11):4545–4564, 1992.
- [KSL⁺10] Matthias Kaschube, Michael Schnabel, Siegrid Löwel, David M Coppola, Leonard E White, and Fred Wolf. Universality in the evolution of orientation columns in the visual cortex. *science*, 330(6007):1113–1116, 2010.
- [LH81] I.A. Langmoen and J.J. Hablitz. Reversal potential for glutamate responses in hippocampal pyramidal cells. *Neuroscience Letters*, 23(1):61–65, 1981.
- [LH05] Michael London and Michael Häusser. Dendritic computation. *Annu. Rev. Neurosci.*, 28:503–532, 2005.
- [Li00] Zhaoping Li. Pre-attentive segmentation in the primary visual cortex. *Spatial Vision*, 13(1):25 – 50, 2000.
- [Li14] Zhaoping Li. *Understanding Vision theory, models, and data*. Oxford university press, Great Clarendon Street, Oxford, OX2 6DP, United Kingdom, 2014.
- [Mar06] Henry Markram. The blue brain project. *Nature Reviews Neuroscience*, 7(2):153–160, 2006.
- [MCRS18] Lyle Muller, Frédéric Chavane, John Reynolds, and Terrence J Sejnowski. Cortical travelling waves: mechanisms and computational principles. *Nature Reviews Neuroscience*, 19(5):255–268, 2018.
- [Mil10] Kenneth D. Miller. pi = visual cortex. *Science*, 330(6007):1059–1060, 2010.

- [MMF⁺10] N. T. Markov, P. Misery, A. Falchier, C. Lamy, J. Vezoli, R. Quilodran, M. A. Gariel, P. Giroud, M. Ercsey-Ravasz, L. J. Pilaz, C. Huissoud, P. Barone, C. Dehay, Z. Toroczkai, D. C. Van Essen, H. Kennedy, and K. Knoblauch. Weight Consistency Specifies Regularities of Macaque Cortical Networks. *Cerebral Cortex*, 21(6):1254–1272, 11 2010.
- [NGP09] Eilen Nordlie, Marc-Oliver Gewaltig, and Hans Ekkehard Plesser. Towards reproducible descriptions of neuronal network models. *PLOS Computational Biology*, 5(8):1–18, 08 2009.
- [OC82] John O’Kusky and Marc Colonnier. A laminar analysis of the number of neurons, glia, and synapses in the visual cortex (area 17) of adult macaque monkeys. *Journal of Comparative Neurology*, 210(3):278–290, 1982.
- [PBTK⁺17] Yangfan Peng, Federico J. Barreda TomÁjs, Constantin Klisch, Imre Vida, and Joerg R.P. Geiger. Layer-Specific Organization of Local Excitatory and Inhibitory Synaptic Connectivity in the Rat Presubiculum. *Cerebral Cortex*, 27(4):2435–2452, 02 2017.
- [PD12] Tobias C. Potjans and Markus Diesmann. The Cell-Type Specific Cortical Microcircuit: Relating Structure and Activity in a Full-Scale Spiking Network Model. *Cerebral Cortex*, 24(3):785–806, 12 2012.
- [PTP⁺21] Yangfan Peng, Federico J. Barreda Tomas, Paul Pfeiffer, Moritz Drangmeister, Susanne Schreiber, Imre Vida, and Joerg R.P. Geiger. Spatially structured inhibition defined by polarized parvalbumin interneuron axons promotes head direction tuning. *Science Advances*, 7(25):eabg4693, 2021.
- [PY11] Adam M. Packer and Rafael Yuste. Dense, unspecific connectivity of neocortical parvalbumin-positive interneurons: A canonical microcircuit for inhibition? *Journal of Neuroscience*, 31(37):13260–13271, 2011.
- [RB99] Rajesh P. N. Rao and Dana H. Ballard. Predictive coding in the visual cortex: a functional interpretation of some extra-classical receptive-field effects. *Nature Neuroscience*, 2(1):1546–1726, 1999.
- [SB01] Lawrence C Sincich and Gary G Blasdel. Oriented axon projections in primary visual cortex of the monkey. *Journal of Neuroscience*, 21(12):4416–4426, 2001.
- [SBF18] Georgios Spyropoulos, Conrado Arturo Bosman, and Pascal Fries. A theta rhythm in macaque visual cortex and its attentional modulation. *Proceedings of the National Academy of Sciences*, 115(24):E5614–E5623, 2018.
- [SBH⁺18] Maximilian Schmidt, Rembrandt Bakker, Claus C Hilgetag, Markus Diesmann, and Sacha J van Albada. Multi-scale account of the network structure of macaque visual cortex. *Brain Structure and Function*, 223(3):1409–1435, 2018.
- [SBS⁺87a] B. C. Skottun, A. Bradley, G. Sclar, I. Ohzawa, and R. D. Freeman. The effects of contrast on visual orientation and spatial frequency discrimination: a comparison of single cells and behavior. *Journal of Neurophysiology*, 57(3):773–786, 1987. PMID: 3559701.
- [SBS⁺87b] Bernt C Skottun, Arthur Bradley, Gary Sclar, Izumi Ohzawa, and Ralph D Freeman. The effects of contrast on visual orientation and spatial frequency discrimination: a comparison of single cells and behavior. *Journal of neurophysiology*, 57(3):773–786, 1987.
- [SBS⁺18] Maximilian Schmidt, Rembrandt Bakker, Kelly Shen, Gleb Bezgin, Markus Diesmann, and Sacha Jennifer van Albada. A multi-scale layer-resolved spiking network model of resting-state dynamics in macaque visual cortical areas. *PLOS Computational Biology*, 14(10):e1006359, 2018.

- [SDBG02] Dan D Stettler, Aniruddha Das, Jean Bennett, and Charles D Gilbert. Lateral connectivity and contextual interactions in macaque primary visual cortex. *Neuron*, 36(4):739–750, 2002.
- [SF82] Gary Sclar and RD Freeman. Orientation selectivity in the cat’s striate cortex is invariant with stimulus contrast. *Experimental brain research*, 46(3):457–461, 1982.
- [SHvAD18] Johanna Senk, Espen Hagen, Sacha J. van Albada, and Markus Diesmann. Reconciliation of weak pairwise spike-train correlations and highly coherent local field potentials across space. *bio arXiv*, 23, 05 2018.
- [SK93] William R Softky and Christof Koch. The highly irregular firing of cortical cells is inconsistent with temporal integration of random epsps. *Journal of neuroscience*, 13(1):334–350, 1993.
- [SKD⁺22] Johanna Senk, Birgit Kriener, Mikael Djurfeldt, Nicole Voges, Han-Jia Jiang, Lisa Schüttler, Gabriele Gramelsberger, Markus Diesmann, Hans E Plessner, and Sacha J van Albada. Connectivity concepts in neuronal network modeling. *PLoS Computational Biology*, 18(9):e1010086, 2022.
- [SR14] Sadra Sadeh and Stefan Rotter. Statistics and geometry of orientation selectivity in primary visual cortex. *Biological cybernetics*, 108:631–653, 2014.
- [Tau07] Jeffrey S. Taube. The head direction signal: Origins and sensory-motor integration. *Annual Review of Neuroscience*, 30(1):181–207, 2007. PMID: 17341158.
- [TKPM98] Todd W. Troyer, Anton E. Krukowski, Nicholas J. Priebe, and Kenneth D. Miller. Contrast-invariant orientation tuning in cat visual cortex: Thalamocortical input tuning and correlation-based intracortical connectivity. *Journal of Neuroscience*, 18(15):5908–5927, 1998.
- [VHWA20] Simo Vanni, Henri Hokkanen, Francesca Werner, and Alessandra Angelucci. Anatomy and physiology of macaque visual cortical areas v1, v2, and v5/mt: Bases for biologically realistic models. *Cerebral Cortex*, 30(6):3483–3517, 2020.
- [ZKM⁺24] Petr Znamenskiy, Mean-Hwan Kim, Dylan R. Muir, M. Florencia Iacaruso, Sonja B. Hofer, and Thomas D. Mrsic-Flogel. Functional specificity of recurrent inhibition in visual cortex. *Neuron*, 2024.